Metrology of Single Quantum Emitters in Hexagonal Boron Nitride

By

Matthew Feldman

Dissertation

Submitted to the Faculty of the

Graduate School of Vanderbilt University

in partial fulfillment of the requirements

for the degree of

DOCTOR OF PHILOSOPHY

in

Physics and Astronomy

August 31, 2021

Nashville, Tennessee

Approved:

Richard F. Haglund, Ph.D.

Joshua D. Caldwell, Ph.D.

Phil G. Evans, Ph.D.

William R. Holmes, Ph.D.

Norman H. Tolk, Ph.D.

Dedication

I dedicate this thesis to

my wife Dr. Olivia Prosper

and

and our two sons Elijah and Logan Feldman.

Acknowledgment

First, I would like to thank my advisor, Professor Richard F. Haglund, for his guidance and advice throughout my graduate studies. I was admitted to the physics program in large part because of Richard and his belief in my potential. Over the past six years he has provided me with the opportunity and freedom to explore quantum optics and defect physics. He has always made himself readily available for scientific discussions about my experiments and career advice. He has been a bastion of support in aiding me in acquiring funding for my graduate career. Without his mentorship I would not be where I am today.

Second, I would also like to thank my committee members Professor Joshua Caldwell, Professor William Holmes, Dr. Phil Evans and Professor Norman Tolk. Their advice and points of view were very useful in helping me throughout my graduate studies and in concluding my Ph.D.

Third, I would like to thank Dr. Ben Lawrie for giving me the opportunity to conduct research at Oak Ridge National Lab (ONRL). His mentorship has guided me to understand how to successfully manage a scientific career and the professional landscape at a national laboratory. I am indebted to Ben for the opportunity he and Richard have given me to pursue my graduate research at ORNL. He has been a consistent supporter of my scientific career giving insights into lab work, fellowship applications and scientific writing.

Finally I thank my family. I thank them all for putting up with the relentless work load that comes with a Ph.D. They have been so supportive and encouraging. I am forever thankful for my wife Dr. Olivia Prosper, my mother Gretchen Feldman, my father Henry Feldman, my father-in-law Dr. Harrison Prosper and mother-in-law Dr. Marie-France Prosper. They inspired and encouraged me to pursue science. Their perpetual optimism, belief in me and moral support throughout my graduate studies is ultimately why I am a scientist today and why I have thrived during my graduate studies.

TABLE OF CONTENTS

LIST OF TABLES

LIST OF FIGURES

Chapter 1

Introduction

Quantum-based technologies involving light-matter interactions promise revolutionary improvements in sensing [3], computation[4, 5, 6, 7], and communications [8, 9, 10, 11, 12, 13, 7, 14] over their classical counterparts. The goal is to create technologies that use the properties of quantum mechanics to assemble devices either to perform operations that are infeasible with classical resources or to surpass their classical counterparts. Quantum communications in particular can gain much from quantum memories to realize quantum repeaters [15, 16, 17, 18, 19, 20] and flying qubits [21, 22, 23, 24] needed for memory based quantum communication protocols. Quantized physical systems have two properties that are the key to enabling this advantage. First, single-quantum systems offer the ultimate limit in scaling and sensitivity, able to respond to their local mesoscopic environment [25, 26, 27, 28, 29, 30] at sensitivities approaching the Heisenberg limit [31, 32, 33, 34, 35, 36, 37]. Second, unlike classical systems, a quantized system can comprise quantum-entangled networks of single quanta (quantum bits), thus providing a computational basis that scales exponentially for each quantum bit [38, 39]. To enable this second quantum revolution, single-quantum systems must be composed and controlled. Various single-quantum systems have been explored as fundamental technological units for quantum technologies such as optical photons [40], ions [41, 42], atoms [43, 44], and superconducting circuits [45, 46] with the ultimate goal of assembling a highly connected quantum system that can be controlled coherently. However, these quantum technology platforms either cannot be manufactured in a scalable [47] manner or they have short-lived quantum memories.

Alternatively, single-quantum emitters (SQEs) [48, 49, 50, 51, 52] in wide-bandgap solid-state materials offer a direct pathway to scalable quantum systems because current semiconductor and optical fabrication methods can be employed to construct on-chip quan-

tum sensors and quantum networks [53, 54, 55, 56, 57, 58, 59]. An ideal single-quantum emitter by definition is a single-photon source capable of generating indistinguishable photons [60, 61, 62, 63, 64, 65]. Moreover, SQEs with quantum memories [66, 67, 68, 69, 70] (*e.g.*, long-lived spin states) provide quantum sensors or qubits that can be integrated into quantum networks on-chip. To date, two leading candidates for solid-state SQEs have been studied in detail: semiconductor quantum dots and the nitrogen vacancy (NV) center in diamond. However, quantum dots, while having near ideal photon indistinguishability [71] , have poor quantum memory characteristics [72]. On the other hand, the NV center has the longest-lived quantum memory in the solid-state [5, 73] but has poor entanglement rates [74] and cannot generate reliably indistinguishable photons[63, 64]. Thus, the search for other SQE platforms is warranted; to date candidate SQEs have been found in silicon carbide (SiC) [75, 76, 77, 78, 79, 80, 81], rare earth ions [82, 16, 83], gallium nitride (GaN) [84], transition metal dichalcogenides (WsE_2) [85, 86, 87, 88], Zinc Oxide (ZnO) [89, 90], carbon nanotubes [91], cubic boron nitride [92], hexagonal boron nitride (hBN) [93, 2] and group IV emitters in diamond [94, 95, 96, 97].

In this dissertation, I explore the quantum metrology of SQEs in hBN because they are the brightest visible SQEs on record comparable [98] to the brightest quantum dots, and have recently been found to have an optically accessible spin degree of freedom [99, 100, 101, 102, 103, 104]. Yet to date, despite extensive optical characterization [105, 106, 107, 108] and theoretical studies [109, 110, 111, 112, 113, 114, 115, 116, 117, 118, 119, 120] the electronic structure and corresponding atomic origins of these defects are poorly understood. These SQEs emit sharp zero-phonon lines (ZPL) in the spectral region from 1.4 to 2.6 eV; in some cases, the SQEs exhibit broad emission lines attributed to optical-phonon sidebands 165±2 meV on the red side of their ZPL [2, 108]. The broad distribution of ZPLs is likely due to a combination of bright emitters with different atomic structures as well as strain fields inducing energy shifts in their ZPLs. However there is no scientific consensus about either the energy-level structure [121, 2, 122, 107, 1, 105, 123] or the

extent of electron-phonon [124, 125, 126] coupling in these SQEs.

In my work, I begin by exploring the contributions of electron-phonon coupling to the microphotoluminescence spectrum of a hBN SQE using a phenomenological model based on Fermi's golden rule. I then conclusively confirm that the broad emission at 165 and 326 meV are optical one- and two-phonon sidebands by applying two-color Hanbury Brown-Twiss (HBT) interferometry to phonon modes to attain their antibunched auto- and cross-correlations [108]. Furthermore, I substantiate that two-color HBT interferometry in conjunction with photoluminescence can be used to identify additional defects in defect spectra. Given this knowledge, I investigate the excited state energy structure of hBN defects. Here, I provide evidence of photochromism in hBN SQEs with a combination of irradiation-time dependent measures of intensity, microphotoluminescence spectroscopy, and two-color Hanbury Brown-Twiss interferometry. The results reported provide evidence that this hBN SQE exhibits two bright excited-state transitions, suggesting a fundamentally new understanding of hBN-SQE energetics. I was the first to explore cross-correlations in the hBN defect community which has led to the deepening in the understanding of the electron-phonon coupling and energetics of hBN defects. This body of work sets the stage for larger scale color center studies to conduct cross-correlation measurements concurrent with other microscopies to identify the energy structure of hBN defects.

These investigations collectively demonstrate the importance of fundamental investigations with the focused aim of discovering the ideal SQE for applications in quantum sensing and quantum computation. The quantum metrology techniques employed show their versatility in characterizing an SQE optical properties. It is clear that the work in this thesis is but a small piece of the puzzle which numerous researchers are rigorously pushing towards solving: an ideal SQE for quantum information science applications. It is my sincere aspiration that this thesis provides a pedagogical resource and a launching pad for the next generation of the SQE community to push further toward reaching that goal.

I begin with an introduction to the fundamentals of single-quantum emitters, and the

state of the art in hBN in Chapter 2 and 3, respectively. I then discuss electron-phonon coupling in hBN defects (Chapter 4), and the excited state structure of hBN defects (Chapter 5), I conclude with my thoughts on future work in search of the ideal SQE in hBN.

Chapter 2

Theoretical Background in SQEs

2.1 Color Centers

A crystal ideally has no energy levels within its bandgap. Yet the material properties of any crystal can be locally altered by point defects (also referred to as color centers). There are three primary defect types; a vacancy - an atom intrinsic to the crystal missing from its lattice, a substitutional defect - a foreign atom occupying an atomic site of the crystal, and an interstitial defect - a foreign atom that is not located at an atomic site. While point defects in crystals can be exploited as single-quantum emitters their coupling to the lattice phonons and local charge environments degrade their optical properties and these couplings will be briefly reviewed in this section.

Point defects alter the energy level structure of the crystal forming narrow levels inside the crystal bandgap [127, 51]. These narrow levels are positioned deep within the crystal bandgap and electrons in these levels cannot be excited into the conduction band when the point defect is photostable - the defect emits photons at a stable emission rate without its quantum efficiency permanently or partially quenching. There is a non-zero overlap between the color center orbital wave function and the wave function of the lattice and thus momentum from the lattice can be exchanged with the defect in the form of lattice phonons to perturb a point defects energy structure [127]. This is known as electron-phonon coupling and the degree of coupling determines the probability that light will be absorbed or emitted by the defect electron orbital without the emission or absorption of a phonon (zero-phonon line) or the corresponding hybridized electron-phonon transitions with phonon emission or absorption (phonon sidebands).

The local charge environment of a defect also affects SQE optical properties, which introduces several challenges in creating effective SQEs. Color centers with an electric dipole moment, such as substitutional defects like the nitrogen vacancy (NV) center in diamond,

are susceptible to fluctuations in their dipole orientation when coupling to a local charge in the lattice. The repeated interaction of the defect electronic dipole with local charge(s) induces fast time-dependent fluctuations in the defect optical frequency, the time average of which leads to inhomogeneous broadening of the zero-phonon line; this phenomenon is referred to as spectral diffusion. Additionally, the related phenomena of intermittent emission, also referred to as blinking, causes random switching between bright and dark states while under continuous-wave (CW) or quasi-CW excitation due to competing radiative and nonradiative relaxation pathways [128]. In the next section, we will cover the basic photophysical properties for a single-quantum emitter and the corresponding physical properties needed in color centers to overcome these challenges.

2.2 Single-Quantum Emitters

A solid-state single-quantum emitter (SQE) must emit precisely one photon at a time into a single spatial-temporal mode such that all photons emitted are indistinguishable. An SQE must have the following specifications for it to be useful as a quantum technology for quantum information science (QIS) applications[51, 52].

(i) Photostable emission, (*e.g.* no blinking or bleaching).

(ii) High count rate in the zero-phonon line (ZPL)

  (i) Short excited-state lifetimes.

  (ii) High quantum efficiency.

  (iii) High Debye-Waller Factor, (*i.e.* a Debye-Waller Factor near unity).

(iii) High single-photon purity

(iv) Optical lifetime-limited, indistinguishable photons.

(v) Resources required to operate an SQE.

(vi) Spatially addressable fabrication of SQEs.

(vii) Integration of SQEs into nanophotonics devices (*e.g.* dielectric resonators).

As this thesis is focused on the fundamental characterization of SQEs' intrinsic properties we will limit further discussion to properties (i)-(iv). However, we refer the interested reader to the following literature covering extrinsic properties of SQEs [52, 57, 53]. In the remainder of this section, we will define and discuss the relevant theory behind the intrinsic photo-physical properties of SQEs.

2.2.1 Photostability

Photostability and, correspondingly, spectral stability of an SQE zero-phonon line (ZPL) can be improved by passivating [129, 130, 131, 132] the local charge traps surrounding the SQE or electrically and dynamically tuning an SQE ZPL by the Stark effect [133, 134]. However, to date blinking and spectral diffusion caused by charge-SQE interactions can be mitigated best by selecting a SQE that has no electric dipole moment such as the inversion symmetric group IV emitters in diamond [135].

2.2.2 Count Rate

The brightness of an SQE is the maximum count rate that single photons can be emitted and is a determining factor in the entanglement rates of two-qubit gates. Brightness in SQEs depends on three photo-physical properties of the SQE: its excited state lifetime, quantum efficiency and Debye-Waller factor. The excited state lifetime, τ, is defined as the meantime it takes for an electron to radiatively relax from the SQE excited states to its ground state, releasing a single photon in the process, after an excitation pulse. The quantum efficiency is simply the probability that an electron will relax from a SQE excited state to its ground state via a radiative pathway. The quantum efficiency and the excited state lifetime determine the brightness of the multimode (*i.e.* multicolor) emission into the ZPL and the phonon sideband. However photon-photon entanglement rates between SQEs depend on how indistinguishable each SQE ZPL is from the other SQE ZPL. A

factor is needed to determine the fraction of counts corresponding to ZPL emission. The Debye-Waller (D) factor is the ratio of the intensity of light from the ZPL, I_{ZPL} to the total intensity, I_{TOT} of the SQE, $D = \frac{I_{ZPL}}{I_{TOT}}$ [93].

2.2.3 Second-Order Coherence

The signature for single-photon emission of an SQE is its single-photon purity $1 - g^{(2)}(0)$, or the probability of single-photon emission. The single-photon purity is evaluated by the second-order coherence function also referred to as the second-order correlation function, $g^{(2)}(\tau)$ of emitted coincident photons [136]. The coherence function in this context quantifies the degree of correlations between light fields. The second-order coherence function, $g^{(2)}(\tau)$ is the normalized coincident photon counts and is proportional to the transition rate of coincident absorption of photons (intensities) by two single-photon detectors at two points in space-time (t_1, r_1) and (t_2, r_2). Counter to the classical theory in which $g^{(2)}(\tau)$ has a lower bound of unity, the second-order coherence for a single-quantum emitter has zero as its minimum value. Given that $g^{(2)}(\tau)$ is central in characterizing SQEs, a thorough theoretical description is presented for the classical and quantum theories of second-order coherence. In this section, we will also review the standard method of measuring $g^{(2)}(\tau)$ using a Hanbury Brown-Twiss (HBT) interferometer. This technique will be used extensively in the following chapters.

2.2.3.1 Classical Theory

The classical theory of optical coherence deals with large photon numbers and Poissonian statistics. In the classical theory of coherence the second-order coherence is defined as [136]

$$g^{(2)}(\tau) = \frac{\left\langle \bar{I}(t)\bar{I}(t+\tau) \right\rangle}{\left\langle \bar{I}(t) \right\rangle^2}, \tag{2.1}$$

$$= \frac{\langle E^*(t)E^*(t+\tau)E(t+\tau)E(t) \rangle}{\langle E^*(t)E^*(t) \rangle^2}, \tag{2.2}$$

where $\bar{I}$ is the long time average intensity in which $\bar{I}$ is assumed to have ergodic and stationary statistical properties, $E(t)$ and $E^*(t)$ are the electric field amplitude and its complex conjugate at time t, where the total electric field is expanded to $E_{tot}(t) = E(t) + E^*(t)$ for generalization to quantum mechanics. By the even symmetry of this definition it can be shown that [136]

$$g^{(2)}(\tau) = g^{(2)}(-\tau). \tag{2.3}$$

To determine the allowable range of values of $g^{(2)}(\tau)$ we may apply the Cauchy-Schwarz inequality, which any pair of real numbers are subject to, such as intensities. Any two measurements of $\bar{I}$ at times t_1 and t_2 must obey the following inequality [136]

$$2\bar{I}(t_1)\bar{I}(t_2) \leq \bar{I}(t_1)^2 + \bar{I}(t_2)^2. \tag{2.4}$$

For M intensity measurements further application of the above inequality to the cross-terms yields

$$\left[\frac{\bar{I}(t_1) + \bar{I}(t_2) + ... + \bar{I}(t_M)}{M}\right]^2 \leq \frac{\bar{I}(t_1)^2 + \bar{I}(t_2)^2 + ... + \bar{I}(t_M)^2}{M}. \tag{2.5}$$

In the limit of a large number of measurements M the terms on both sides become the statistical means

$$\left\langle \bar{I}(t) \right\rangle^2 \leq \left\langle \bar{I}(t)^2 \right\rangle, \tag{2.6}$$

where we have invoked the stationary assumption. By this inequality and the definition the second-order coherence, at zero time delay $\tau = 0$ the latter must obey

$$1 \leq g^{(2)}(0). \tag{2.7}$$

For classical systems there is no known upper bound, therefore, the range of allowable values for $g^{(2)}(0)$ is [136]

$$1 \leq g^{(2)}(0) < \infty. \tag{2.8}$$

Hence the second-order correlation function at zero delay for classical systems is lower bounded by unity and has no upper bound. This argument above is not extendable to time delay values $\tau \neq 0$ and the only restriction on $g^{(2)}(\tau)$ is that intensities are non-negative real numbers yielding [136]

$$0 \leq g^{(2)}(\tau) < \infty. \tag{2.9}$$

However, the Cauchy-Schwarz inequality may again be applied to determine an inequality between $g^{(2)}(0)$ and $g^{(2)}(\tau)$

$$\{\Sigma_{i=1}^{M} \bar{I}(t_i)\bar{I}(t_i+\tau)\}^2 \leq \Sigma_{i=1}^{M} \bar{I}(t_i)^2 \Sigma_{i=1}^{M} \bar{I}(t_i+\tau)^2. \tag{2.10}$$

The two summations on the right are equivalent for long measurement times again assuming stationary intensities, which yields the conclusion

$$\frac{\left\langle \bar{I}(t)\bar{I}(t+\tau) \right\rangle}{\left\langle \bar{I}(t) \right\rangle^2} \leq 1, \tag{2.11}$$

and thus $g^{(2)}(\tau) \leq g^{(2)}(0)$. Hence for the classical systems the second-order correlation at time τ may never be greater than the second-order correlation at zero delay, according to the preceding inequality.

2.2.3.2 Quantum Theory

The theory of quantum optical coherence requires the quantization of the electromagnetic field. It can be shown that the quantized time dependent operator for the electric field is proportional to the creation and the annihilation operators $\hat{a}^\dagger$ and $\hat{a}$, respectively, of a quantum-harmonic oscillator

$$\hat{E}(t) = \hat{E}^+(t) + \hat{E}^-(t), \tag{2.12}$$

$$= i\frac{\hbar}{\sqrt{2\epsilon_0 V}}(\hat{a}e^{-i\omega t} + \hat{a}^\dagger e^{i\omega t}), \tag{2.13}$$

with positive $\hat{E}^+(t)$ and negative $\hat{E}^-(t)$ electric field operators, where $\hbar$ is Planck's reduced constant, ω is the angular frequency of the electric field, ϵ_0 is the electric permittivity of the material the field passes through, and V is the spatial volume of the electric field within an arbitrary cavity [136]. As we will see in later arguments, the intensity operator $I(\hat{t})$ is the natural operator for the second-order coherence so we will first determine its relation to the electric field operators $\hat{E}^+(t)$ and $\hat{E}^-(t)$.

According to the semiclassical theory of the photoelectric effect, the photoionization rate of a detector is proportional to the intensity of detected light and is a direct measure of the rate of atomic transitions of the detector [136]. Let us presume the detector is initially in a state $|i\rangle$ prior to the absorption of n identical photons. The relevant matrix element of the electric-dipole interaction for the atomic Hamiltonian under second quantization is [136]

$$\langle f|\hat{H}_{ED}|i\rangle = e\langle q|\hat{D}|1\rangle\langle n-1|\hat{E}^+(t)|n\rangle, \tag{2.14}$$

where $\hat{H}_{ED}$ is the electric-dipole interaction Hamiltonian, $|i\rangle$ and $|f\rangle$ are the initial and final states of the dipole transition, e is the electric charge of an electron, q is the wavevector of the electron excited from the ionized atom and $\hat{D}$ is the electric-dipole moment operator. The first and second portions of this expectation value are factorized and for the current discussion only the second component of this expectation values is relevant. Using this and

Fermi's golden rule we can calculate the photoelectric transition rate as [136]

$$\frac{2\pi}{\hbar}\left|\langle n-1|\,E^{+}(t)\,|n\rangle\right|^{2} = \frac{2\pi}{\hbar}\langle n|\,\hat{E}^{-}(t)\,|n-1\rangle\langle n-1|\,\hat{E}^{+}(t)\,|n\rangle, \tag{2.15}$$

$$= \frac{2\pi}{\hbar}\langle n|\,\hat{E}^{-}(t)\hat{E}^{+}(t)\,|n\rangle, \tag{2.16}$$

$$\propto \frac{2\pi}{\hbar}\langle n|\,|\hat{a}^{\dagger}(t)\hat{a}(t)\,|n\rangle. \tag{2.17}$$

Here the operator $\hat{E}^{-}(t)\hat{E}^{+}(t)$ is defined as the intensity operator $\hat{I}(t)$. We now present the definition of the quantum analogue of the second-order coherence [136]

$$g^{(2)}(\tau) = \frac{\left\langle \hat{E}^{-}(t)\hat{E}^{-}(t+\tau)\hat{E}^{+}(t+\tau)\hat{E}^{+}(t)\right\rangle}{\left\langle \hat{E}^{-}(t)\hat{E}^{+}(t)\hat{E}^{-}(t+\tau)\hat{E}^{+}(t+\tau)\right\rangle}, \tag{2.18}$$

$$= \frac{\left\langle \hat{a}^{\dagger}\hat{a}^{\dagger}\hat{a}\hat{a}\right\rangle}{\left\langle \hat{a}^{\dagger}\hat{a}\right\rangle^{2}}, \tag{2.19}$$

$$= \frac{\left\langle \hat{I}(t)\hat{I}(t+\tau)\right\rangle}{\left\langle \hat{I}(t)\right\rangle^{2}}. \tag{2.20}$$

Here the electric field operators are normally ordered, where all the creation operators are to the left of all annihilation operators. Using the commutation relation $[\hat{a},\hat{a}^{\dagger}] = \hat{a}\hat{a}^{\dagger} - \hat{a}^{\dagger}\hat{a} = 1$ we can rewrite equation 2.20 as

$$g^{(2)}(\tau) = \frac{\left\langle \hat{a}^{\dagger}(\hat{a}\hat{a}^{\dagger}-1)\hat{a}\right\rangle}{\left\langle \hat{a}^{\dagger}\hat{a}\right\rangle^{2}} = \frac{\left\langle (\hat{a}^{\dagger}\hat{a})^{2}\right\rangle - \left\langle \hat{a}^{\dagger}\hat{a}\right\rangle}{\left\langle \hat{a}^{\dagger}\hat{a}\right\rangle^{2}}. \tag{2.21}$$

If we examine equation 2.21 in the Fock (photon number) basis $|n\rangle$ we find that the lower bound for the quantum theory of $g^{(2)}(\tau)$ differs from its classical counterpart

$$g^{(2)}(\tau) = \frac{\langle n|\,(\hat{a}^{\dagger}\hat{a})^{2}\,|n\rangle - \langle n|\,\hat{a}^{\dagger}\hat{a}\,|n\rangle}{\langle n|\,\hat{a}^{\dagger}\hat{a}\,|n\rangle^{2}} = \frac{\left\langle n^{2}\right\rangle - \langle n\rangle}{\langle n\rangle^{2}} = 1 - \frac{1}{\langle n\rangle}, \tag{2.22}$$

and consequently upon substituting $|1\rangle$ for $|n\rangle$ it is readily apparent that the quantum analogue of $g^{(2)}(\tau)$ has a lower bound of 0 as opposed to its classical counterpart.

2.2.3.3 Comparison of Photon Statistics in Classical and Quantum Light Sources

The second-order coherence function is an observable used to characterize the photon statistics of a given physical system. We will now review examples of classical light (coherent states and chaotic light) and quantum light (the two-level and three-level SQE), which represent the possible physical regimes of photons statistics (Poisson, superpoissonian, and subpiossonian) for quantum and classical light sources.

Let $|\alpha\rangle$ be the quantum state that most closely mimicks a classical light field. For a given coherent state $|\alpha\rangle$, the second-order autocorrelation becomes [136]

$$g^{(2)}(\tau) = \frac{\left\langle \alpha|\hat{a}^\dagger \hat{a}^\dagger \hat{a}\hat{a}|\alpha\right\rangle}{\left\langle \alpha|\hat{a}^\dagger \hat{a}|\alpha\right\rangle^2} = 1, \tag{2.23}$$

since $|\alpha\rangle$ are right ($\hat{a}\,|\alpha\rangle = \alpha\,|\alpha\rangle$) and left ($\langle\alpha|\,\hat{a}^\dagger = \langle\alpha|\,\alpha^*$) eigenstates of the photon destruction and creation operators. The probability to find n photons in state $|\alpha\rangle$ is Poisson and so its mean photon count and photon count variance are equal, $\langle n\rangle = (\Delta n)^2 = |\alpha|^2$. Furthermore, upon consideration of the $g^{(2)}(\tau)$ in the Fock state basis it is clear that the $g^{(2)}(\tau) = 1$ is proof that a coherent state photon number distribution is Poisson,

$$\begin{aligned} g^{(2)}(\tau) &= \frac{\langle n(n-1)\rangle}{\langle n\rangle^2} = \frac{\left\langle n^2\right\rangle - \langle n\rangle}{\langle n\rangle^2} = 1 + \frac{(\Delta n)^2 - \langle n\rangle}{\langle n\rangle^2}, \\ &= 1, \end{aligned} \tag{2.24}$$

since $(\Delta n)^2 - \langle n\rangle = 0$ for a Poisson distribution.

Superpoissonian light sources, such as a chaotic light source, exhibit photon bunching due to photon packets piling up within the coherence time τ_c of the ensemble of atoms comprising the source. Here the photons are coherent only within τ_c and decohere exponentially as [136],

$$g^{(2)}(\tau) = 1 + e^{(-2|\tau|/\tau_c)}. \tag{2.25}$$

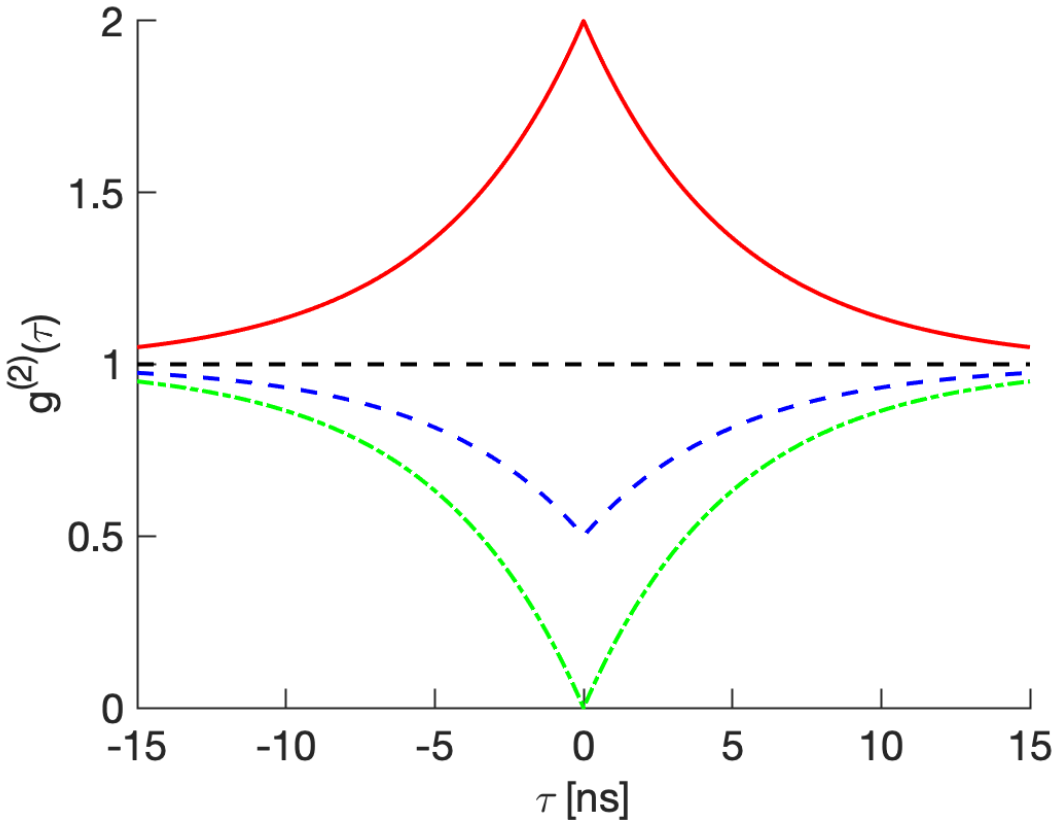

Figure 2.1: Summary of photon statistics for classical and quantum light sources. The black dashed line is the second-order coherence, $g^{(2)}(\tau) = 1$ for a coherent light source with Poisson statistics where $(\Delta n)^2 = \langle n \rangle$; the red solid line is the $g^{(2)}(\tau) = 1 + e^{(-2|\tau|/\tau_c)}$ for a chaotic light source with superpoissonian statistics where $(\Delta n)^2 > \langle n \rangle$; The dashed green curve is the $g^{(2)}(\tau) = 1 - e^{(-|\tau|/\tau_c)}$ for an SQE with subpoissonian statistics where $(\Delta n)^2 < \langle n \rangle$; the blue dashed curve is $g^{(2)}(\tau) = 1 - (1/2)e^{(-|\tau|/\tau_c)}$ and it represents the upper bound of $g^{(2)}(\tau)$ for determining the single photon quality of a two-level SQE degraded by background light.

Similar to the coherent source, it can be shown that a chaotic source, *i.e.* a state of maximum entropy, is superpossionian given that its photon statistics follow a geometric distribution with variance $(\Delta n)^2 = \langle n \rangle^2 + \langle n \rangle$. Equation 2.24 leads to $g^{(2)}(0) = 2$ and hence the variance of a chaotic source must exceed its mean.

For classical light the second-order coherence function satisfies $1 \leq g^{(2)}(\tau) < \infty$, due to the Cauchy-Schwarz inequality. As seen earlier, in contrast to classical sources of light, for quantum light this does not hold. This is exemplified by the second-order correlation

function for a Fock number state as previously shown

$$1 - \frac{1}{\langle n \rangle} < g^{(2)}(\tau) < \infty, \tag{2.26}$$

for mean photon numbers $\langle n \rangle \geq 1$. A quantum photon source exhibits antibunching, which is anticorrelations in the the second-order coherence function where $g^{(2)}(\tau) > g^{(2)}(0)$. A quantum light source may also exhibit subpoissonian statistics where $g^{(2)}(0) < 1$ and while the quantum source does not always have antibunched and have subpoissionian photon statistics this is the case for SQEs [136]. For an SQE, as we will see, we can model the photon statistics according to the optical Bloch equations under resonant excitation or simpler rate equation under off-resonant excitation using a two-level atomic model. For a true single-quantum emitter only one photon, $n = 1$, can be emitted at any given time within the optical lifetime, τ_c of the SQE and correspondingly the single-photon purity is $1 - g^{(2)}(0) = 1$, where $g^{(2)}(\tau) = 1 - e^{-|\tau|/\tau_c}$. However, practically all experiments suffer from background counts due to photoactive impurities on the sample, as well as detector dark counts, *i.e.* counts in the absence of a signal, which diminish the single-photon purity of the SQE. Here the minimum condition for single-photon emission of an SQE is $g^{(2)}(0) < 0.5$, where $g^{(2)}(\tau) = 1 - (1/n)e^{(-|\tau|/\tau_c)}$, n is the number of emitters within the same confocal volume and all emitters are equally coupled to the optical experimental apparatus.

We have reviewed the different regimes of photon statistics for quantum and classical systems, which is determined by $g^{(2)}(\tau)$. These regimes are identified as follows: Poisson light, $g^{(2)}(\tau) = 1$; superpoissonian light which exhibits photon bunching, $g^{(2)}(\tau) > 1$; and subpoissonian and antibunched light, $g^{(2)}(\tau) < 1$. The different regimes are summarized in Figure 2.1.

2.2.3.4 Two-level Model for a Single-Quantum Emitter

For evaluating the photophysics of single-quantum emitters (SQE) we can simplify the SQE energy level structure to either a two or three-level model. While some SQEs require

more levels to explain their photodynamics [121] we will limit our discussion to these two cases. The simplest and most fundamental model of a SQE is a two-level atomic model with excited state ($|2\rangle$) and ground state ($|1\rangle$) as depicted in Figure 2.2a where $|2\rangle$ and $|1\rangle$ are not to be confused with Fock states. First the SQE electron is excited at a pumping rate k_{12} by an external radiating field where photons have energies equal to or greater than the energy difference of the two levels. The electron then experiences a transition from $|1\rangle$ to $|2\rangle$. Upon the electron relaxation to $|1\rangle$ at a spontaneous emission rate k_{21} a single photon is emitted, giving a zero probability of coincident photon emission ($g^{(2)}(0) = 0$). Under resonant excitation the equations of motion can be described using the optical Bloch equations [136, 137],

$$\dot{\rho}_{12}(t) = \frac{i\Omega}{2}(\rho_{21} - \rho_{12}) - 2k_{21}\rho_{22}, \text{ and} \tag{2.27}$$

$$\dot{\rho}_{22}(t) = \frac{i\Omega}{2}(\rho_{11} - \rho_{22}) + i((\omega_o - \omega) - k_{21}^{'})\rho_{12}, \tag{2.28}$$

where $\dot{\rho}_{ij}(t)$ is the time derivative of $\rho_{ij}(t)$, Ω is the Rabi frequency, ρ_{ij} are elements of the density operator, $k_{21}^{\prime} = k_{21} + k_{21}^{''}$ is the effective spontaneous emission rate from $|2\rangle$ to $|1\rangle$, k_{21} is the liftetime-limited emission rate and $k_{21}^{''}$ describe the cumulative electronic decoherence pathways that increase $k_{21}^{'}$. The Rabi frequency is $\Omega = e\mathbf{E}\cdot\mathbf{D}_{12}/\hbar$, where $\mathbf{D_{12}}$ is the SQE transition dipole moment, $\mathbf{E}$ is the field driving the SQE, e is the electric charge of an electron and $\hbar$ is the reduced Planck's constant. The remaining equations of motion can be derived using the following relations for the density matrix elements

$$\rho_{21} = \rho_{12}^{*}, \quad \rho_{11} + \rho_{22} = 1, \tag{2.29}$$

where ρ_{12}^{*} denotes the complex conjugate of ρ_{12}.

The optical Bloch equations can also be restated using the steady-state expectation val-

ues of atomic transition operators in the interaction picture

$$\langle\hat{\pi}(t)\rangle = \hat{\rho}_{21}(t), \tag{2.30}$$

$$\left\langle\hat{\pi}^{\dagger}(t)\right\rangle = \hat{\rho}_{12}(t), \text{ and} \tag{2.31}$$

$$\left\langle\hat{\pi}^{\dagger}(t)\hat{\pi}(t)\right\rangle = \hat{\rho}_{22}(t), \tag{2.32}$$

where $\hat{\pi} = |1\rangle\langle 2|$ and $\hat{\pi}^{\dagger} = |2\rangle\langle 1|$ are the atomic raising and lowering operators and $\hat{\rho}_{ij}$ are the elements of the density matrix. The SQE is initially taken to be in the $|1\rangle$ ground state prior to excitation. Thus all density matrix elements $\hat{\rho}_{ij}$ have a linear dependence on the boundary conditions $\hat{\rho}_{12}(0) = \hat{\rho}_{21}(0) = \hat{\rho}_{22}(0) = 0$. With this in mind we can reformulate $\left\langle\hat{\pi}^{\dagger}(t)\hat{\pi}(t)\right\rangle$ as [137]

$$\left\langle\hat{\pi}^{\dagger}(t)\hat{\pi}(t)\right\rangle = \alpha_1(t) + \alpha_2(t)\langle\hat{\pi}(0)\rangle + \alpha_3(t)\left\langle\hat{\pi}^{\dagger}(0)\right\rangle + \alpha_4(t)\left\langle\hat{\pi}^{\dagger}(0)\hat{\pi}(0)\right\rangle, \tag{2.33}$$

where we find the function $\alpha_j(t)$ by solving the optical Bloch equations. An additional boundary conditions arises in the limit of long integration times. In this case damping mechanisms in the SQE degrades its optical coherence in the steady state and all information about the initial state of the SQE is lost. Here, $\alpha_2(\infty) = \alpha_3(\infty) = \alpha_4(\infty) = 0$ and thus in the steady-state (st)

$$\left\langle\hat{\pi}^{\dagger}(\infty)\hat{\pi}(\infty)\right\rangle_{st} = \alpha_1(\infty). \tag{2.34}$$

To determine the second-order coherence we must first apply the quantum regression theorem, which allows us to restate any two-time expectation value in terms of single-time expectation values [137]. If a first-order expectation value $\left\langle\hat{A}(t+\tau)\right\rangle$ can be written as a linear combination of single-time expectation values

$$\left\langle\hat{A}(t+\tau)\right\rangle = \sum \alpha_i(\tau)\left\langle\hat{A}_i(t)\right\rangle, \tag{2.35}$$

then any expectation value that is second-order in time may be rewritten as

$$\left\langle \hat{B}(t)\hat{A}(t+\tau)\hat{C}(t)\right\rangle = \Sigma\alpha_i(\tau)\left\langle \hat{B}(t)\hat{A}_i(t)\hat{C}(t)\right\rangle. \tag{2.36}$$

We now seek to determine the second-order coherence for the two-level SQE. We may first use the fact that the source-field expression for the positive $E^+(t)$ and negative $E^-(t)$ frequency electric field operators of a two-level atom are proportional to the atomic lowering $\langle\hat{\pi}\rangle$ and raising $\left\langle\hat{\pi}^\dagger\right\rangle$ operators and we can rewrite the second-order coherence as

$$g^{(2)}(\tau) = \frac{\left\langle \hat{E}^-(t)\hat{E}^-(t+\tau)\hat{E}^+(t+\tau)\hat{E}^+(t)\right\rangle}{\left\langle \hat{E}^-(t)\hat{E}^+(t)\hat{E}^-(t+\tau)\hat{E}^+(t+\tau)\right\rangle}, \tag{2.37}$$

$$= \frac{\left\langle \hat{\pi}^\dagger(t)\hat{\pi}^\dagger(t+\tau)\hat{\pi}(t+\tau)\hat{\pi}(t)\right\rangle}{\left\langle \hat{\pi}^\dagger(t)\hat{\pi}(t)\right\rangle^2}. \tag{2.38}$$

From the quantum regression theorem it follows that

$$\left\langle \hat{\pi}^\dagger(t)\hat{\pi}^\dagger(t+\tau)\hat{\pi}(t+\tau)\hat{\pi}(t)\right\rangle = \alpha_1(\tau)\left\langle \hat{\pi}^\dagger(t)\hat{\pi}(t)\right\rangle_{st}. \tag{2.39}$$

In equation 2.39 it follows from the boundary conditions at $t = 0$ (see equations 2.30-2.34) that $\alpha_1(\tau)$ is the population of the excited state $|2\rangle$ at time τ, $\rho_{22}(\tau)$ after the excitation of the SQE with the SQE initially in the ground state $|1\rangle$ and the remaining factor is the steady-state value for the excited state population, $\rho_{22}(\infty)$. We can then express the second-order coherence as

$$g^{(2)}(\tau) = \frac{\alpha_1(\tau)}{\alpha_1(\infty)} = \frac{\rho_{22}(\tau)}{\rho_{22}(\infty)}. \tag{2.40}$$

It is clear that the time dependence of $g^{(2)}(\tau)$ is dictated by the time-dependent population of the excited state, $\rho_{22}(t)$. The excited state population can be derived from the optical

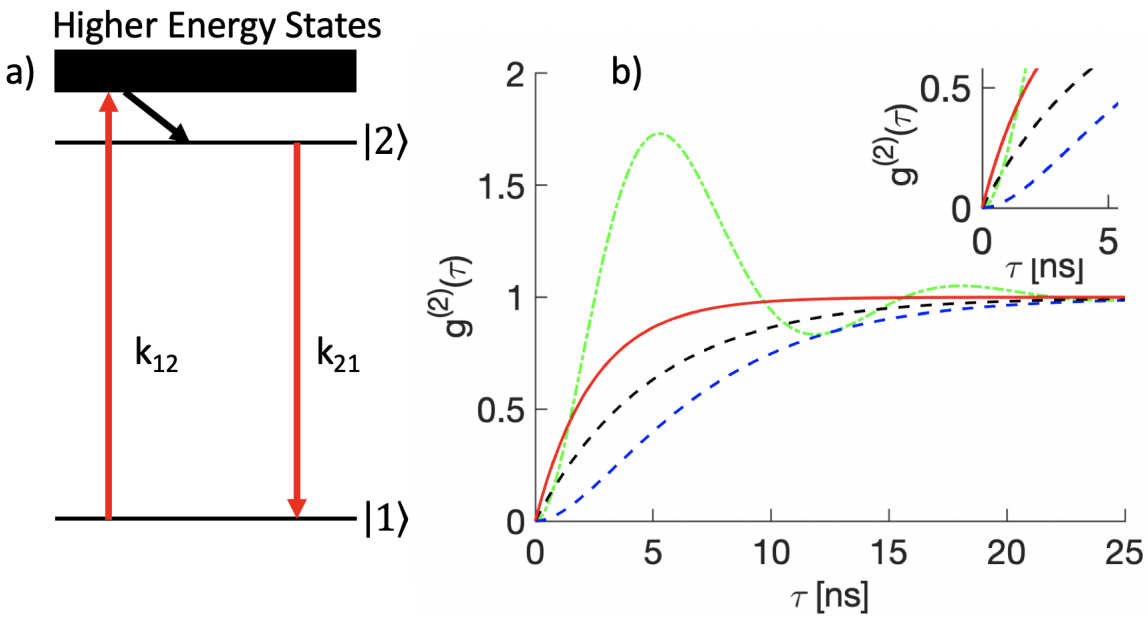

Figure 2.2: Two-level SQE. a) The energy diagram of a two-level system with excitation rate k_{12} and spontaneous emission rate k_{21}. When the SQE experiences additional optical decoherence processes, the k_{21} is replaced by $k_{21}^{'}$ the effective spontaneous emission rate. b) The $g^{(2)}(\tau)$ for an SQE driven coherently (green, red and blue traces) and incoherently (black trace). For a coherently driven SQE there are three cases: i) where the only decoherence process is given by k_{21} (green trace), ii) where there is also zero detuning (blue trace) and iii) there are significant additional decoherence pathways $k_{21}^{'} \gg k_{21}$ (red trace).

Bloch equations and the second-order correlation in this case is [136]

$$g^{(2)}(\tau) = \frac{\rho_{22}(\tau)}{\rho_{22}(\infty)} \tag{2.41}$$

$$\begin{aligned} &= 1 + \frac{(2k_{21} - k_{21}^{'})[(\omega_0 - \omega)^2 + k_{21}^{'2}]/k_{21}^{'}}{(\omega_0 - \omega)^2 + (2k_{21} - k_{21}^{'})^2} e^{-2k_{21}\tau} \\ &- \frac{2k_{21}[(\omega_0 - \omega)^2 + (2k_{21} - k_{21}^{'})^2]cos[(\omega_0 - \omega)\tau]}{k_{21}^{'}[(\omega_0 - \omega)^2 + (2k_{21} - k_{21}^{'})^2]} e^{-k_{21}^{'}\tau} \\ &- \frac{4k_{21}(\omega_0 - \omega)(k_{21}^{'} - k_{21})sin[(\omega_0 - \omega)\tau]}{k_{21}^{'}[(\omega_0 - \omega)^2 + (2k_{21} - k_{21}^{'})^2]} e^{-k_{21}^{'}\tau} \end{aligned} \tag{2.42}$$

where $\rho_{22}(\tau)$ is the population of the excited state $|2\rangle$ at time τ, $\rho_{22}(\infty)$ is the limit of $\rho_{22}(\tau)$ when the population of $|2\rangle$ is saturated; and ω_0 is frequency corresponding to the transition between the two energy levels and ω is the frequency of a monochromatic driving field,

$E = E_0 \cos(kz - \omega\tau)$. Since this is a rather complex result it is best to focus on three limiting cases to determine the essential physics at play. In all cases presented in this thesis weak driving is assumed where $\Omega << k_{21}$; here Ω and k_{21} are the Rabi frequency and the life-time limited spontaneous emission rate. In the first case let us first assume that there are no additional decoherence processes beyond spontaneous emission (rate $k_{21}^{'} = k_{21}$). In this case equation 2.42 reduces to

$$g^{(2)}(\tau) = 1 + e^{-2k_{21}\tau} - 2\cos[(\omega_0 - \omega)\tau]e^{-k_{21}^{'}\tau}, \tag{2.43}$$

leading to coherent Rabi oscillations in $g^{(2)}(\tau)$ for small detuning, $\omega \approx \omega_0$. In the second case, a coherent driving field is present in which there is zero detuning, $\omega = \omega_0$, between the driving field frequency, ω and the resonant frequency of the two-level SQE ω_0, in which case

$$g^{(2)}(\tau) = (1 - e^{-k_{21}\tau})^2. \tag{2.44}$$

In the third case, we presume that the dominant optical decoherence pathways are elastic or inelastic broadening due to nonideal optical relaxation mechanisms (*e.g.* spectral diffusion) leading to $k_{21}^{'} \gg k_{21}$. In this case the second exponential term in equation 2.43 goes to zero for sufficiently large delay times, τ, such that $k_{21}^{'}\tau \gg 1$ and, therefore,

$$g^{(2)}(\tau) = 1 - e^{-2k_{21}\tau}. \tag{2.45}$$

In the case of off-resonantly excited SQE coherence the electronic motion is described completely by the on-diagonal elements of the density matrix. These elements have a time

dependence given by the rate equations of atomic populations [136]

$$\dot{\rho}_{11} = -k_{12}\rho_{11} + k_{21}\rho_{22}, \text{ and} \tag{2.46}$$

$$\dot{\rho}_{22} = k_{12}\rho_{11} - k_{21}\rho_{22}, \tag{2.47}$$

where k_{12} is the excitation rate, k_{21} is the spontaneous emission rate and ρ_{ii} is the diagonal density matrix elements, which is equivalent to the probability of the SQE being in the ith state. Again the populations ρ_{22} and ρ_{11} are the only populations possible and must satisfy $\rho_{22} + \rho_{11} = 1$. The solutions to the rate equations for $\tau \geq 0$ are

$$\rho_{11} = \frac{k_{21}}{k_{12} + k_{21}}(1 + e^{-(k_{12}+k_{21})\tau}), \text{ and} \tag{2.48}$$

$$\rho_{22} = \frac{k_{12}}{k_{12} + k_{21}}(1 - e^{-(k_{12}+k_{21})\tau}). \tag{2.49}$$

By inspection it is clear that $\rho_{22}(\infty) = (k_{12}/(k_{12} + k_{21})$ and from equation 2.40 we have

$$g^{(2)}(\tau) = (1 - e^{-(k_{12}+k_{21})\tau}). \tag{2.50}$$

A summary of the photon statistics for coherent and incoherently driven two-level SQEs is provided in Figure 2.2b.

2.2.3.5 Three-level Model for a Single-Quantum Emitter

While the photophysics of some quantum dots can be explained sufficiently by a two-level atomic model, most SQEs are more complex often requiring additional levels to explain the observed photodynamics, which leads to additional correlations in their second-order coherence. In many cases, such as color centers in diamond and single molecules, we must include a third level, $|3\rangle$ to model the trapping of the electron in a metastable or shelving state, which is unable to emit photons until it relaxes to the ground $|1\rangle$ state leading to bunching in $g^{(2)}(\tau)$ at $\tau > 0$ [138]. As shown in Figure 2.3a, we add a third metastable

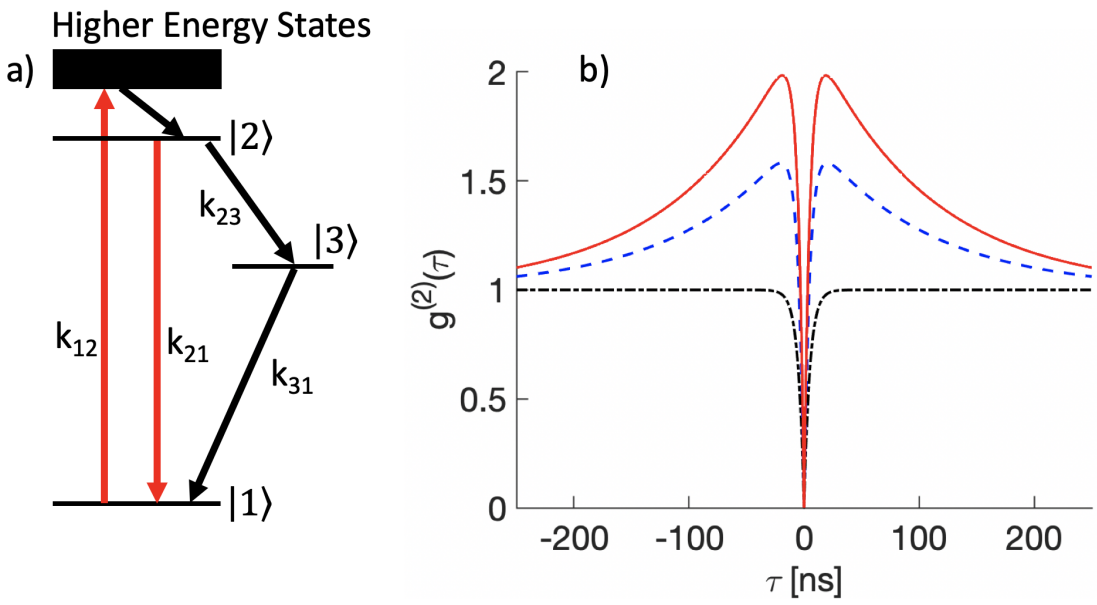

Figure 2.3: Three-level SQE. a) the energy diagram of a three-level system with excitation and spontaneous emission rates k_{12} and k_{21} and shelving rates k_{23} and k_{31} . b) The $g^{(2)}(\tau)$ for a three-level SQE with varying shelving amplitudes (0, 0.75, and 1.25).

state that has transition rates k_{23} and k_{31} to the original two-level model for a total of four transition pathways the SQE can take across the three states. In this model we neglect transition rates k_{32} and k_{13} since during off-resonant excitation absorption is unlikely for transitions from $|3\rangle$ to $|2\rangle$ and from $|1\rangle$ to $|3\rangle$. Since the coherence between levels decays rapidly in SQEs it is sufficient to use rate equations instead of the optical Bloch equations. The equations of motion for the three-level system are [138]

$$\dot{\rho_{11}} = -k_{12}\rho_{11} + k_{21}\rho_{22} + k_{31}\rho_{33}, \tag{2.51}$$

$$\dot{\rho_{22}} = k_{12}\rho_{11} - (k_{21} + k_{23})\rho_{22}, \tag{2.52}$$

$$\dot{\rho_{33}} = k_{23}\rho_{22} - k_{31}\rho_{33}, \text{ and} \tag{2.53}$$

$$1 = \rho_{11} + \rho_{22} + \rho_{33}, \tag{2.54}$$

where ρ_{33} is the population of the third state $|3\rangle$. These equations of motion show that similar to the two-level model, a single electron occupies one of these three states at any given time. It is often the case that the transition rates k_{23}, k_{31} associated with metastable states $|3\rangle$ in SQEs are orders of magnitude slower than that for the excitation (k_{12}) and spontaneous emission (k_{21}) rates between the ground and excited states, as is the case for emitters in diamond and single molecules. Solving equation 2.40, given the above rate equations, yields the second-order correlation function for a three-level SQE with [138]

$$g^{(2)}(\tau) = 1 - (1+a)e^{-\gamma_1|\tau|} + ae^{-\gamma_2|\tau|}, \tag{2.55}$$

where a is the shelving amplitude that determines the amplitude of the photon bunching, while γ_1 and γ_2 are decay rates associated with the excited and metastable state. It can be shown that the decay pathways (γ_1, γ_2) and the shelving parameter a can be written in terms of the three-level SQE transition rates k_{ij} [138]

$$\gamma_1 \approx k_{12} + k_{21}, \tag{2.56}$$

$$\gamma_2 \approx k_{21} + \frac{k_{12}k_{23}}{k_{12}+k_{21}}, \text{ and} \tag{2.57}$$

$$a \approx \frac{k_{12}k_{23}}{k_{31}(k_{12}+k_{21})}. \tag{2.58}$$

Figure 2.3b displays the effects of varying shelving amplitudes and lifetimes on the photodynamics of a three-level system.

2.2.3.6 Background Correction for the Second-order Correlation Function

For any model the effect of background counts on the measurement must be taken into account since common background sources such as room light, scattered laser light, and diffuse photoluminescence from the sample will degrade the measured photon purity of the SQE. All of the aforementioned background sources have Poisson photon statistics and

coupling to these sources while measuring an SQE will cause $g^{(2)}(0) > 0$ [48]. If we assume a steady state singles count rate S and B for the SQE signal counts and the background counts, respectively, then we may define a ratio of signal to total counts as

$$\rho = \frac{S}{S+B}. \tag{2.59}$$

The measured coincidence counts $C_n(\tau)$, is then

$$C_n(\tau) = \langle n \rangle_m^2 g_m^{(2)}(\tau) = \langle n \rangle_m^2 (1 - \rho^2 + \rho^2 g_{ideal}^{(2)}(\tau)), \tag{2.60}$$

where $\langle n \rangle_m$ is the measured singles counts rate and $g_m^{(2)}(\tau)$ and $g_{ideal}^{(2)}(\tau)$ are the measured and ideal second-order coherence functions, respectively, for a given coincidence measurement [48]. It must be noted that this background model does not take into account the effect of the instrument response function of the single photon counter, which may further degrade the measured purity of an SQE. For a three-level system the ideal correlation function is given in equation 2.55, where $\tau_1 = 1/\gamma_1$ and $\tau_2 = 1/\gamma_2$. For a three-level model the measured second-order coherence is

$$g_m^{(2)}(\tau) = 1 - \rho^2[(1+a)e^{-|\tau|/\tau_1} - ae^{-|\tau|/\tau_2}]. \tag{2.61}$$

When no shelving is observed the measured second-order coherence function reduces to that of the two-level model

$$g_m^{(2)}(\tau) = [1 - \rho^2 e^{-|\tau|/\tau_1}]. \tag{2.62}$$

Under the condition of zero shelving the threshold for identifying single photon emission is then $g^{(2)}(0) < 0.5$, however, for a three-level SQE we must factor in the effects of shelving on this threshold as bunching can cause the $g^{(2)}(\tau)$ at $\tau < \tau_2$ to exhibit superpoission statis-

tics. In this case the threshold $g^{(2)}_{limit}$ is half of the bunched amplitude in the limit where τ_1 and τ go to zero for $g^{(2)}_m(\tau)$ [107]

$$g^{(2)}_{limit} = \frac{1}{2}(1+\rho^2 a), \tag{2.63}$$

and thus for a three-level system the minimum specification for single photon emission is $g^{(2)}(0) < \frac{1}{2}(1+\rho^2 a)$ and in the case of zero shelving ($a = 0$) this threshold reduces to that for a two-level model ($g^{(2)}(0) < 0.5$).

2.2.3.7 Hanbury Brown-Twiss Interferometry

The second-order coherence and correspondingly the single-photon purity of an SQE is measured using a Hanbury Brown-Twiss (HBT) interferometer that comprises a 50/50 beamsplitter with light entering port 1 of the beamsplitter and the light at its output ports being collected by two single-photon detectors where the coincident and singles counts are analyzed by a timer tagger as shown in Figure 2.4a [136]. In 1956 the HBT interferometer was used to measure the angular size of the star Sirius [139]. A strongly bunched correlation was observed over a range of meters until it damped over a range of kilometers giving the apparent angular dimension for Sirius. This spurred a flurry of theoretical work to understand the classical and quantum correlations previously discussed [140]. In this subsection, we will first review the relevant classical physics of an ideal beamsplitter and then derive the second-order coherence assuming photons in an arbitrary Fock state are incident at the input to an HBT interferometer.

An ideal beamsplitter is presented in Figure 2.4b with two input and two output ports with four identical light beams at each port. The beamsplitter is assumed to be lossless with no energy dissipation due to reflection off or transmission through the partially silvered beamsplitter [136]. The light field at the output ports is related to the light field at the input

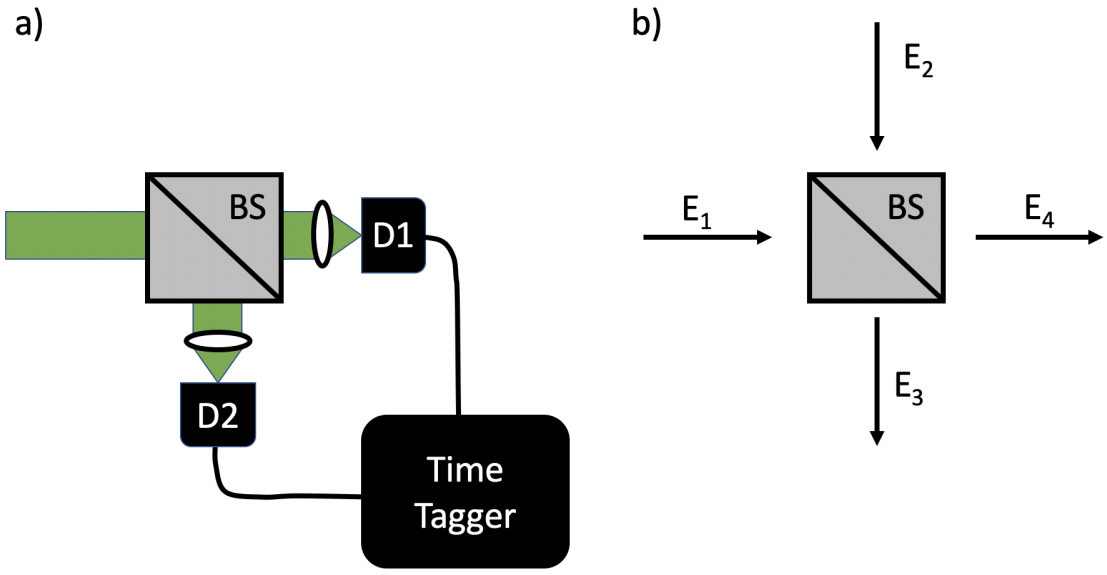

Figure 2.4: Hanbury Brown-Twiss (HBT) Interferometer. a) For the HBT interferometer light enters a half-silvered beamsplitter (BS) and is detected at the outputs of the beamsplitter using detectors D1 and D2; the counts are then timed and recorded using a time tagger. b) An ideal half-silvered beamsplitter with incident light field E_1 and E_2 and identical output light field E_3 and E_4.

ports by the following relations

$$E_3 = R_{31}E_1 + T_{32}E_2, \text{ and} \tag{2.64}$$
$$E_4 = T_{41}E_1 + R_{42}E_2,$$

where R_{ij} and T_{ij} are the directionally-dependent reflection and transmission coefficients of the beamsplitter. These coefficients in the non-ideal case are wavelength dependent with additional losses introduced due to the material properties of the reflector material. By energy conservation the total energy of the light at the input ports must equal the total energy of the light at the output ports

$$|E_1|^2 + |E_2|^2 = |E_3|^2 + |E_4|^2. \tag{2.65}$$

Energy conservation is satisfied for both input light fields (E_1, E_2) when

$$|R_{31}|^2 + |T_{41}|^2 = |R_{42}|^2 + |T_{32}|^2 = 1, \text{ and} \tag{2.66}$$

$$R_{31}T_{32}^* + T_{41}R_{42}^* = 0. \tag{2.67}$$

If we further assume that all reflection ($R_{31} = -R_{42}$) and transmission ($T_{32} = T_{41}$) coefficients are identical, respectively, then equations 2.66 and 2.67 simplify to

$$|R|^2 + |T|^2 = 1, \text{ and} \tag{2.68}$$

$$RT^* + TR^* = 0. \tag{2.69}$$

It can be shown that when the electric field, E_i, is quantized we have the following ladder operators, $\hat{a}_i$, associated with the output of the beamsplitter [136]

$$\hat{a}_3 = R\hat{a}_1 + T\hat{a}_2, \text{ and} \tag{2.70}$$

$$\hat{a}_4 = T\hat{a}_1 + R\hat{a}_2.$$

Here each $\hat{a}_i$ is associated with each E_i as shown in Figure 2.4b. We assume the input light fields are independent, in which case we have the following commutation relations $[\hat{a}_i, \hat{a}_i^\dagger] = 1$ for $i = 1, 2$ and $[\hat{a}_i, \hat{a}_j^\dagger] = 0$ for $i, j = 1, 2$ and $i \neq j$. The commutation relations for the output fields are given by

$$[\hat{a}_3, \hat{a}_3^\dagger] = [R\hat{a}_1 + T\hat{a}_2, R^*\hat{a}_1^\dagger + T^*\hat{a}_2^\dagger] = |R|^2 + |T|^2 = 1, \text{ and} \tag{2.71}$$

$$[\hat{a}_3, \hat{a}_4^\dagger] = [R\hat{a}_1 + T\hat{a}_2, T^*\hat{a}_1^\dagger + R^*\hat{a}_2^\dagger] = RT^* + TR^* = 0, \tag{2.72}$$

which are equivalent to the conditions for energy conservation in the classical derivation [136]. We now define the photon number operator for an ideal beamsplitter at each

arm as $\hat{n}_i = \hat{a}_i^\dagger \hat{a}_i$ for $i = 1,2,3,4$. From the ladder operators for the beamsplitter output in the system of equations 2.70 it can be seen that

$$\hat{n}_3 = |R|^2 \hat{n}_1 + TR^* \hat{a}_1^\dagger \hat{a}_2 + T^* R \hat{a}_2^\dagger \hat{a}_1 + |T|^2 \hat{n}_2, \text{ and} \tag{2.73}$$

$$\hat{n}_4 = |T|^2 \hat{n}_1 + T^* R \hat{a}_1^\dagger \hat{a}_2 + R^* T \hat{a}_2^\dagger \hat{a}_1 + |R|^2 \hat{n}_2. \tag{2.74}$$

With these properties of the ideal beamsplitter presented let us now return our attention to the HBT interferometer to derive the second-order coherence for the case of photons in a Fock state incident on the interferometer. Let us assume an arbitrary Fock state at input port 1 and a vacuum state at port 2 as (see in Figure 2.4b) giving an input product state $|n\rangle_1 |0\rangle_2$ where the subscripts of the kets indicate the port input numbers. With the number operators for the output light in equation 2.73 and 2.74 let us now determine the expectation values $\langle \hat{n}_3 \rangle$ and $\langle \hat{n}_4 \rangle$ at the output ports of the beamsplitter

$$\begin{aligned} \langle \hat{n}_3 \rangle &= \langle 0|_2 \langle n|_1 \hat{n}_3 |n\rangle_1 |0\rangle_2 , \\ &= \langle 0|_2 \langle n|_1 |R|^2 \hat{n}_1 + TR^* \hat{a}_1^\dagger \hat{a}_2 + T^* R \hat{a}_2^\dagger \hat{a}_1 + |T|^2 \hat{n}_2 |n\rangle_1 |0\rangle_2 , \\ &= |R|^2 \langle \hat{n}_1 \rangle . \end{aligned} \tag{2.75}$$

Similarly we have

$$\langle \hat{n}_4 \rangle = |T|^2 \langle \hat{n}_1 \rangle . \tag{2.76}$$

We may also use the number operators $\hat{n}_3$ and $\hat{n}_4$ to evaluate the second-order expectation

$\langle n_3 n_4 \rangle$, that is, the coincidence counts for the HBT interferometer

$$
\begin{aligned}
\langle n_3 n_4 \rangle &= \langle 0|_2 \langle n|_1 \hat{n}_3 \hat{n}_4 |n\rangle_1 |0\rangle_2 , \\
&= \langle 0|_2 \langle n|_1 (|R|^2 \hat{n}_1 + TR^* \hat{a}_1^\dagger \hat{a}_2 + T^* R \hat{a}_2^\dagger \hat{a}_1 + |T|^2 \hat{n}_2)(|T|^2 \hat{n}_1 + T^* R \hat{a}_1^\dagger \hat{a}_2 + R^* T \hat{a}_2^\dagger \hat{a}_1 \\
&\quad + |R|^2 \hat{n}_2) |n\rangle_1 |0\rangle_2 , \\
&= R^* R T T^* \langle 0|_2 \langle n|_1 \hat{a}_1^\dagger \hat{a}_1 \hat{a}_1^\dagger \hat{a}_1 |n\rangle_1 |0\rangle_2 + R^* T R^* T \langle 0|_2 \langle n|_1 \hat{a}_1^\dagger \hat{a}_1 |n\rangle_1 |0\rangle_2 , \\
&= |R|^2 |T|^2 \langle 0|_2 \langle n|_1 \hat{a}_1^\dagger \hat{a}_1 \hat{a}_1^\dagger \hat{a}_1 - \hat{a}_1^\dagger \hat{a}_1 |n\rangle_1 |0\rangle_2 , \\
&= |R|^2 |T|^2 \langle 0|_2 \langle n|_1 \hat{a}_1^\dagger \hat{a}_1^\dagger \hat{a}_1 \hat{a}_1 |n\rangle_1 |0\rangle_2 , \\
&= |R|^2 |T|^2 \langle \hat{n}_1 (\hat{n}_1 - 1) \rangle ,
\end{aligned}
\tag{2.77}
$$

where we have used equation 2.69. From equations 2.75-2.77 it is clear that the HBT interferometer provides a direct measure of the second-order coherence

$$
g^{(2)}(\tau) = \frac{\left\langle \hat{a}^\dagger \hat{a}^\dagger \hat{a} \hat{a} \right\rangle}{\left\langle \hat{a}^\dagger \hat{a} \right\rangle^2} = \frac{\langle n_1 (n_1 - 1) \rangle}{\langle n_1 \rangle^2}. \tag{2.78}
$$

2.2.4 Two-photon Interference: Hong-Ou-Mandel Interferometry

In this subsection, I discuss photon indistinguishability. Quantum networks require high fidelity between quantum processing nodes to allow for the transmission of quantum information across long distances [61]. Therefore, the light emitted from any SQE should be completely inidistinguishable in which no degree of freedom (spatial, temporal, spectral, polarization) can be used to distinguish between the photons emitted from the same or different SQEs. However, due to multiple optical decoherence pathways, SQEs may be limited in their probability of generating indistinguishable photons. To determine that the stream of photons from a SQE or that two SQEs photon streams are indistinguishable, the photons emitted from the SQE(s) must be fed to both input ports of a half-silvered beamsplitter where they interfere at the beamsplitter and form an interference pattern known as Hong-Ou-Mandel (HOM) interference. The visibility of the fringe (the HOM dip) is a

measure of the two-photon indistinguishability [61, 60, 136]. Photon indistinguishability is measured using a HOM interferometer, which, like the HBT interferometer, comprises a 50/50 beamsplitter with equal reflectivity r and transmissivity t, two single-photon detectors and a time tagger.

Single-quantum emitters may have properties that make their photons distinguishable such as phonon sideband emission and spectral diffusion. We, therefore, consider a multi-mode input wave function $\langle\psi_m\rangle$ given by [141]

$$\langle\psi_m\rangle = \langle\phi_1\rangle\langle\phi_2\rangle = A^2 e^{i(\phi_1+\phi_2)} u_{11}u_{22}, \tag{2.79}$$

where $\langle\phi_i\rangle = Ae^{i(\phi_j)}u_{ij}$ are the wave functions for the ith photons incident at the jth input port of the beamsplitter, with the same amplitude A, photon-mode function u_{ij} and ϕ_i is the photon phase at input port j. It can be shown that at the output of the beamsplitter the two-photon wave function is [141]

$$\begin{aligned}\langle\psi_{out,m}\rangle &= A^2 e^{i(\phi_1+\phi_2)}[tr'u_{11}u_{21} + rt'u_{12}u_{22} + tt'u_{11}u_{22} + rr'u_{12}u_{21}], \\ &= A^2 e^{i(\phi_1+\phi_2)}[tr'u_{11}u_{21} + rt'u_{12}u_{22} + (tt' + rr')u^2],\end{aligned} \tag{2.80}$$

where t, r, t' and r' are the transmissivity and reflectivity for the two sides of the beamsplitter, respectively. The first two terms are distiniguishable whereas the last two terms correspond to each output photon going to a separate port. The last two terms are indistinguishable if they are summed and their photon modes are equal: $u_{1j} = u_{2j} = u$ [141]. These terms are illustrated in Figure 2.5a. Due to energy conservation from the input to output of a 50/50 beamsplitter the phases of the reflectivities and transmissivities satisfy $\phi_t + \phi_{t'} - \phi_r - \phi_{r'} = \pi$. Hence for a half-silvered beamsplitter we have the following relation

for the last two terms in equation 2.81

$$
\begin{aligned}
A^2 e^{i(\phi_1+\phi_2)}(tt' + rr')u^2 &\propto tt' + rr', \\
&= e^{i(\phi_r+\phi_{r'})}[e^{i(\phi_t+\phi_{t'}-\phi_r-\phi_{r'})} + 1]/\sqrt{2}, \\
&= e^{i(\phi_r+\phi_{r'})}[e^{i\pi} + 1]/\sqrt{2}, \\
&= 0
\end{aligned}
\tag{2.81}
$$

and thus due to destructive interference the last two terms in in equation 2.81 sum to zero and no photons are observed at the output ports of the beamsplitter [141]. This result is due to the cancellation of the output phases of the photons and thus, the indistinguishability of photons is dependent entirely on the similarity of the photon modes.

Experimentally, indistinguishability is measured with a HOM interferometer in which the coincidence counts are recorded for the photons output from the beamsplitter. We would expect for the case of two ideal SQEs, whose photons are incident on a HOM interferometer that no coincident counts, save for background counts, would be recorded. However, for a non-ideal SQE photon indistinguishability requires the overlap of all modes (spatial, temporal, polar, etc.). For example, if the delay between input arms is nonzero then the temporal mode of the two input photons will not overlap and the counts coincident within some time window (*i.e.* the coincident counts) will increase. If we sweep this delay we will observe an interference fringe known as a HOM dip, which is a key signature of photon indistinguishability [141] as seen in Figure 2.5b.

For a SQE that emits all photons in the same spatial mode, we may only consider its spectral mode as having an effect on photon indistinguishability. When a SQE is Fourier-limited in its spectral linewidth, each photon can be described with the same coherent spectral mode, then any photons the SQE emits are indistinguishable. When SQE emitted photons have Fourier-limited linewidths the emission spectrum is equivalent to the Fourier transform of its time-resolved photoluminescence with linewidth $1/2T_1$, where T_1 is the

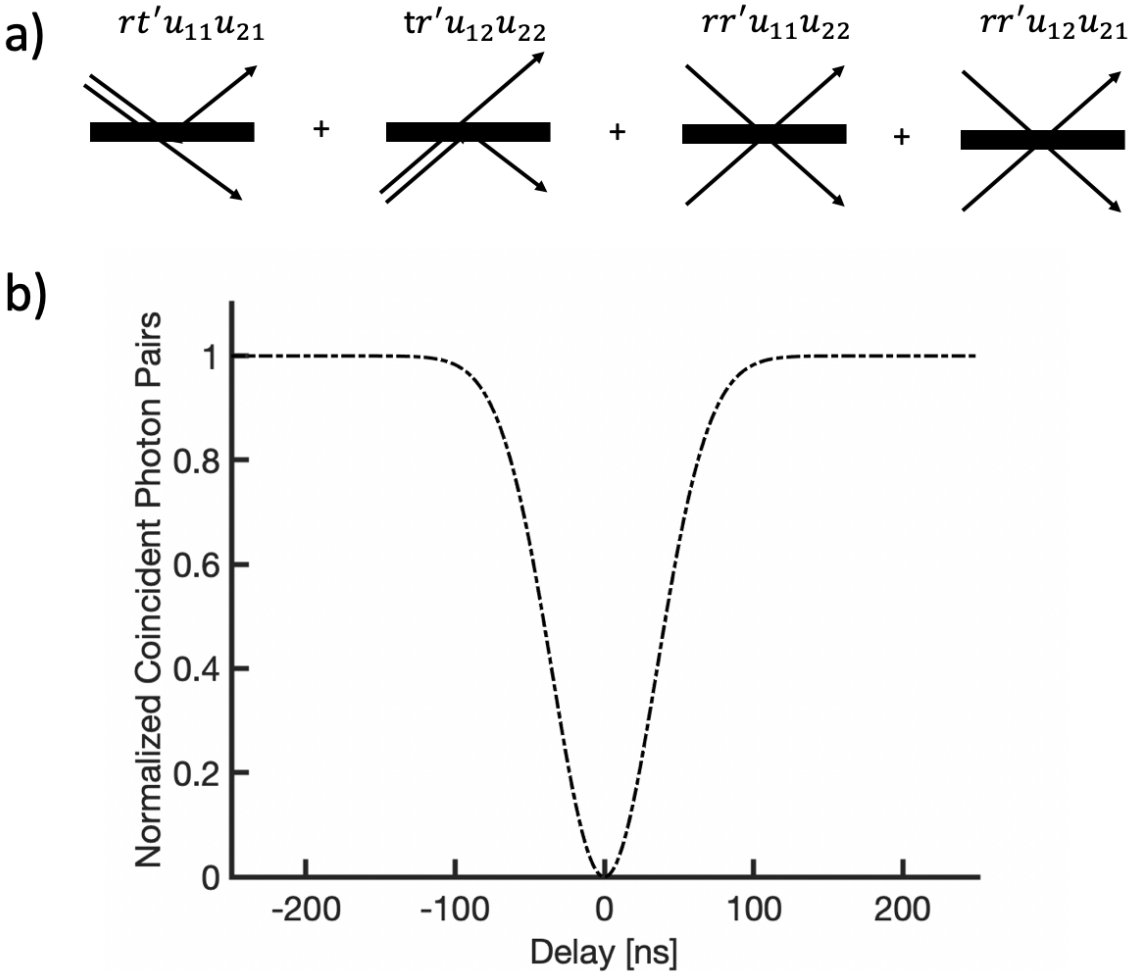

Figure 2.5: Two-Photon Indistinguishability. a) The four possible trajectories for the two photons in a HOM interferometer. b) The HOM dip of coincident counts is a function of the relative delay between single-photon wave packets

optical lifetimes of the SQE. Unlike the case in which a SQE exhibits pure spontaneous emission and thus emits indistinguishable photons, optical decoherence degrades the indistinguishability expected for an SQE. In these cases, the linewidth of the spectral mode is broader than the Fourier-transform of the time-domain profile of the emitted photons [142]. This broadening is due to fluctuation in the resonant frequency and can be due to dephasing, or spectral diffusion. We will now briefly discuss these decoherence mechanisms, their properties and how they specifically degrade photon indistinguishability.

First, interactions of an SQE with a bath of phonons cause the state vector to lose phase

as a function of time along the Bloch sphere transverse plane with dephasing time constant T_2. The dephasing time constant is related to the SQE optical lifetime by

$$1/T_2 = 1/2T_1 + 1/T_2^*, \tag{2.82}$$

where T_1 is the optical lifetime of the SQE and T_2^* is the pure dephasing due to interactions with a phonon bath [142]. Second, spectral diffusion is the drifting or jumping in the optical frequency due to interactions with the dipole moment of the SQE. This leads to photons emitting into different spectral modes and thus are distinguishable [142]. Spectral diffusion may be negligible in its dephasing contribution only in the case where the delay between emitted photons is shorter than the spectral diffusion time.

2.2.5 The Photon Emission Rate and Quantum Efficiency of SQEs

In this final subsection we focus on the photon emission rate and the intrinsic quantum efficiency of an SQE ignoring extrinsic optical efficiency, which degrades the quantum efficiency due to optical losses in the collection path of a confocal microscope, for example. As we have seen in subsections 2.2.3.4 and 2.2.3.5 the photophysics for color centers is generally well explained using simplifying two- or three-level models. In the case of an SQE modeled as having only two atomic states we presume that the excitation rate k_{12} and the excitation power P_{exc} are proportional with

$$k_{12} = \beta P_{exc}, \tag{2.83}$$

where β is a constant. The product of the equilibrium population $\rho_{22}(\infty) = k_{21}/(k_{12} + k_{21})$ of the excited state $|2\rangle$ and the excitation pumping rate k_{21} gives the photon emission rate I_R

$$I_R(P_{exc}) = \frac{k_{21} P_{exc}}{P_{exc} + P_{sat}}, \tag{2.84}$$

where $P_{exc} = k_{12}/\beta$ and $P_{sat} = k_{21}/\beta$ is the saturation power in which I_R is linear with P_{exc} when $P_{exc} < P_{sat}$ and I_R approaches the asymptotic limit of k_{21} otherwise, (*i.e.* power saturation).

For a SQE modeled as a three-level system there are additional non-radiative decay pathways k_{23} and k_{31} associated with the shelving state. Solving the rate equations in 2.51-2.54 and taking the steady-state limit for the excited state population gives

$$\rho_{22}(\infty) = \frac{k_{21}}{k_{12}/\kappa + k_{21} + k_{23}}, \tag{2.85}$$

where $\kappa = (1 + k_{23}/k_{31})^{-1}$. We again assume linear dependence on power and the excitation rate and also define $P_{sat} = (\kappa/\beta)(k_{21} + k_{23})$. We now can state the photon emission rate for a three-level model as

$$I_R(P_{exc}) = \frac{\kappa k_{21} P_{exc}}{P_{exc} + P_{sat}}. \tag{2.86}$$

The factor κ has the effect of slowing the emission rate i) when $k_{23} > 0$ and ii) by greater than half of k_{21} when $k_{23} > k_{31}$.

The quantum efficiency for any SQE is the radiative decay rate normalized to the sum of the radiative and non-radiative decay rates

$$Q_{Eff} = \frac{\Gamma_{rad}}{\Gamma_{nrad} + \Gamma_{rad}}. \tag{2.87}$$

For the two-level model there are no or negligible non-radiative pathways assumed and the quantum efficiency is assumed to be 100%. For the three-level model we have radiative decay, k_{21} and non-radiative decay rates k_{23} and k_{31} and the quantum efficiency is given by

$$Q_{Eff} = \frac{k_{21}}{k_{21} + k_{23} + k_{31}}. \tag{2.88}$$

Chapter 3

Background in Hexagonal Boron Nitride SQEs

Color centers in hexagonal boron nitride (hBN) are a promising platform for SQEs and solid-state quantum memories. As noted in chapter 1, their primary advantages are their brightness, their photostability at room temperature and their optically accessible spin states. However, the inability to identify the atomic structure of experimentally observed defects has delayed progress in i) identifying the Hamiltonian of experimentally observed defects and ii) controlling these defects for SQE and quantum memory applications. In this section, we will review hBN as a host material for defects. We will also review the following properties of hBN defects: electron-phonon coupling, emitter categorization, excited-state structure, ZPL temperature dependence, spin properties and excitation mechanisms.

3.1 Hexagonal Boron Nitride as a Host Material for Defects

Hexagonal boron nitride is an insulating layered white material where each boron and nitrogen atom is sp^2 hybridized forming a honeycomb lattice structure with lattice constants $a = b = 0.2504$ nm and $c = 0.665$ nm [143]. The bond structure between the nitrogen and boron atoms are polar covalent bonds due to the difference in electronegativity between nitrogen and boron. There are no direct bonds between layers and instead, weak van der Waals interactions loosely bond each layer to the other. Furthermore, since hBN is a van der Waals material, SQEs can be integrated into heterostructures. In addition to these properties, hBN has a large and indirect bandgap of 5.96 eV [144]. Hence a momentum mismatch between the valence and conduction bands requires either a phonon or a crystallographic defect interaction to overcome the momentum mismatch. However, this large bandgap allows for photostable visible and near-infrared SQEs to be formed deep in the bandgap of hBN. The Raman accessible LO(Γ) phonon mode in hBN is a key signature of the layer thickness with monolayers (1,367.5 cm^1), multilayers (1,366.6 cm^1)

and bulk Raman (1,365.1 cm^1) shifts reported [145]. Additionally the ~169 meV and the 199.6 meV LO(Γ) modes [146] have peak energies consistent with observed peak optical phonon-sideband in hBN defects [145, 147]. However, due to the poor understanding of the identity of hBN defects, local modes cannot be ruled out as sources of optical-phonon sideband emission.

3.2 Electron-Phonon Coupling in hBN Emitters

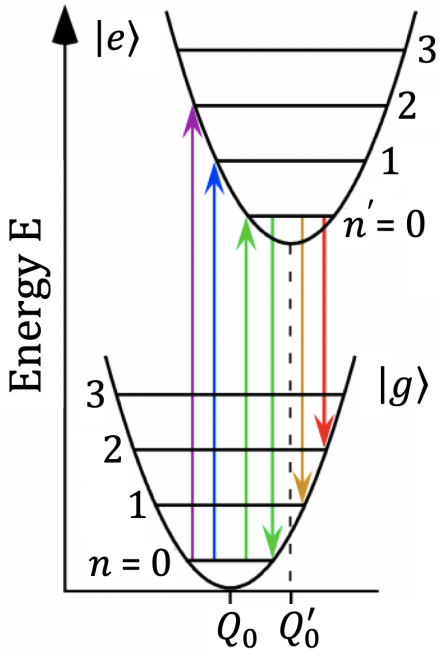

Figure 3.1: Configuration coordinate diagram for a two-level emitter, adapted from [1]

Defect photoluminescence is due to radiative transitions between electornic states and how these states couple to localized vibrational modes and lattice phonons. This can be explained with the use of a coordinate diagram as shown in Figure 3.1. Here we plot the potential energy for the ground and excited state of a two-level defect with respect to the nuclear coordinate describing the lattice configuration. Both the ground $|g\rangle$ and excited $|e\rangle$ electronic states are coupled to the vibrational energy levels of the lattice $|n\rangle$ and $|n'\rangle$, respectively. At a temperature of absolute zero the defect is in the ground electronic and vibrational states $|g\rangle|n = 0\rangle$. Relative to the ZPL nuclear coordinate Q_0 for the ground

state $|g\rangle|n=0\rangle$ the nuclear coordinate is displaced to Q_0' due to each state having different electrostatic potentials, which deform the lattice [1]. An input photon may pump the defect into the excited state $|e\rangle|n'\rangle$ via a vertical transition that occurs immediately without altering the defect or lattice geometries according to the Born-Oppenheimer approximation. The defect then quickly thermalizes to the vibrational ground state $|e\rangle|n'=0\rangle$ and the defect may then relax via radiative decay from the $|e\rangle|n'=0\rangle$ to the $|g\rangle|n\rangle$ state with a probability given by the overlap integral between the n- and n'-phonon wavefunctions, known as the Frank-Condon factor $F_n^{n'}$. If we assume only linear vibrational modes are present ($f=f'$) then the $F_n^{n'}$ is given by

$$F_n^{n'} = e^{-S} S^{n-n'} \frac{n'!}{n!} (L_n^{n-n'}(S))^2 \tag{3.1}$$

where the strength of the electron-phonon coupling between the defect and the lattice is given by the Huang-Rhys factor S, and $L_n^{n-n'}$ are Laguerre polynomials [1]. At zero kelvin the phonons in the excited state $|e\rangle|n'\rangle$ are depleted and $n'=0$. The overlap integral then becomes $F_n^{n'} = e^{-S} S^n/n!$. The distribution of the phonons created during radiative decay to the ground state is described by a Poisson distribution with mean S. The spectral weight of the ZPL, the Debye-Waller Factor at zero kelvin, is then e^{-S}.

Microphotoluminesence microscopy can be used to evaluate the electron-phonon coupling and to determine the peak phonon modes of an emitter. For hBN emitters, optical one-phonon energies of 160±5 and 200±5 meV redshifted from the ZPL have been observed [148, 2]. For ultraviolet defects these phonon energies have been attributed to $TO(M)/LO(K)$ and zone center $LO(\Gamma)$ optical phonons, respectively [148]. Here TO(X) and LO(X) are transverse or longitudinal optical phonons located at the critical point X in the Brillouin zone. For the 200 meV phonon, it was assumed that optical phonons centered in the Brillouin zone (zone center) couple to the electron through the Frolich interaction. The interaction scales as the inverse of the phonon wave vector leading to a singularity in

the electron-phonon matrix element for $LO(\Gamma)$ phonons causing a large transition at 200 meV redshifted from the ZPL despite the negligible density of states for $LO(\Gamma)$ phonons in hBN. However, this argument does not consider the local modes of the defect. Efforts have been made to identify the local vibrational modes of hBN defects using first-principle density functional theory assuming carbon- or nitrogen-based color centers [125]. But to date calculated local modes do not agree with experimentally observed peak phonon energies from photoluminescence spectra.

3.3 Phenomenological Categorization of Emitters: Group I and Group II

Recent optically detected magnetic resonance (ODMR) studies have reported i) defects with a ground state triplet and ii) carbon related defects as having optically addressable spin identifying the negatively charged boron vacancy (V_B^-) and the negatively charged carbon defect ($V_B C_N^-$) as defect candidates, respectively [100, 123]. However, to date, the atomic structure of experimentally observed defects in hBN has yet to be determined conclusively through transmission electron microscopies. This leaves the electronic states for the majority of experimentally observed defects poorly understood. While currently, and in general, it is infeasible to determine the selection rules and the Hamiltonian of a given hBN defect, the community has instead resorted to a phenomenological classification of defects into two groups (I and II) based on their observed electron-phonon coupling, the linewidth of the zero-phonon line (ZPL), and the energy range of the ZPL as shown in Figure 3.2. Group I emitters exhibit a stronger electron-phonon coupling than group II emitters with a pronounced one-phonon sideband doublet, and an asymmetric ZPL as shown in Figure 3.2a ZPL [2].

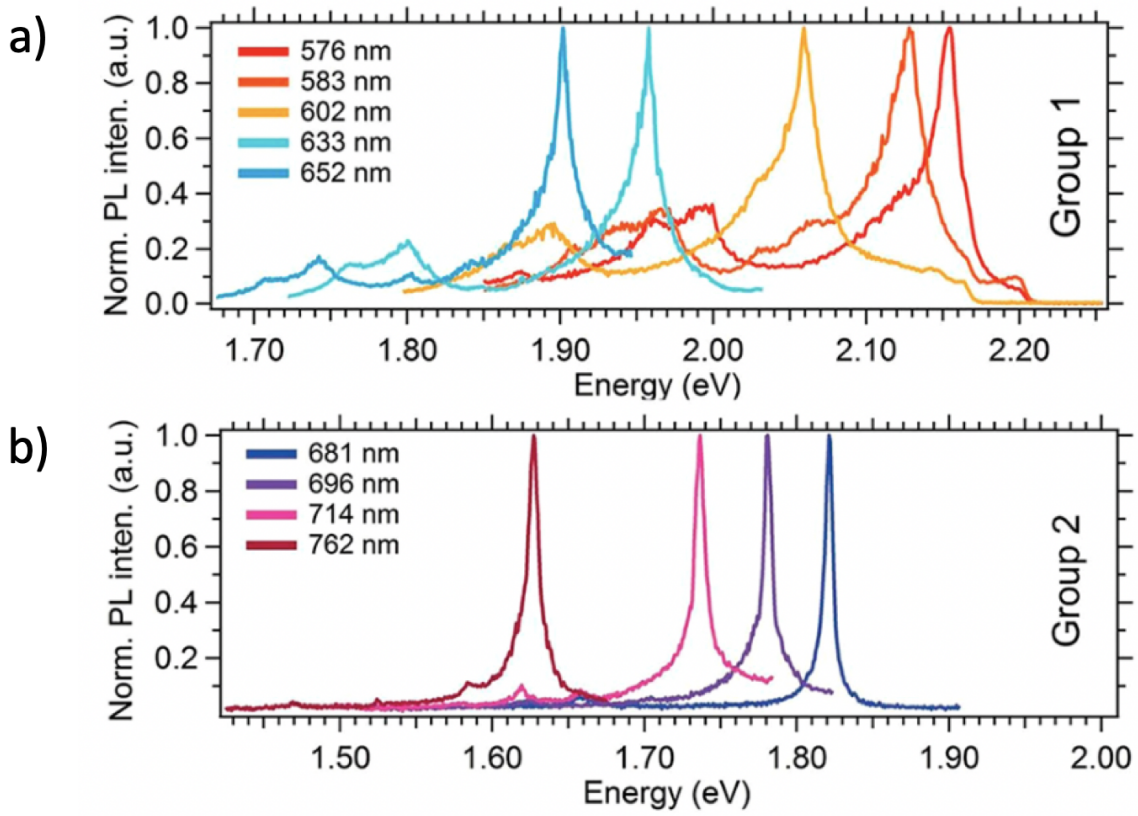

Figure 3.2: Microphotoluminesence classification of hBN emitters. a) Spectra of group I emitters at room temperature have asymmetric ZPLs with broad linewidths and a prominent phonon sideband. b) Spectra of group II emitters at room temperature have a symmetric ZPLs with narrow linewidths and up to 80% of the emission into the ZPL. This figure was adapted from [2]

The electron-phonon coupling strength is quantified by the Huang-Rhys factor S, and the probability of emitting into the ZPL is given by the Debye-Waller factor $l = e^{-S}$, which ranges from 0.15-0.60 for group I emitters. The peak energy of the ZPL for group I emitters ranges from 1.8-2.6 eV and has linewidths ranging from 0.08 to 0.35 meV at 4K [149, 2]. Group II emitters (see Figure 3.2b) have much less pronounced phonon sidebands with Debye-Waller factors ranging from 0.50 to 0.80. Their ZPL peak energies are in the near-infrared range (1.4-1.8 eV) and their ZPL linewidths are narrower ranging from 0.04 to 0.08 meV [149, 2]. For both group I and group II emitters the peak energy of the one-phonon sideband is at 160±5 meV meV [2, 148].

Additionally, group I and II emitters exhibit shelving peaks in the photon statistics

indicating the presence of metastable shelving states [121, 2]. Here the shelving state is the third state in the three-level model for an SQE. For group I emitters, the presence of multiple metastable states has been observed in recent photophysics studies where two shelving states were found to exist based on best fits to rate equation models for second-order coherence statistics using a χ^2 comparison test of models with 1,2 and 3 shelving states [121]. Group II emitter photophysics have yet to be studied in rigorous detail, but initial reports of second-order coherence at long time scales indicate the presence of more than one shelving state with shelving lifetimes ranging from $\sim$ 10 to $\sim$ 10000 ns [2].

3.4 Electronic Structure of hBN Emitters

Initial experiments on group I and II hBN emitters indicate the existence of a third excited state. Polarimetry experiments reported a misalignment in their absorption and emission dipole moments implying an indirect excitation pathway and at least two excited states [105, 107]. The existence of a complex excited state structure is also supported by a study where discrete spectral jumps $\sim$ 100 nm were observed under 405 nm excitation whereas a small fraction of defects emits upon 532 nm excitation [150].

To date, two studies have investigated the existence of multiple excited states in a cross-section of group I hBN emitters. The first is a survey of polarimetry on hBN emitters whose results fail to be supported by a Huang-Rhys model involving two electronic states [1]. The second is a study evaluating the effects of global strain. This study has shown a strain-dependence of the misalignment angle between absorption and emission dipoles requiring a three-level model to explain the wide range in which strain can tune the ZPL of hBN SQEs [123]. In this section, we will review these two topics and their relevance for future studies of the excited state structure in hBN defects.

In [1] spectrally resolved optical absorption and emission polarimetry was collected at cryogenic temperatures on single defects in hBN with $g^{(2)}(\tau) < 0.5$. The observed emission and absorption dipole moments were compared to a Huang-Rhys two-level model as a

function of the phonon energy for each defect. The aligned emission and absorption dipole moments are found to agree with the two-level Huang-Rhys model when the difference between the excitation light (E_{exc}) and the ZPL (E_{ZPL}) is less than the maximum phonon energy [1]. However, when $|E_{exc} - E_{ZPL}|$ exceeds the maximum phonon energy the two-level model fails to explain the emission and absorption dipole alignment, which implies a third excited state mediates the ZPL emission.

In an extensive survey of hBN defects, it was found that absorption and emission dipole moments of hBN defects were aligned when spectrally filtering on energies below the maximum one-phonon sideband energy [1]. But the dipole moments were misaligned up to 90^{o} when filtering on energies above the one-phonon sideband in disagreement with the Huang-Rhys model suggesting a third excited state is required to explain the observed misalignment. However, in the higher-energy regime defects were observed that did not have their dipoles misaligned. This could be due to a difference in the absorption cross-section coupling to the excitation light. To test this, polarimetry was conducted on the same ZPL when excited by a 532 nm and 473 nm laser. It was found that for the 532 nm case the dipoles were aligned whereas for the 473 nm case the dipoles were misaligned by 50^{o} [1]. This confirms that laser detuning can induce direct or indirect electron absorption in hBN point defects.

Recent strain-induced photophysics studies have also supported the existence of a third state in a subset of hBN emitters [123]. In that study, the emission dipole orientation and ZPL energy were found to be dependent on the applied tensile strain. Furthermore, the reorientation of the emission dipole cannot be explained using a model for the linear static strain involving only two states. Instead, the existence of a third state is assumed, having the same spin multiplicity as the ground and first excited states. With this three-level model, it is determined that the mixing between the second excited and the first excited and ground states in the strain potential is responsible for the tunable dipole misalignment.

3.5 Temperature dependence of the ZPL

The zero-phonon lines peak energy and linewidth temperature dependence have been investigated [151, 152]. A redshift and broadening of the ZPL linewidth have been observed when heating group I and group II emitters from 4 to 300K [151]. An additional study confirmed this redshift and broadening by heating from 300 to 800K and found both to be reversible [152]. It has been proposed that the redshift in the ZPL is due to the expansion of the lattice upon heating. Whereas the broadening of the ZPL linewidths has been attributed to piezoelectric coupling to acoustic phonons to account for the exponential temperature dependence of the ZPL linewidth [151]. Impressively, the photostability of the defect emission is maintained even at exceedingly high temperatures (800K) [152].

3.6 Spin Properties of Defects in hBN

An understanding of the spin properties of solid-state defects is necessary to control and detect spin states for use as quantum memories. In this section, I review the mangeto-optical and spin properties of SQEs in hBN. In initial work species of hBN SQE were found to be nonmagnetic exhibiting no Zeeman splitting in the ground state manifold when the SQE is placed in a static magnetic field [99]. These SQEs were shown to be spatially overlapped with structural defects in hBN and having narrow ZPLs consistent with the group II emitter classification [99]. However, additional work has shown that a few percent of emitters surveyed do exhibit a magnetic field-dependent anisotropy in their photoluminescence, while the remaining SQEs have no magnetic properties [104]. A magnetic field-dependent modulation in the intensity of these select SQEs is indicative of optically addressable spin states, although there is a lack of any observable Zeeman interaction. Both of these points are consistent with a spin-dependent intersystem crossing between a singlet-ground and triplet-excited states [104].

However, recent optically detected magnetic resonance (ODMR) experiments have reported a defect ensemble in neutron-irradiated bulk-hBN crystals with a triplet-ground

state. The triplet nature of the ground state was confirmed by clear evidence of a Zeeman interaction, zero-field splitting and microwave-driven transitions between the $m_s = \pm 1$ and $m_s = 0$ levels inducing spin-dependent optical contrast (dimming of the photoluminescence) [100]. This defect is identified as the negatively charged boron vacancy ($V_B{}^-$) given that theory has predicted the $V_B{}^-$ to have a, i) positive zero-field splitting (D) [153], ii) D_{3h} symmetry with a C_3 axis parallel to the c-axis of the hBN crystal [153, 118], and iii) S = 1 triplet ground state with a spin-dependent intersystem crossing [153], which are consistent with the findings in recent electron paramagnetic resonance and ODMR experiments [100, 103].

In contrast with these observations, recent experiments on carbon implanted bulk-hBN have verified that group II emitters exhibit optically accessible spin states via ODMR studies and that the emission for visible SQEs in hBN is in part due to carbon related defects [154]. In the same paper time-domain density functional theory further indicates that the defect is likely the negatively charged $V_BC_N^-$ defect. To date, the effect of the dimensionality (bulk-hBN, monolayer-hBN) has on the energetics for the $V_BC_N^-$ and $V_B{}^-$ defects has yet to be explored.

3.7 Excitation Mechanisms for hBN Defects

In this section, we will review the excitation schemes used to drive hBN defects into their excited state(s). The collection scheme used nominally is an off-resonance excitation [145, 155] usually consisting of a 532 nm continuous wave laser. To separate the photoluminescence from the laser only a low-pass filter or dichroic mirror is necessary. While this approach is simple it can excite fluorescent background leading to degradation in the SQE purity. This is due to the small cross-section of off-resonant light that excites the SQE. Furthermore, off-resonant excitation schemes cannot coherently control the state of the SQE and instead the SQE spontaneously emits photons. A specialized form of off-resonant excitation is Antistokes driving, which has been shown to partially miti-

gate the effects of spectral diffusion [156]. In this case, the pumping wavelength drives the SQE such that the transition for the excited electronic state is mediated by lower-energy vibronic states. This enables the effective cross-section of surface-charges being excited, which causes spectral diffusion, to be reduced. This is because the effective cross-section usually increases with increasing excitation energy [156]. Alternatively, resonant excitation [106] can be employed to i) improve the SQE purity and ii) drive the SQE coherently to control the quantum state of the SQE. Filtering the laser light from the SQE PL is done by either i) collecting only the phonon-sideband using bandpass filters or ii) cross-polarizing the laser and PL.

Chapter 4

Phonon-induced multi-color correlations in hBN single-photon emitters

In this chapter I will address characterizing the electron-phonon coupling of hBN defects. I will model the electron-phonon coupling evident in photoluminescent spectra of a hBN defect thereby characterizing the phohon modes coupled to the defect orbital. I will then use two-color HBT interferometry to show that all the phonon modes and the ZPL are cross correlated with one another as expected for the vibronic modes of a defect. This is the first confirmation of phonon sideband emission using HBT interferometry.

Matthew A. Feldman[1,2], Alex Puretzky[3], Lucas Lindsay[4], Ethan Tucker[2], Dayrl P Briggs[3], Philip G. Evans[2], Richard F. Haglund[1], and Benjamin J. Lawrie[2]

[1]Department of Physics and Astronomy, Vanderbilt University, Nashville, TN 37235, USA

[2]Quantum Information Science Group, Oak Ridge National Laboratory, Oak Ridge, TN 37831, USA

[3]Center for Nanophase Materials Sciences, Oak Ridge National Laboratory, Oak Ridge, TN 37831, USA

[4]Materials Science and Technology Division, Oak Ridge National Laboratory, Oak Ridge, TN 37831, USA

The following work has been accepted by Physical Review B [108] and is reprinted below in its entirety.

4.1 Abstract

Color centers in hexagonal boron nitride have shown enormous promise as single-photon sources, but a clear understanding of electron-phonon interaction dynamics is criti-

cal to their development for quantum communications or quantum simulations. We demonstrate photon antibunching in the filtered auto- and cross-correlations $g^{(2)}_{lm}(\tau)$ between zero-, one- and two-phonon replicas of defect luminescence. Moreover, we combine autocorrelation measurements with a violation of the Cauchy-Schwarz inequality in the filtered cross-correlation measurements to distinguish a low quantum-efficiency defect from phonon replicas of a bright defect. With no background correction, we observe single photon purity of $g^{(2)}(0) = 0.20$ in a phonon replica and cross-spectral correlations of $g^{(2)}_{lm}(0) = 0.18$ between a phonon replica and the zero phonon line. These results illustrate a coherent interface between visible photons and mid-infrared phonons and provide a clear path toward control of photon-phonon entanglement in 2D materials.

4.2 Introduction

The recent discovery of a wide class of defect-based single photon emitters (SPEs) in hexagonal boron nitride (hBN) has spurred significant interest in the development of two-dimensional (2D) materials and van der Waals heterostructures [145, 155, 107, 98, 157, 152]. Defects in hBN have narrow linewidths [157], bright emission [145], small Huang-Rhys factors [145, 107], and are stable at temperatures as high as 800K [152]. Stable SPEs in hBN thus far have only been categorized phenomenologically into two groups on the basis of the phononic contributions to their spectra. Group I color centers have an asymmetric zero-phonon-line (ZPL) sideband [105, 155] and a doublet optical phonon sideband redshifted $\sim 160(5)$ meV from the ZPL [145, 105, 158, 150, 159, 155, 152]. Group II defects have a symmetric ZPL and less pronounced optical phonon sidebands [155].

The state structure of hBN defects, the large variance in ZPL energies, and the electron-phonon dynamics and energetics remain poorly understood. Improved understanding of these properties will drive the development of 2D hybrid quantum systems that leverage quantum coherent photonic and phononic interactions to generate indistinguishable single photons and to enable quantum frequency conversion [148]. Coherent phonon-emitter cou-

pling has been explored in depth for diamond color centers, resulting in the observation of phonon-mediated photon bunching [160], quantum teleportation from photonic to phononic states [161], phononic quantum memories suitable for storing single photons [162, 163], and room-temperature phononic quantum processing [164].

In this Letter we explore the electron-phonon dynamics of group I defects in few-layer hBN with one- and two-color Hanbury Brown-Twiss (HBT) interferometry and micro-photoluminescence (μPL) spectroscopy. We provide the first evidence of single-phonon excitation and photon-phonon entanglement in 2D materials by measuring antibunching in the one- and two-phonon replicas of a hBN color center and we use violations of the Cauchy-Schwarz inequality in two-color cross-correlation measures to distinguish low quantum-efficiency defects from phonon replicas of bright defects. These measurements demonstrate that hBN is an ideal platform for generating single mid-infrared phonons by optical excitation because of the weak electron-phonon coupling in hBN compared with diamond. This is a critical step toward the realization of deterministic single-phonon sources and acoustic quantum transducers that have been proposed in recent years [165, 166].

4.3 Results & Discussion

We used a custom confocal microscope to excite color centers in hBN with a 405 nm CW source. Nineteen group I defects with ZPLs varying from 1.7-2.7 eV were surveyed [167] with μPL and HBT interferometry, and a single defect exhibiting minimal coupling to other defects was chosen for more detailed spectroscopy. Background corrected μPL spectra were collected at temperatures of 3.6K and 300K, photon antibunching was measured for each transition identified in the μPL spectra, and photon cross-correlations were measured for each pair of transitions. Further details on the experimental apparatus are available in the supplemental material [167]. As seen in Fig 5.1 and Fig 5.2(a), the group I defect examined here has a ZPL at 2.21 eV with a linewidth that broadens from 1.3 to 20 meV with increasing temperature, consistent with a temperature-dependent

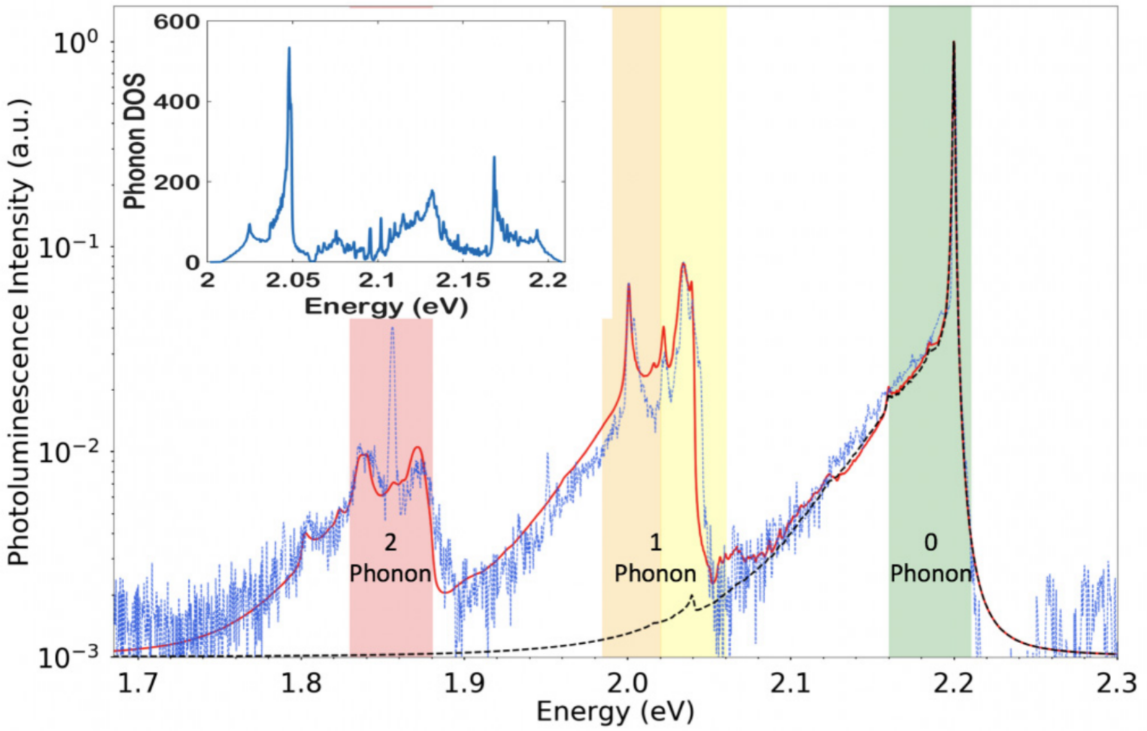

Figure 4.1: Background corrected defect μPL spectrum (blue) collected at 3.6 K, calculated μPL with (red dashed curve) and without (black curve) Lorentzian filters. The calculated one-phonon DOS is shown in the inset. The μPL spectrum calculated with the one-phonon DOS and Lorentzian filters approximating the selection rules present in this material provides a reasonable reproduction of the ZPL and the one-phonon replicas, but an additional transition appears in the experimental μPL spectrum that is not present in the calculated filtered two-phonon replicas

Debye-Waller factor associated with acoustic phonons [105]. hBN defects with ZPLs near 2.21 eV remain poorly classified[168], but the results discussed here are relevant to broad classes of defects in hBN. Phonon sidebands were observed redshifted by 166, 177, 200, 326, 343, 359 and 395 meV from the ZPL in agreement with Raman spectroscopy, inelastic x-ray scattering experiments and ab initio calculations of the phonon dispersion for hBN [169, 170, 171, 172, 173].

In order to explain the vibronic structure of a specific defect, both localized defect vibrations and delocalized lattice vibrations should be considered. Although lattice phonons are well defined, the defect vibrational modes that are determined by defect structure and composition are not. Even in the case of known defects, such calculations are challenging even for hBN monolayers [109]. Here we will consider a limiting case assuming that the main contribution to the vibronic spectrum is given by lattice phonons. As we show below, this assumption provides a reasonably good agreement between the measured and calculated spectra.The inset of Fig. 5.1 illustrates the calculated one-phonon hBN density of states (DOS). The TO(M)/LO(K) (166 meV) and LO(T) (177 meV) phonon modes in the phonon DOS are also well-defined in the measured PL spectrum. The measured single-phonon replica 200 meV to the red of the ZPL can be described as a result of a Fröhlich interaction that scales inversely with the phonon wavevector so that even in the case of small single-phonon DOS, a diverging electron-phonon matrix element results in a significant LO(Γ) phonon replica at 200 meV [148]. Two-phonon replicas were observed redshifted from the ZPL by 326 meV (2TO(M)/2LO(K)), 343 meV (LO(T) + TO(M)/LO(K)), 359 meV (LO(Γ) +TO(M)/LO(K)) and 395 meV (2LO(Γ)).

In order to better validate this description of the μPL spectrum, we modeled each phonon replica in terms of a change in vibronic state at a rate modeled by Fermi's golden rule. We describe excited $\widetilde{i} = |E,m\rangle$ and ground $\widetilde{f} = |G,n\rangle$ vibronic states, where m and n are the vibrational states of the lattice, and the electronic dipole operator μ is assumed to be independent of the nuclear coordinates. The emission spectrum cross-section is then

proportional to the transition rate from $|E,m\rangle$ to $|G,n\rangle$

$$\sigma(\omega) = \frac{16\pi^2 c}{\hbar\omega}|\langle\widetilde{f}|\mu|\widetilde{i}\rangle|^2\delta(\omega_{\widetilde{fi}}-\omega), \tag{4.1}$$

which can be approximated to first order as

$$\frac{8\pi c|\mu|^2}{\hbar\omega}e^{-S}\int_{-\infty}^{\infty}dte^{it(\omega_{GE}-\omega)}e^{S\zeta(t)}, \tag{4.2}$$

where $\zeta(t)$ is given by

$$\int d\Omega(\rho(\Omega)/\Omega^2)[(n(\Omega)+1)e^{i\Omega t}+n(\Omega)e^{-i\Omega t}], \tag{4.3}$$

where ω is the emission frequency, ω_{EG} is the frequency of the electronic transition, Ω is the vibrational frequency, H_G and H_E are the nuclear Hamiltonians for point defects in the ground and excited states, and μ is the matrix element of the electric dipole operator of the point defect [174, 175, 176]. S is the Huang-Rhys factor, $n(\Omega)$ the thermal average number of phonons and $\rho(\Omega)$ the total density of phonon states. For our calculation of the emission spectrum, the empirically determined Huang-Rhys factor (S), a phenomenological term accounting for the observed acoustic phonons [107, 148], and the calculated one-phonon density of states shown in the inset of Fig 5.1 were used to approximate $\rho(\omega)$. Based on experimental observation, we assumed that the TO(M)/LO(K) (166 meV), LO(T) (177 meV), and LO(Γ) (200meV) modes were the dominant one-phonon modes. Hence, the calculated one-phonon density of states was re-weighted using three Lorentzians centered at each of these one-phonon modes. The calculated emission spectrum, plotted in Fig 5.1, reproduces all of the essential features of the experimental spectrum except for the measured feature 343 meV redshifted from the ZPL. Further details on the emission spectrum cross-section may be found in the supplemental material [167].

For a single defect, the selection rules determined by μ allow transitions of only one

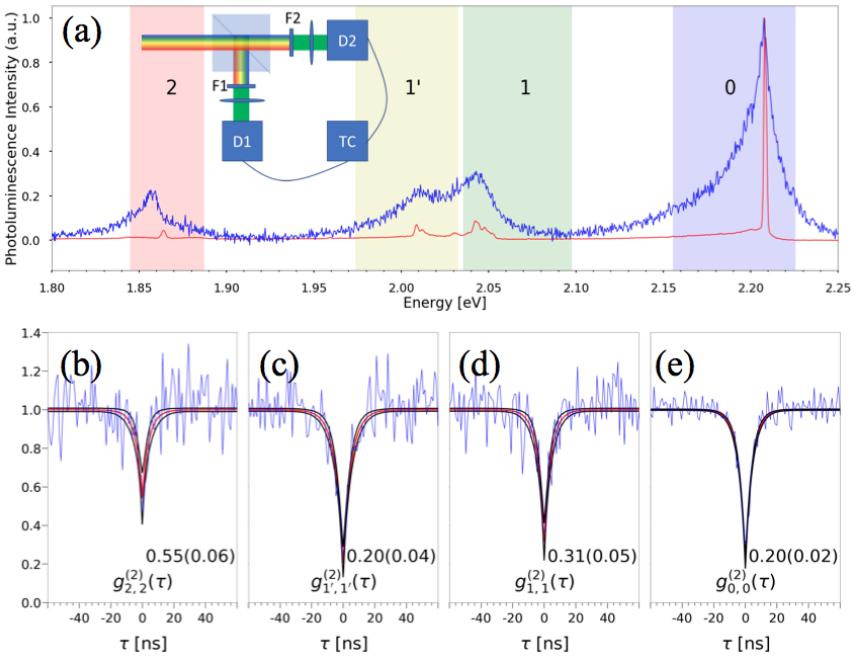

Figure 4.2: (a) Background corrected room temperature (blue) and 3.6K (red) PL spectrum of a hBN defect (the inset illustrates a HBT interferometer with two single-photon detectors (D1 and D2), tunable bandpass filters (F1 and F2), and high speed time correlation electronics (TC)). The filters are actively tunable from 1.75-2.95 eV, enabling spectrally-resolved single photon detection across the bandwidth of all observed SPEs. (b-e) Frequency-filtered two-photon autocorrelations $g_{ll}^{(2)}(\tau)$ (blue), median fits (red), and 95% credibility intervals (black) for the two-phonon replicas (2), LO(Γ) and LO(T) replicas (1′), TO(M)/LO(K) replicas (1), and ZPL (0), respectively. The colored bands (0,1′,1,2) in (a) are the spectral ranges of the bandpass filters used for each of the autocorrelation measurements in (b-e). The mean and standard deviation for $g_{ll}^{(2)}(0)$ are inset in panel (a)-(e).

electron from $|E,m\rangle$ to $|G,n\rangle$ within the coherence lifetime of the electron. Hence this indicates that all transitions $|E,m\rangle$ to $|G,n\rangle$ should be strongly anti-correlated, while a mid-infrared phonon should be strongly correlated with each phonon replica. However, background luminescence, uncorrelated color centers, and incoherent coupling dynamics can all suppress the expected correlations. Hence, we next investigate the correlation dynamics experimentally using colored-HBT interferometry to measure $g^{(2)}_{lm}(\tau)$ for phonon mediated transitions l and m.

For the colored HBT experiments, tunable bandpass filters with bandwidth of 20 nm were used to select the ZPL, one- and two-phonon sidebands. While low-temperature PL was used to map the phonon replicas to the phonon DOS in Fig. 5.1, all auto- and cross-correlation measurements employed room-temperature PL to maximize photon collection efficiency and minimize the excitation spot size for spatially-selective defect excitation. Figure 5.2a illustrates the room-temperature photoluminescence with colored bars 0, 1, $1'$, and 2 representing the spectral filters that were used to select each transition. These filter bands correspond to integrating across the ZPL and acoustic phonon modes, the TO(M)/LO(K) mode, the LO(Γ) and LO(T) modes, and the above described two-phonon modes, respectively. The filtered two-photon autocorrelations $g^{(2)}_{ll}(\tau)$ in Fig. 5.2(b)-(e) for the $l = 0$, 1, $1'$, and 2 spectral bands confirm that antibunching is present in every phonon replica in addition to the ZPL, even without background correction.

Mean fits and 95% credibility intervals from a self-consistent Bayesian regression for a two-level model of $g^{(2)}_{ll}(\tau)$ are plotted in red and black respectively. The autocorrelations involving the ZPL, TO(M)/LO(K), and LO(T) modes exhibit $g^{(2)}_{ll}(0) < 0.5$, clearly demonstrating single-photon emission. The two-phonon replicas reveal $g^{(2)}_{ll}(0) = 0.55 \pm 0.06$, demonstrating that the band centered at 1.87 eV likely includes two transitions. The time constants for all of the autocorrelations in Fig. 5.2 are $\tau \approx 4$ ns, indicating that details of the phonon-defect coupling are not critical to the dynamics of the phonon replicas themselves.

The frequency-filtered two-photon correlation function $g^{(2)}_{lm}(\tau)$ is a normalized measure

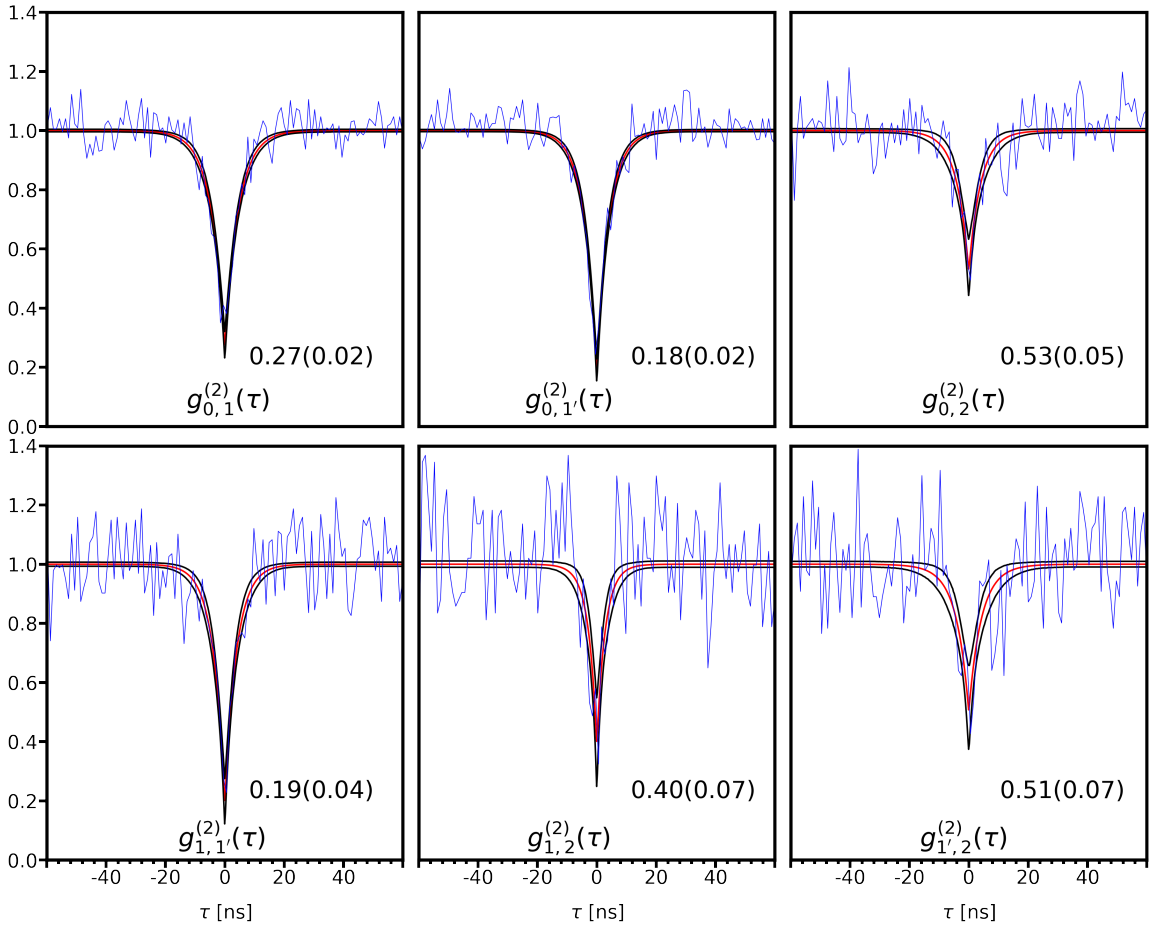

Figure 4.3: Frequency-filtered two-photon cross-correlations $g^{(2)}_{lm}(\tau)$ between each pair of spectral bands visible at room temperature, labeled in terms of the four spectral bands illustrated in Fig. 2(a).The mean and standard deviation for $g^{(2)}_{lm}(0)$ are inset in each panel

of photon fluctuations that quantifies the correlation between a photon of color l detected at time τ after a photon of color m is detected. While Fig. 5.2(b)-(e) reported autocorrelations using the same bandpass filter on both detectors, Fig. 4.3 uses different bandpass filters on each detector to measure the cross-correlations between all combinations of the four transitions. The same self-consistent Bayesian regression used to fit the autocorrelation functions in Fig. 5.2(b)-(e) is used in Fig. 4.3.

The Cauchy-Schwarz inequality: $[g^{(2)}_{l,m}(\tau)]^2 \leq g^{(2)}_{l,l}(\tau)g^{(2)}_{m,m}(\tau)$ describes the classical limit for two mode fields. While photon anticorrelations lead to the antibunching reported in Fig. 5.2, Cauchy-Schwarz inequality violations emerge from positive quantum correlations

between two fields [177, 164, 178]. The Franck-Condon model of a single defect coupled to several phonon modes would lead one to expect anticorrelations between each measured frequency band, with no Cauchy-Schwarz inequality violation. Cascaded photoemission would yield a violation, as would the presence of uncorrelated single photon emitters within one of the spectral bands illustrated in Fig. 5.2(a). All of the measured cross-correlations reported in Fig. 4.3 satisfy the Cauchy-Schwarz inequality except for $g^{(2)}_{0,2}$ and $g^{(2)}_{1',2}$. Combining this observation with the reduced antibunching seen in the two-phonon replicas in Fig. 5.2 and the phonon density of states calculations in Fig. 5.1 provides significant support for the claim that the narrow linewidth feature seen at 1.86 eV in the low-temperature PL spectrum in Fig. 5.1(a) is an uncorrelated SPE. Note that no Cauchy-Schwarz violation is seen for $g^{(2)}_{1,2}$ because of the reduced antibunching of $g^{(2)}_{1,1}$ compared with $g^{(2)}_{0,0}$ and $g^{(2)}_{1',1'}$.

4.4 Conclusions

Distinguishing between low-brightness SPEs and phonon replicas is important for the further development of 2D materials for quantum technologies, but the critical issue here is the otherwise strong anticorrelations between antibunched spectral bands. Because of the measured anticorrelations in Figs. 5.2 and 4.3, and because the measured PL spectrum can be completely described in terms of a ZPL and one and two phonon replicas, the state of the photoluminescence can be represented as $\alpha_1 \left|\psi_{\omega_{ZPL}}\right\rangle + \sum_i \alpha_i \left|\psi_{\omega_{PR_i}}\right\rangle \left|\psi_{\omega_{PH_i}}\right\rangle + \sum_{j,k} \alpha_{j,k} \left|\psi_{\omega_{PR_{j,k}}}\right\rangle \left|\psi_{\omega_{PH_j}}\right\rangle \left|\psi_{\omega_{PH_k}}\right\rangle$, where each term describes a Fock state of zero or one photons or phonons. The first term describes photons emitted into the ZPL (ω_{ZPL}), the second describes single phonon replicas (ω_{PR_i}) and single mid-infrared phonons (ω_{PH_i}), and the final term describes the two-phonon replica ($\omega_{PR_{j,k}}$) and the associated phonon pair($\omega_{PH_j}, \omega_{PH_k}$). Increased control over vibronic pathways will be critical to the generation of high fidelity photon-phonon entanglement, which may be enabled by appropriate phononic cavity design. The anticorrelations measured here thus provide a clear path toward heralded single phonon sources and phonon-photon entanglement in 2D materials.

The characterization of photonic correlations between all electronic and vibronic transitions associated with a given defect is critical to the understanding of quantum phononic dynamics. Further control of the phonon density of states is needed to generate controllable quantum vibronic states, but the measurements reported here have importance both for quantum information science and phononic technologies more generally. In particular, these results point toward one approach for developing quantum photonics and quantum phononics in the mid-infrared atmospheric transparency windows. Recent demonstrations of satellite-to-ground quantum key distribution, for example, have relied on weak coherent pulses and entangled single photon sources at near-infrared wavelengths [179, 180]. These demonstrations have suffered from 20-30 dB attenuation because of atmospheric absorption and scattering. Developing bright single photon sources and entangled photon sources at mid-infrared wavelengths would enable significant improvements in satellite-to-ground quantum communications.

Moreover, strong cross-correlations between the zero-phonon mode and the phonon replicas and strong positive correlations between each phonon replica and the associated mid-infrared phonon may enable side-channel attacks against quantum communication protocols. Similarly, detection of mid-infrared phonons could enable quantum non-demolition measurements on the state of visible phonon replicas. Because electron-phonon coupling in hBN is strain-dependent, the strength of these effects can be controlled with nanopatterned surfaces.

Finally, hexagonal boron nitride has drawn significant interest because of its hyperbolic phononic dispersion [181]. Hyperbolic dispersion enables super-resolution imaging and significant Purcell effects for shallow defects. Combining the single and entangled phonon sources described here with control over the hyperbolic dispersion of nanopatterned multilayer hBN could therefore enable significant advances in the concept of cavity quantum phonodynamics [182]. While the results presented here have illustrated the first evidence of quantum phononics in hBN, it remains crucial to more carefully explore the combined

phononic, photonic, and electronic dynamics of color centers in 2D materials in order to advance science and technology in all of these research agendas.

4.4.1 Acknowledgments

The authors acknowledge feedback from Raphael Pooser. This research was sponsored by the Laboratory-Directed Research and Development Program of Oak Ridge National Laboratory, managed by UT-Battelle, LLC for the U.S. Department of Energy. M.F. gratefully acknowledges support by the Department of Defense (DoD) through the National Defense Science & Engineering Graduate Fellowship (NDSEG) Program. L.L. acknowledges support from the U. S. Department of Energy, Office of Science, Basic Energy Sciences, Materials Sciences and Engineering Division. Rapid thermal processing and spectroscopy experiments were carried out at the Center for Nanophase Materials Sciences (CNMS), which is sponsored at ORNL by the Scientific User Facilities Division, Office of Basic Energy Sciences, U.S. Department of Energy.

4.5 Supplemental Material

4.5.1 Additional Defect Measurements

PL spectra for 5 other defect sites are shown in Fig. 4.4. Each spectrum exhibits a ZPL and one-phonon replicas comparable to those discussed in the manuscript, but the magnitude of the two-phonon replica varied significantly between defects as seen in the middle and right of Fig. 4.4. Additional spectral content to the blue of the ZPL appears in some defect spectra as well. Representative antibunched autocorrelations and anticorrelated cross-correlations, without background correction, are provided in Fig. 4.5 and Fig. 4.6 substantiating the reproducibility of this study.

The phonon-replica detuning exhibited no significant change with temperature as seen in Fig. 4.4 and Fig. 4.7. Shifts in wavelength $\Delta\lambda$ and energy ΔE were calculated as

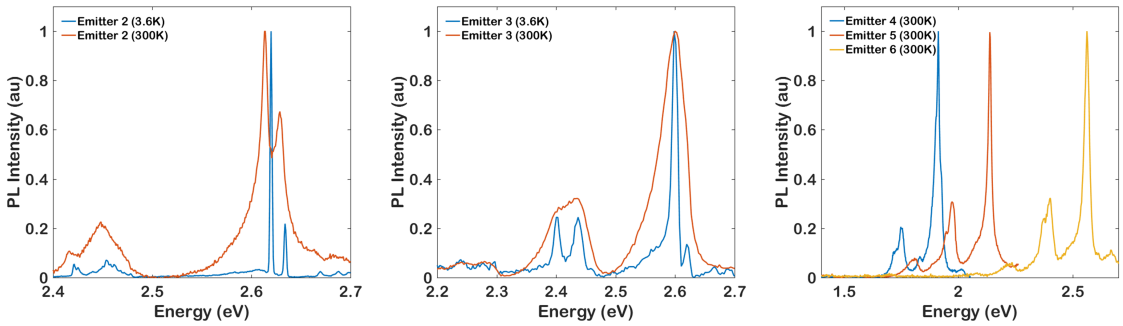

Figure 4.4: (left, middle) Representative spectra of two additional defects recorded at 300K and 3.6K and (right) additional spectra for three other defects that were recorded only at room temperature.

$$\Delta\lambda = \lambda_{ZPL}(T_L) - \lambda_{ph}(T_L) - (\lambda_{ZPL}(T_H) - \lambda_{ph}(T_H)), \tag{4.4}$$

$$\Delta E = E_{ZPL}(T_L) - E_{ph}(T_L) - (E_{ZPL}(T_H) - E_{ph}(T_H)), \tag{4.5}$$

where λ_{ZPL} (E_{ZPL}) is the wavelength (energy) of the ZPL, λ_{ph} (E_{ph}) is the wavelength (energy) of the peak vibronic spectral mode, and $T_L = 4K$ and $T_H = 300K$ are the temperatures that the spectra were collected at for SPE1-SPE3. The uncertainty in the calculated shift in wavelength (0.4 nm) was greater then the spectrometer resolution (0.2 nm). In contrast, the 8 meV redshift of the mode near 1.86eV in Fig. 2 of the Rapid Communication is consistent with the measured redshifts shown in Fig. 4.8 for different emitters characterized at low temperature and room temperature. This further corroborates the claims in the Rapid Communication that that mode is a combination of a 2-phonon replica and a separate, uncorrelated ZPL.

The claim that we have observed and modeled the vibronic modes of a single defect is further evidenced by the 1- and 2-phonon peak energies calculated as

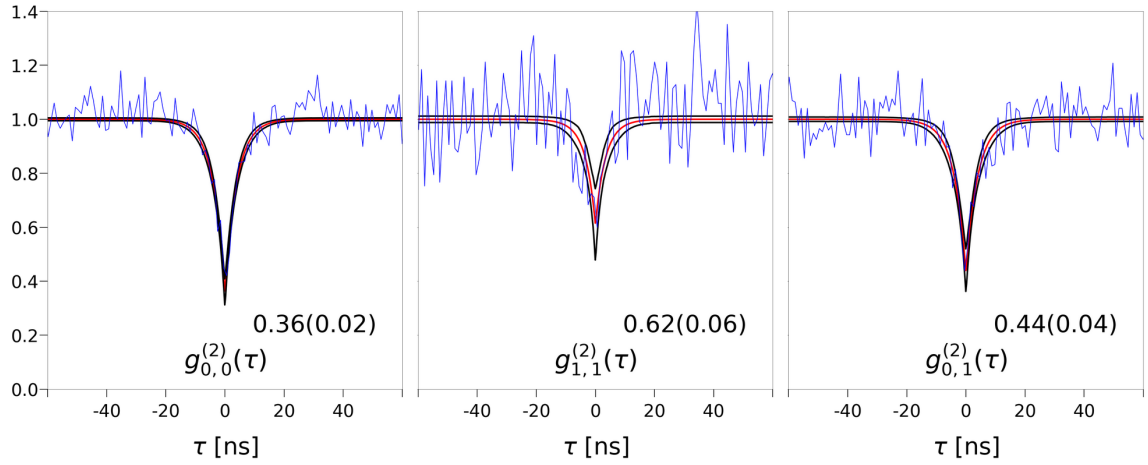

Figure 4.5: Antibunched autocorrelations of single photon emitters for (left) the zero phonon mode (middle) the one-phonon mode and (right) antibunched cross-correlations between the zero- and one-phonon modes for emitter 4 in Fig S1.

$$\Delta E = E_{ZPL} - E_{ph}, \tag{4.6}$$

The 1-phonon (1-ph, and 1′-ph, and 2-phonon (2-ph) peak energies are plotted in Fig. 4.9(a-b) for low temperature measurements. As seen in Fig. 4.9(a-b), SPE1-SPE3 exhibit peak 1-phonon energies consistent with one another whereas SPE1 and SPE3 exhibit 2-phonon peak energies consistent with one another. This consistency is further evidenced for SPE1-SPE6 in Fig. 4.9(c-d) for measurements performed at 300K.

4.5.2 Background Correction

For each defect spectrum, a background spectrum was collected $\sim 1\ \mu m$ from the defect position. The exact position where the background spectrum was collected was determined by the minimum distance needed to minimize collection of PL from the defect. The background data was then scaled by a scalar constant and subtracted from the signal spectrum in order to maximize the goodness-of-fit to our model. An example of these spectra are provided in Fig. 4.10.

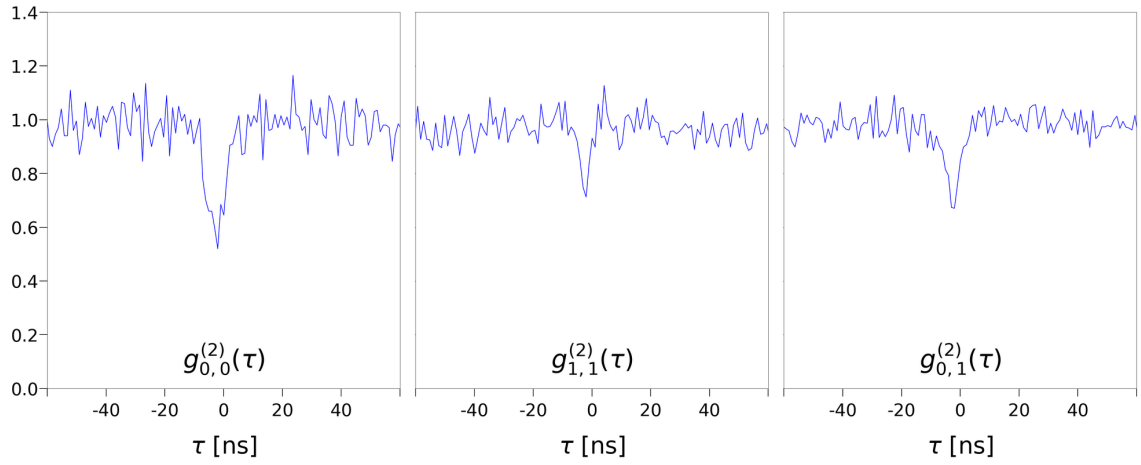

Figure 4.6: Antibunched autocorrelations of single photon emitters for (left) the zero phonon mode (middle) the one-phonon mode and (right) antibunched cross-correlations between the zero- and one-phonon modes for emitter 2 in Fig S1.

4.5.3 Correlations in PL bursts

No blinking was observed in the defects studied. However correlated fluorescent dynamics were observed over timescales of $\sim 10s$ in the ZPL and the phonon replica as shown in Fig. 4.11.

4.5.4 Methods and Experimental Apparatus

Multilayer hBN flakes (3-5 layers in thickness) from Graphene Supermarket were annealed in a First Nano rapid thermal processor at a temperature of 850°C in 1 Torr N_2. The temperature was increased and decreased at 5°C/min.

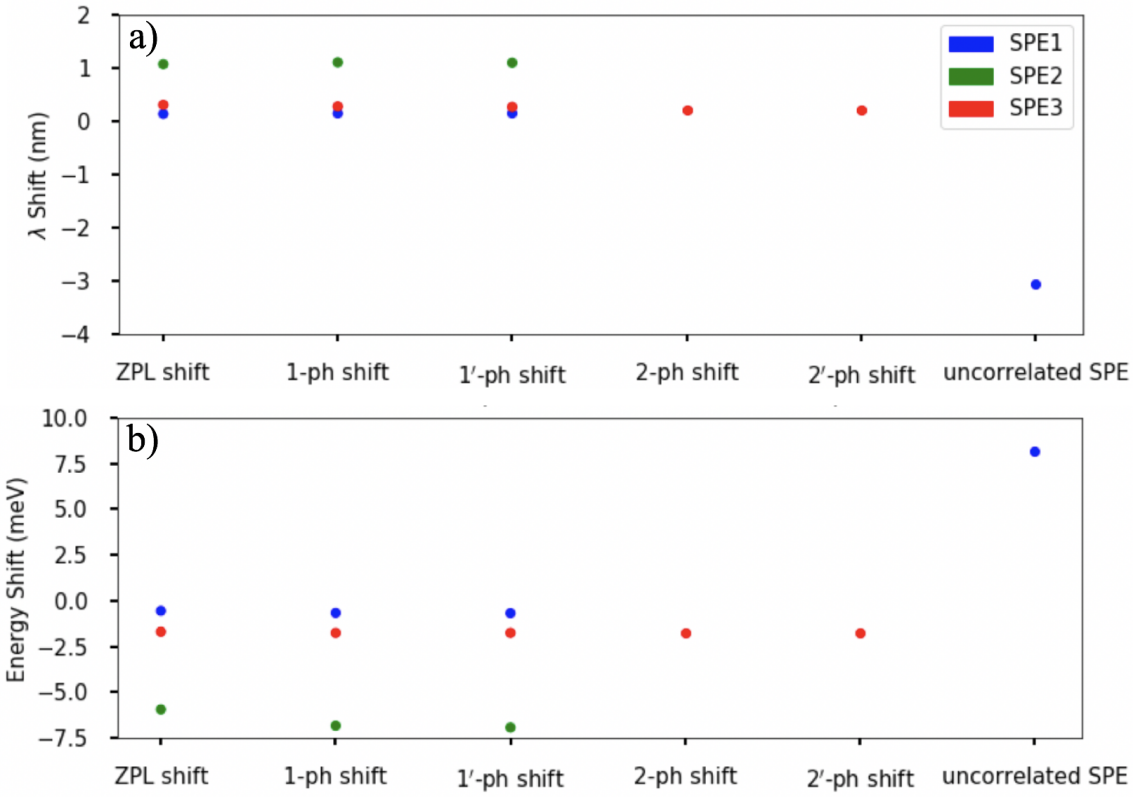

Figure 4.7: Experimental wavelength (a) and energy (b) shifts for the ZPL, 1- and 2-phonon sidebands for SPE1-SPE3.

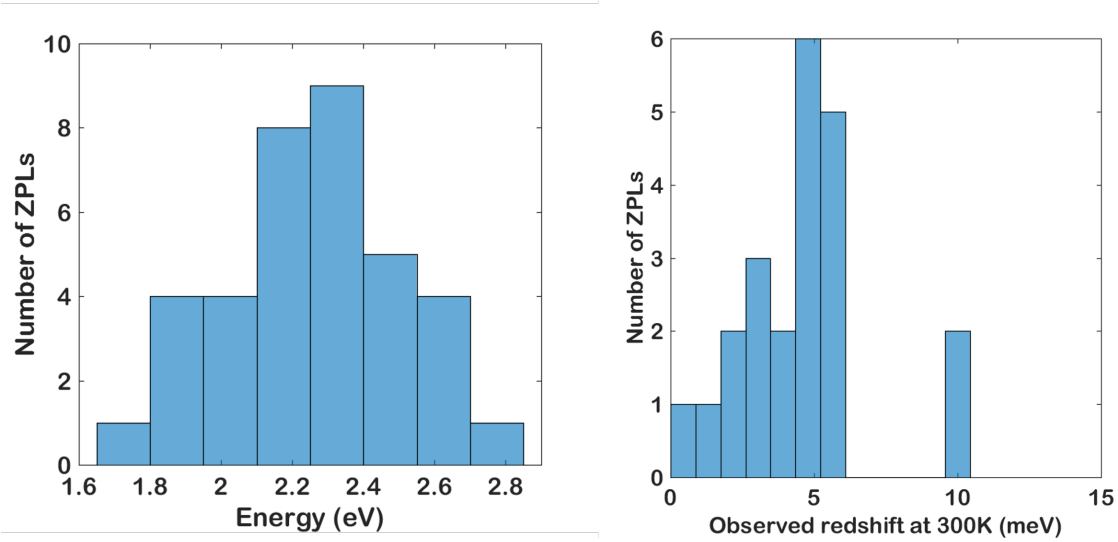

Figure 4.8: (left) Histogram of measured ZPL energies for 36 defect spectra recorded at room temperature. (right) Histogram of the measured ZPL redshift with increasing temperature recorded for the subset of 14 defect spectra characterized at room temperature and 3.6K.

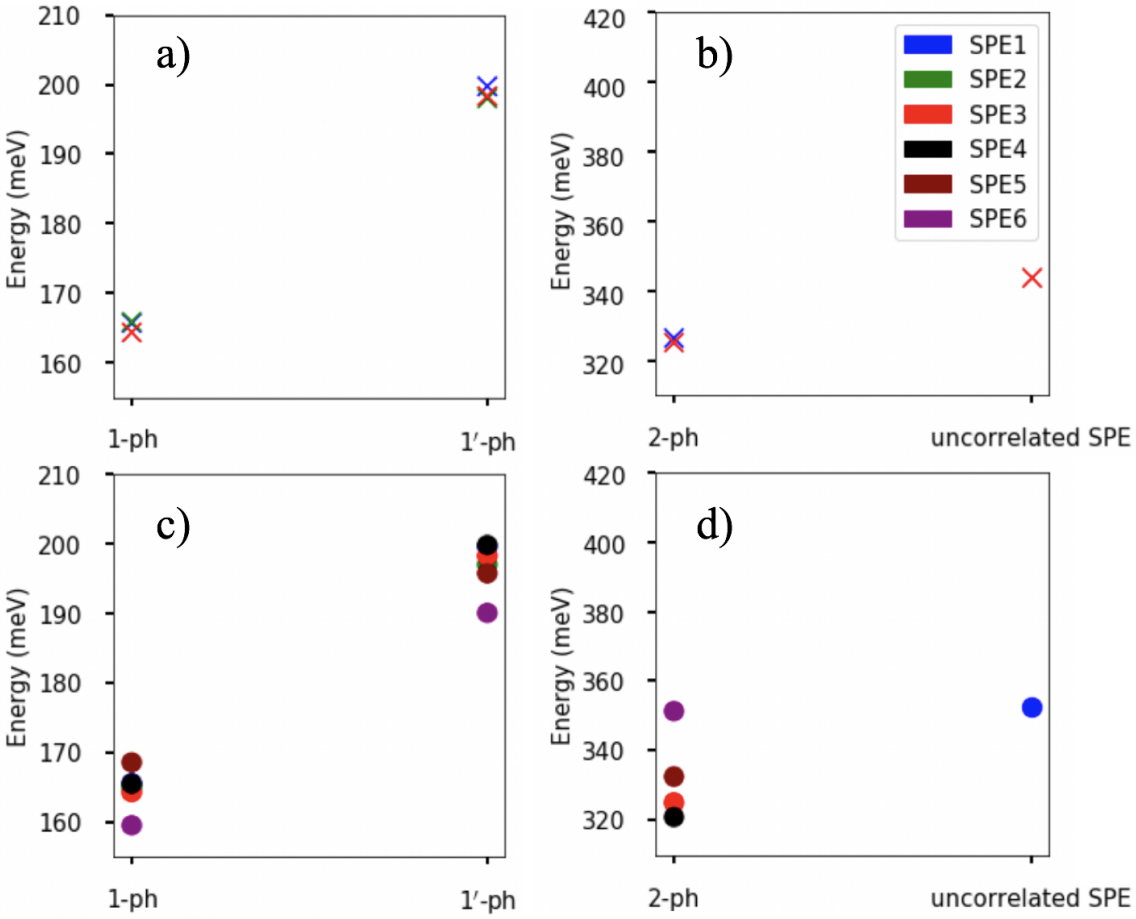

Figure 4.9: The theoretical 1- (1-ph, 1′-ph) and 2-phonon (2-ph) peak energies at 4K (a-b) and 300K (c-d). The peak energies are calculated by subtracting the observed peak vibronic spectral modes from the ZPL energy for each SPE.

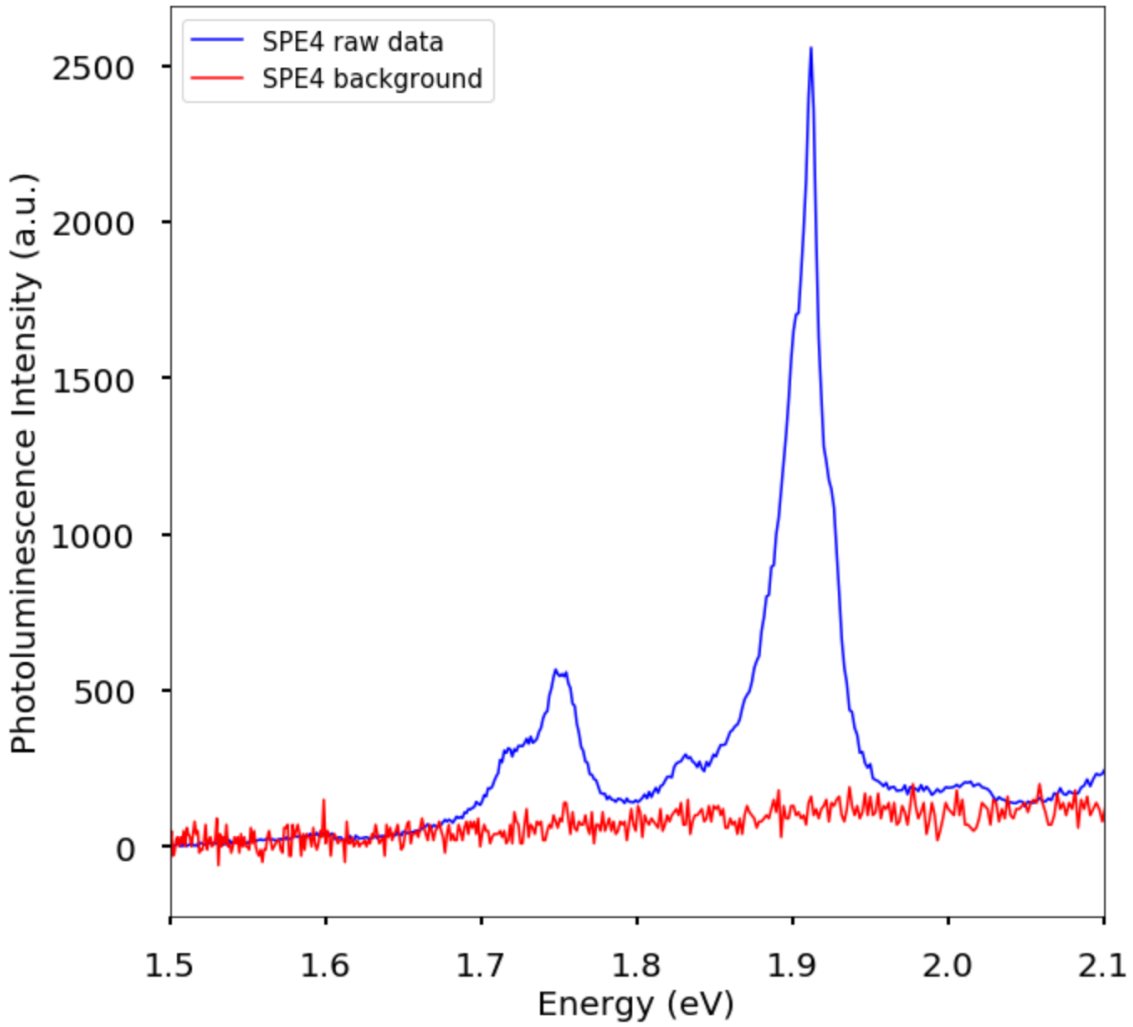

Figure 4.10: SPE4 background (red) and raw (blue) data. The background spectrum is magnified by 10x.

For the μPL and colored HBT interferometry, a 100x (NA=0.9) objective was used to collect PL under $40\mu W$ of continuous-wave 405nm laser excitation. The colored HBT interferometer was fiber coupled to a 105 μm core multimode fiber splitter. The outputs of the splitter were passed to filters in free space. The filters were rotated with respect to the optical path of the PL to tune to the center wavelength of interest. Four filters from Semrock were used (TBP01-487-15,TBP01-547-15,TBP01-617-14,TBP01-697-13) giving a tunable range of 435-710nm with a corresponding maximum bandwidth of 20nm. The PL was then recollected by another 105 μm core multimode fiber, detected by Perkin-

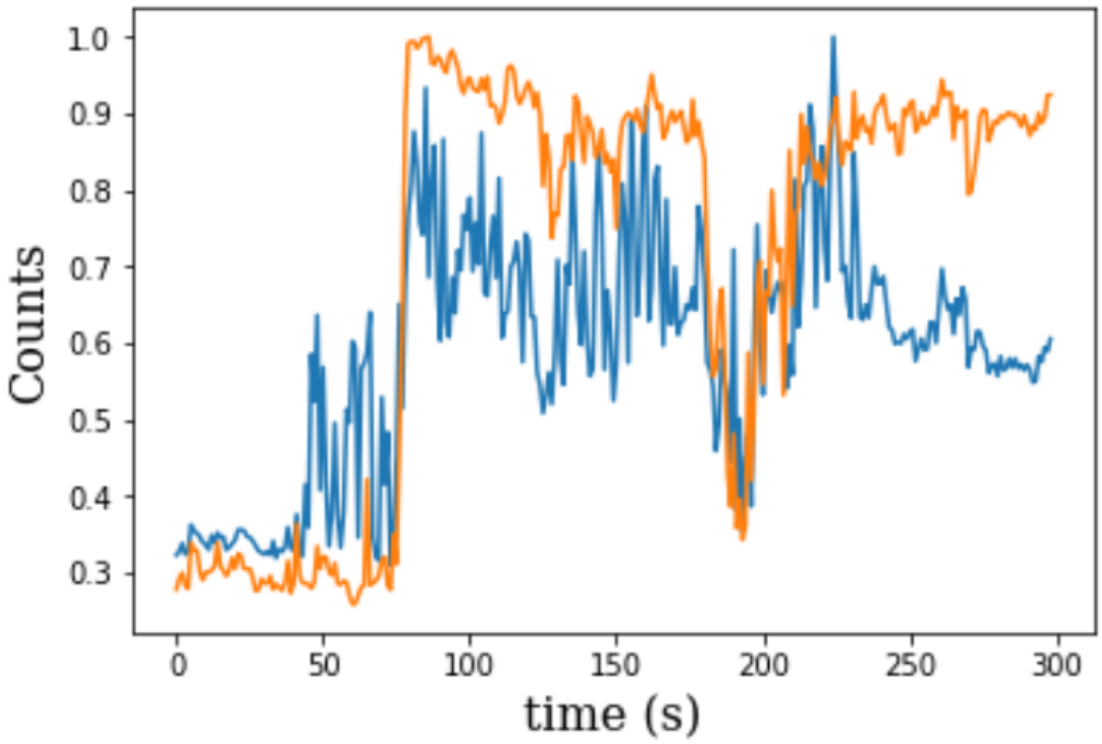

Figure 4.11: Time trace data for the ZPL (orange) and one-phonon replica (blue) for SPE4.

Elmer single photon counting modules (SPCM-AQR), and recorded by a Hydraharp 400 time tagging circuit.

4.5.5 Emission Spectrum Calculation

The derivation of the emission cross-section detailed below is a compilation of results from references [175, 176, 107, 148]. The optical emission of point defects is significantly modified by its interaction with the lattice. The electron-lattice interaction contributes a perturbative potential energy to the lattice nuclei of the defect which is dependent on the defect's electronic state. The total Hamiltonian of a point defect coupled to the vibrational modes of the lattice when the defect is in the ground state is given by

$$H_{\tilde{f}} = E_G + H_O + H_n, \tag{4.7}$$

where E_G is the energy of the electron corresponding to its ground state and when the lattice is in an undistorted configuration, H_O is the Hamiltonian for an ideal lattice, and H_n is the electron-lattice interaction. With this in mind, the emission transition rate $w_{\widetilde{i}\to\widetilde{f}}(\omega)$ for a defect coupled to the vibrational modes of its host lattice is given as

$$w_{\widetilde{i}\to\widetilde{f}}(\omega) = \frac{2\pi}{\hbar^2}|\langle\widetilde{f}|\mu|\widetilde{i}\rangle|^2\delta(\omega_{\widetilde{f}\widetilde{i}}-\omega), \tag{4.8}$$

where μ is the electric dipole moment operator, and $|\widetilde{i}\rangle = |E,m\rangle$ and $|\widetilde{f}\rangle = |G,n\rangle$ are the initial and final vibronic states respectively. The emission cross-section $\sigma(\omega)$ for a defect coupled to the vibrational modes of its host lattice may be written as,

$$\sigma(\omega) = \frac{16\pi^2 c}{\hbar\omega}|\langle\widetilde{f}|\mu|\widetilde{i}\rangle|^2\delta(\omega_{\widetilde{f}\widetilde{i}}-\omega), \tag{4.9}$$

for a photon flux $\frac{I(\omega)}{\hbar\omega} = \frac{A^2\omega}{8\pi\hbar c}$, where A is a the amplitude of the exciting light's vector potential [176]. This dirac-delta may be rewritten in its integral form giving,

$$\sigma(\omega) = \frac{8\pi c}{\hbar\omega}\int dt e^{i(\omega_{\widetilde{f}\widetilde{i}}-\omega)t}|\langle\widetilde{f}|\mu|\widetilde{i}\rangle|^2, \tag{4.10}$$

$$= \frac{8\pi c}{\hbar\omega}\int dt e^{i(\omega_{\widetilde{f}\widetilde{i}}-\omega)t}\langle\widetilde{i}|\mu|\widetilde{f}\rangle\langle\widetilde{f}|\mu|\widetilde{i}\rangle, \tag{4.11}$$

$$= \frac{8\pi c}{\hbar\omega}\int dt e^{i(\omega_{\widetilde{f}}-\omega_{\widetilde{i}}-\omega)t}\langle\widetilde{i}|\mu|\widetilde{f}\rangle\langle\widetilde{f}|\mu|\widetilde{i}\rangle, \tag{4.12}$$

$$= \frac{8\pi c}{\hbar\omega}\int dt e^{-i\omega t}\langle\widetilde{i}|\mu|\widetilde{f}\rangle\langle\widetilde{f}|e^{i\omega_{\widetilde{f}}t}\mu e^{-i\omega_{\widetilde{i}}t)}|\widetilde{i}\rangle, \tag{4.13}$$

$$= \frac{8\pi c}{\hbar\omega}\int dt e^{-i\omega t}\langle\widetilde{i}|\mu|\widetilde{f}\rangle\langle\widetilde{f}|e^{iH_{\widetilde{f}}t/\hbar}\mu e^{iH_{\widetilde{i}}t/\hbar}|\widetilde{i}\rangle, \tag{4.14}$$

$$= \frac{8\pi c}{\hbar\omega}\int dt e^{-i\omega t}\langle\widetilde{i}|\mu(0)|\widetilde{f}\rangle\langle\widetilde{f}|\mu(t)|\widetilde{i}\rangle, \tag{4.15}$$

$$\mu(t) = e^{(iH_{\widetilde{f}}t/\hbar)}\mu e^{(-iH_{\widetilde{i}}t/\hbar)}. \tag{4.16}$$

According to the Born-Oppenheimer approximation we may write the vibronic states as

$$\widetilde{|i\rangle} = |E\rangle|m\rangle = \psi_E(q;Q)\chi_m(Q), \tag{4.17}$$

$$\widetilde{|f\rangle} = |G\rangle|n\rangle = \psi_G(q;Q)\chi_n(Q), \tag{4.18}$$

where Q is the normal coordinates of the lattice, and q is the coordinates relative to the dipole operator μ. Under this adiabatic approximation $\sigma(\omega)$ may be written as

$$\sigma(\omega) = \frac{8\pi c}{\hbar\omega}\int_{-\infty}^{\infty} dt e^{-i\omega t}\langle E|\langle m|\mu(0)|n\rangle|G\rangle\langle G|\langle n|\mu(t)|m\rangle|E\rangle. \tag{4.19}$$

According to the Frank-Condon prinicple [175, 176] the electronic transitions are immediate relative to phononic transitions and $\langle E|\mu|G\rangle$ is independent of Q,

$$\sigma(\omega) = \frac{8\pi c}{\hbar\omega}|\langle E|\mu|G\rangle|^2\int_{-\infty}^{\infty} dt e^{-i\omega t}\langle m|n\rangle\langle n|e^{i(H_{\widetilde{f}}-H_{\widetilde{i}})t/\hbar}|m\rangle. \tag{4.20}$$

However due to our ignorance of the initial state under thermal equilibrium we must take an average across all initial states $|m\rangle$ of the canonical ensemble and similarly sum across all final states $|n\rangle$

$$\sigma(\omega) = \frac{8\pi c}{\hbar\omega}|\mu|^2\sum_{n,m}\omega_m\int_{-\infty}^{\infty} dt e^{-i\omega t}\langle m|n\rangle\langle n|e^{i(H_{\widetilde{f}}-H_{\widetilde{i}})t/\hbar}|m\rangle, \tag{4.21}$$

$$= \frac{8\pi c}{\hbar\omega}|\mu|^2\sum_{m}\omega_m\int_{-\infty}^{\infty} dt e^{-i\omega t}\langle m|e^{i(H_{\widetilde{f}}-H_{\widetilde{i}})t/\hbar}|m\rangle, \tag{4.22}$$

$$= \frac{8\pi c}{\hbar\omega}|\mu|^2\int_{-\infty}^{\infty} dt e^{-i\omega t}\langle\langle m|e^{i(H_{\widetilde{f}}-H_{\widetilde{i}})t/\hbar}|m\rangle\rangle_m, \tag{4.23}$$

where $\langle ... \rangle_m$ is an average across all initial states $|m\rangle$ of the canonical ensemble. We can reformulate $\sigma(\omega)$ in terms of Fourier transforms:

$$\sigma(\omega) = \frac{16\pi^2 c}{\hbar\omega}|\mu|^2 G(\omega), \tag{4.24}$$

$$= \frac{16\pi^2 c}{\hbar\omega}|\mu|^2 G(\omega), \tag{4.25}$$

$$G(\omega) = \frac{1}{2\pi}\int_{-\infty}^{\infty} dt e^{-i\omega t} g(t), \tag{4.26}$$

$$g(t) = \int_{-\infty}^{\infty} d\omega e^{i\omega t} G(\omega). \tag{4.27}$$

When H_n is linear in the displacement of normal modes[176] (i.e. the harmonic approximation is assumed) then

$$g(t) = e^{i\omega_{GE}} e^{-S} e^{S\zeta(t)}, \tag{4.28}$$

$$\zeta(t) = \frac{S_0}{S}\int_{-\infty}^{\infty} d\Omega'(\rho(\Omega')/\Omega'^2)\eta(\Omega'), \tag{4.29}$$

where Ω' is the phonon energy, $\rho(\Omega')$ is the total phonon density of states, S_0 and S are the dimensionless Huang-Rhys parameters corresponding to the fundamental and higher order normal modes of the lattice.

$$\eta(\Omega', t) = \begin{cases} e^{i\Omega' t}(n(\Omega')+1) & \Omega' \geq 0, \\ e^{-i\Omega' t} n(\Omega') & \Omega' \leq 0, \end{cases} \tag{4.30}$$

and $n(\Omega') = 1/(e^{\hbar\Omega'/kT} - 1)$ is the thermal phonon occupation number. For emission spectra at low temperatures it is improbable that a phonon is annihilated and hence only the $\eta(\Omega')$ for $\Omega' \geq 0$ contributes to the emission spectrum and for $\Omega' \leq 0$ only the zero phonon mode term contributes to the emission spectrum. Hence,

$$G(\omega) = (e^{-S}/2\pi)\int_{-\infty}^{\infty} dt e^{i(\omega_{GE}-\omega)} e^{S\zeta(t)}, \tag{4.31}$$

$$G(\omega) = (e^{-S}/2\pi)\sum_{p=0}^{\infty}\frac{S^p}{p!}\Gamma_p(\omega), \tag{4.32}$$

$$\Gamma_p(\omega) = \int_{-\infty}^{\infty} dt e^{i(\omega_{GE}-\omega)t}[\zeta(t)]^p, \tag{4.33}$$

and for the first phonon replica we have:

$$\Gamma_1(\omega) = \frac{1}{2\pi}\int_{-\infty}^{\infty} dt e^{i(\omega_{GE}-\omega)t}\zeta(t). \tag{4.34}$$

Under the approximation that phonons are only created in emission spectra at low temperatures, we have

$$\Gamma_1(\omega) = \frac{S_0}{2\pi S}\int_0^{\infty} d\Omega'(\rho(\Omega')/\Omega'^2)(n(\Omega')+1)\times \tag{4.35}$$

$$\int_{-\infty}^{\infty} dt e^{i(\omega_{GE}+\Omega'-\omega)t}, \tag{4.36}$$

$$= \frac{S_0}{S}\int_0^{\infty} d\Omega'(\rho(\Omega')/\Omega'^2)(n(\Omega')+1)\delta(\omega_{GE}+\Omega'-\omega), \tag{4.37}$$

$$= \frac{S_0}{S}\rho(\Omega)(n(\Omega)+1)/\Omega^2, \tag{4.38}$$

where the phonon energy, $\Omega = \omega - \omega_{GE}$.

We may rewrite Γ_p as a convolution integral since $F^{-1}[F[f]F[g]] = f \circledast g$ [176],

$$\Gamma_p(\omega) = \int_0^{\infty} d\Omega\Gamma_{p-1}(\Omega)\Gamma_1(\omega+\omega_{GE}-\Omega). \tag{4.39}$$

The above derivation does not take into account the effects of quadratic electron-phonon coupling or inhomogeneous broadening. To account for inhomogeneous broadening in the

zero phonon line (ZPL), the experimentally observed ZPL is modeled as a Lorentzian Γ_o with finite linewidth 1.1 meV and convolved with a phenomenological term $\Gamma_{inhomo}(\omega)$ accounting for the inhomogeneous broadening of the ZPL which contributes to its asymmetry at low temperatures,

$$\Gamma_{o,inhomo} = \Gamma_o \circledast \Gamma_{inhomo}, \tag{4.40}$$

where $\Gamma_{inhomo}(\omega) = 1/(B + (\Omega - \Omega_o))^2$ where B = 110 meV is the full-width at half-max and Ω_o = 7 meV is the center phonon frequency [174]. We attribute this inhomogeneous broadening to a deformation potential interaction between longitudinal acoustic phonons as discussed in [148]. Phonon-mediated broadening of the zero phonon mode is resolved phenomenologically by convolving the zero phonon line (ZPL) $\Gamma_0(\omega)$ with the lineshape $G(\omega)$. All calculations were performed as follows:

$$G(\omega) = \frac{e^{-S}}{2\pi}\Gamma_{o,inhomo} + \frac{e^{-S}}{2\pi}\sum_{p=1}^{\infty}\frac{S^p}{p!}\Gamma_p(\omega), \tag{4.41}$$

$$\Gamma_p(\omega) = \int d\Omega \Gamma_{p-1}(\Omega)\Gamma_1(\omega + \omega_{GE} - \Omega), \tag{4.42}$$

$$\sigma(\omega) = \frac{16\pi^2 c}{\hbar\omega}|\mu|^2\Gamma_0 \circledast G(\omega). \tag{4.43}$$

Hence we have assumed that only linear terms are dominant and that we are in the weak coupling regime.

Fits of the model to experimental emission spectrum are reported in the main text. to the above model the experimental

4.5.6 Estimation of the total phonon density of states $\rho(\omega)$

At low temperatures, where $\hbar\Omega \gg kT$, the total phonon density of states (DOS) $\rho(\Omega)$ may be estimated as the one-phonon density of states $\rho_1(\Omega)$ because the zero- and one-phonon modes are the most probable modes to be occupied. Because the phonon modes are modeled as quantum harmonic oscillators, the zero-phonon mode contributes a diverging term and hence it is excluded from $\rho(\omega)$. If coupling of delocalized modes to the defect is the dominant contribution to the vibronic spectrum, then there must be some interaction, selection rules, divergent phonon matrix elements, etc. to account for the discrepancy between the experimental emission spectrum and the calculated one-phonon DOS. As discussed in the main text, we measure phonon replicas redshifted from the ZPL by 326 meV (2TO(M)/2LO(K)), 359 meV (LO(Γ) +TO(M)/LO(K)) and 395 meV (2LO(Γ)), all consistent with two phonon excitation. We assume that these sums are the two-phonon modes and that the LO(K), TO(M)/LO(K) and LO(Γ) are the one-phonon modes and consequently $\rho(\Omega)$ should only include these modes. Hence we apply a phenomenological weighting term $w(\omega)$ to the calculated one-phonon DOS to preferentially favor the modes centered at 166 meV, 177 meV, and 200 meV,

$$\rho(\omega) = \rho_1(\omega) w(\omega), \tag{4.44}$$

$$w(\omega) = \sum_{i}^{n=3} \frac{A_i \Gamma_i}{(2\pi)(\Gamma_i/(2\pi))^2 + (\omega - \omega_i)^2}, \tag{4.45}$$

where A_i is a scaling factor, Γ_i is a linewidth and ω_i is the center frequency for the corresponding Lorentzian terms of $w(\omega)$.

$$\omega_i = [165.6, 177.4, 199.3], \tag{4.46}$$

$$\Gamma_i = [6, 2, 1.95], \tag{4.47}$$

$$A_i = [0.017, 0.053, 0.93], \tag{4.48}$$

We find that a fit including the DOS and Lorentzian weighting terms is more informative than fits in which only the Lorentzians weights are included. This is evidenced by comparison of Chi2 tests in which the goodness-of-fit including the DOS was $\chi^2 = 57380$, whereas when it was excluded it was $\chi^2 = 1055399$. This is also made clear qualitatively as seen in Fig. 4.12 where a fit that includes Lorentzian filters but excludes the phonon DOS fails to reproduce the one- and two-phonon sidebands.

Lastly it is important to note that this calculation assumes that localized defect vibrational modes are insignificant. Because this calculation is in part phenomenological, this assumption may not be sound. However this calculation demonstrates that delocalized phonon replicas can plausibly explain the experimental luminescence spectrum.

4.5.7 Bayesian Regression of $g^{(2)}(\tau)$

The second-order coherence function $g^{(2)}_{lm}(\tau)$ is a normalized measure of intensity fluctuations that quantifies the correlation between a photon detected at time $t+\tau$ and a photon detected at time t between two photon streams l and m,

$$g^{(2)}_{lm}(\tau) = \frac{\langle \hat{I}(t)\hat{I}(t+\tau)\rangle}{\langle \hat{I}(t)\rangle^2}. \tag{4.49}$$

Here, $g^{(2)}_{lm}(\tau)$ of the μPL was characterized by a colored Hanbury Brown-Twiss interferometer as shown in the inset of Fig.1 in the main text. The posterior density of the parameters

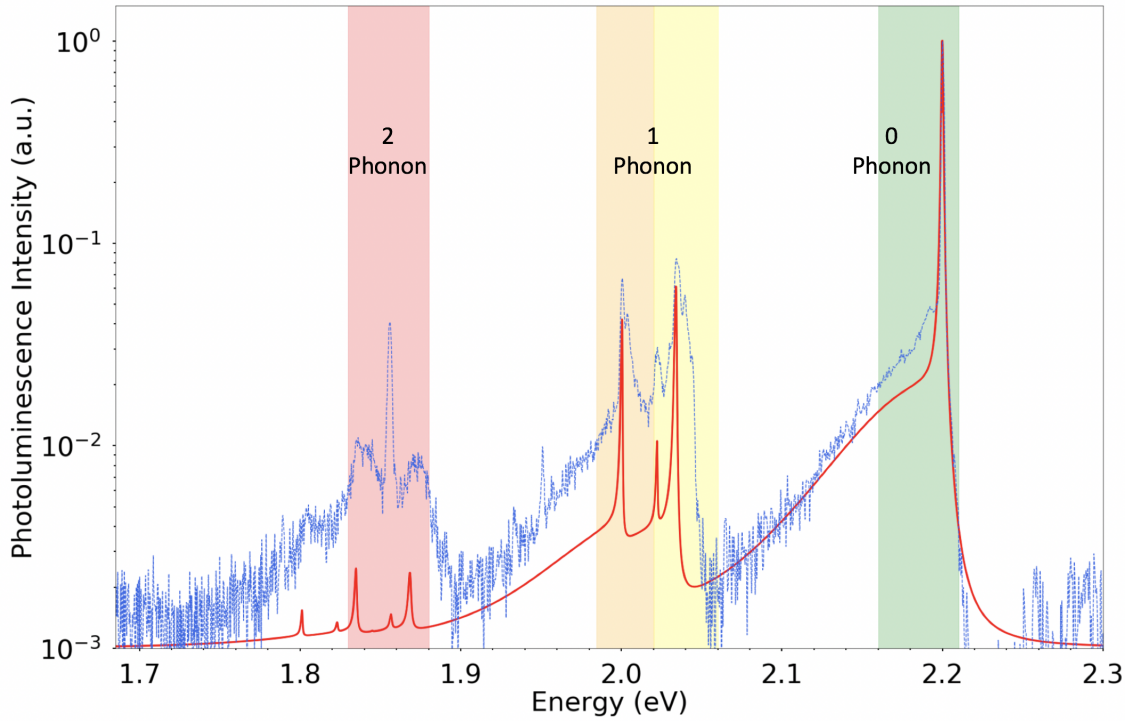

Figure 4.12: Background corrected defect μPL spectrum (blue) collected at 3.6K for direct comparison with the calculated μPL cross-section only using Lorentzian filters (red curve).

θ is given by Bayes' theorem

$$p(\theta|n) \propto p(n|\theta)p(\theta), \tag{4.50}$$

where $n = n_1, \cdots, n_N$ are the measured coincident photon counts, $p(\theta)$ is the prior density assumed to be uniform, and $p(n|\theta)$ is the likelihood taken to be a product of Poisson distributions,

$$p(n|\theta) = \prod_{i=1}^{N} p(n_i|\theta), \tag{4.51}$$

$$p(n_i|\theta) = e^{-C(\tau_i)} \frac{C(\tau_i)^{n_i}}{n_i!}, \tag{4.52}$$

with mean number of coincident photons

$$C(\tau_i) = Ag^{(2)}(\tau_i) \text{ and} \tag{4.53}$$

$$g^{(2)}(\tau_i) = 1 - \frac{1}{n}e^{(\tau_i - \tau_o)/\tau_1} \tag{4.54}$$

where A is the normalization factor in the denominator of equation (1), n is the number of emitters, $\tau_1 = 1/(\Gamma_0 + W_p)$ [107], Γ_0 is the spontaneous emission rate, W_p is the pump rate and τ_o is a zero delay offset.The parameter vector to be estimated is $\theta = \{A, n, \tau_1, \tau_o\}$. While many models assume a single emitter is present and include a background parameter to account for deviations from $g^{(2)}(0) = 0$ we instead model the photon number n explicitly to determine the number of emitters detected. Here n is treated as a continuous random variable. Goodness of fit was determined using a χ^2 test with $\chi^2 \leq 100$ and $p - values \leq 1e - 10$. For auto- and cross-correlations involving the 2-phonon filter band the range of mean photon number $\langle n \rangle$ was 1.7-2.2 clearly indicating that two emitters with differing quantum efficiencies are responsible for such photon statistics.

Chapter 5

Evidence of Photochromism in a Hexagonal Boron Nitride Single Photon Emitter

In this chapter I will address the electronic energy structure of hBN defects. I will extend the technique of two-color HBT to observe cross-correlations between two ZPLs. This and the correlations in the photoluminescence between the two ZPL spectra indicate that these ZPLs orginate from a single defect. This is the first evidence of of Photochromism in a hBN emitter.

Matthew A. Feldman[1,2], Claire Marvinney[2], Alex Puretzky[3], and Benjamin J. Lawrie[2]

[1]Department of Physics and Astronomy, Vanderbilt University, Nashville, TN 37235, USA

[2]Materials Science and Technology Division, Oak Ridge National Laboratory, Oak Ridge TN 37831

[3]Center for Nanophase Materials Sciences, Oak Ridge National Laboratory, Oak Ridge, TN 37831, USA

The following work has been accepted by Optica [183] and is reprinted below in its entirety.

5.1 Abstract

Solid-state single-photon emitters (SPEs) such as the bright, stable, room-temperature defects within hexagonal boron nitride (hBN) are of increasing interest for quantum information science. To date, the atomic and electronic origins of SPEs within hBN are not well understood, and no studies have reported photochromism or explored cross-correlations between hBN SPEs. Here, we combine irradiation-time dependent microphotoluminescence spectroscopy with two-color Hanbury Brown-Twiss interferometry in an investigation of

the electronic structure of hBN defects. We identify evidence of photochromism in a hBN SPE that exhibits single-photon cross-correlations and correlated changes in the intensity of its two zero-phonon lines.

5.2 Introduction

Solid-state single-photon emitters (SPEs) are of increasing interest as a source of non-classical light for quantum computation, quantum communication, and quantum sensing applications [184, 185, 186]. Defects in hexagonal boron nitride (hBN) have emerged as notable SPEs due to their bright, stable, room-temperature emission across the visible spectrum [187]. The recent characterization of spin states in a hBN defect ensemble with optically detected magnetic resonance could enable new quantum memories [188, 189]. Charge state initialization of hBN defects could enable new approaches to coherent optical control [190, 191]. Furthermore, strain localization [192] and strain tuning [193] of hBN SPEs could enable the design of deterministic indistinguishable single photon sources.

Despite these advances in state preparation, readout, and process control, and despite substantial theoretical [194, 118, 195, 125, 120] and microscopic [196] analysis, the atomic origins and electronic structure of hBN SPEs are still poorly understood. To date, defects have been categorized phenomenologically. Initial reports identified group I and group II hBN SPEs based on the difference in their electron-phonon coupling [197]. More recent research demonstrating the existence of four species of hBN emitters spanning the visible spectrum with correlated microphotoluminescence (μPL), cathodoluminescence, and nanoscale strain mapping suggests that the observed defect species may be complexes of defects [196]. Further research has identified photochemical effects such as bleaching of hBN emitters under 405 nm excitation[198], or activation of emitters with electron-beam irradiation [199]. Polarimetric studies of hBN emitters under i) 473 nm and 532 nm excitation and ii) tunable strain have exhibited a misalignment in absorption and emission dipole moments, supporting the claim of a third excited bright state in hBN.[200, 201, 202]. How-

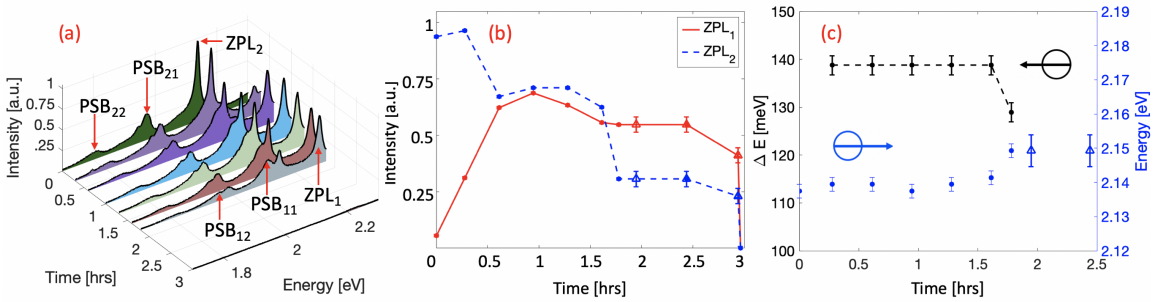

Figure 5.1: Laser irradiation-dependent spectroscopy of a single defect pumped with a 405 nm laser. (a) The μPL spectra of ZPL transitions ZPL_1 and ZPL_2. ZPL_1 has one-phonon (PSB_{11}) and two-phonon (PSB_{12}) sidebands 166 meV and 326 meV, respectively, redshifted from ZPL_1, and ZPL_2 has one-phonon (PSB_{21}) and two-phonon (PSB_{22}) sidebands 166 and 326 meV, respectively, redshifted from ZPL_2. (b) The relative μPL intensity of ZPL_1 and ZPL_2 (normalized to the peak ZPL_1 intensity) show enhancement and partial quenching within the first half hour of irradiation, respectively. For the following hour, they remain stable, after which ZPL_2 undergoes a second partial quenching. ZPL_1 and ZPL_2 remain stable for another hour prior to simultaneously quenching. (c) The energy difference between ZPL_1 and ZPL_2 remains constant until the second partial quenching in ZPL_2 occurs, leading to a 10 meV spectral jump in the energy of ZPL_2. Triangles indicate measurements made using filtered singles counts.

ever, no studies to date have directly reported photochromism in hBN SPEs or explored cross-correlations between electronic transitions in hBN μPL spectra.

Here, we use μPL spectroscopy to study the photostability of defects in few-layer hBN flakes in air when optically pumped with greater photon energy than the activation energy for the photochemical decomposition of hBN[203]. Further, we characterize the cross-correlations between zero-phonon lines (ZPLs) that exhibit correlated changes in intensity with spectrally resolved two-color Hanbury Brown-Twiss (HBT) interferometry. While we have previously used two-color HBT interferometry with photo-stable emitters in hBN under vacuum to verify that the broad emission bands redshifted 166±0.5 meV and 326±0.5 meV from the ZPL are optical one- and two-phonon sidebands (PSBs), respectively [147], the cross-correlated ZPLs studied in this work have separation energies 20 meV below the known optical phonon modes of hBN [204, 205] and localized phonon resonances fail to explain the observed spectrum[125]. Combining irradiation-time depen-

dent μPL spectroscopy with two-color HBT interferometry enables this new investigation of the electronic structure of hBN defects.

5.3 Microphotoluminescence Spectroscopy

We investigate defects in three-to-five layer hBN using the same sample from a previous study[147]. Microphotoluminescence spectroscopic data were collected for each defect using a custom-built room-temperature confocal microscope. Eleven defects with ZPLs ranging from 2.15 to 2.9 eV were observed. The majority of defects measured were identified as group I emitters with ~10 meV linewidth ZPLs and one-phonon doublets and two-phonon sidebands 166 and 326 meV redshifted from the ZPL[197, 147]. Out of these, seven defects photobleached consistent with previous μPL studies of defects in oxygen rich environments[198]. Among the defects that photobleached, two ZPLs within a diffraction-limited confocal volume demonstrated a correlated enhancement and quenching in their μPL intensity under 405 nm excitation. Figure 5.1a shows the μPL spectra measured for that site. ZPL_1 (2.28 eV) has one-phonon (PSB_{11}) and two-phonon (PSB_{12}) sidebands 166±2 meV and 326±2 meV red-shifted with respect to ZPL_1, and ZPL_2 (2.14 eV) has one-phonon (PSB_{21}) and two-phonon (PSB_{22}) sidebands 166±2 and 326±2 meV redshifted from ZPL_2.

We then evaluate the intensity of ZPL_1 and ZPL_2 as a function of irradiation time (see Figure 5.1b) using the ZPL peaks (dots) in our spectra and correlated filtered singles counts (triangles). In the first half-hour of irradiation, the intensity of ZPL_1 and PSB_{11} increases while ZPL_2, PSB_{21} and PSB_{22} decrease as seen in Figure 5.1a-b. The intensities of ZPL_1 and ZPL_2 and their corresponding phonon sidebands then equilibriate for an hour until ZPL_2 is again partially quenched. Prior to this second quench in ZPL_2 the energy difference between ZPL_1 and ZPL_2 was 139±2 meV; afterwards, the energy difference decreases to 129±2 meV due to a 10 meV blue shift in ZPL_2 as seen in Figure 5.1c. The blueshifted ZPL_2 and the ZPL_1 showed no substantial intensity fluctuations before both simultaneously

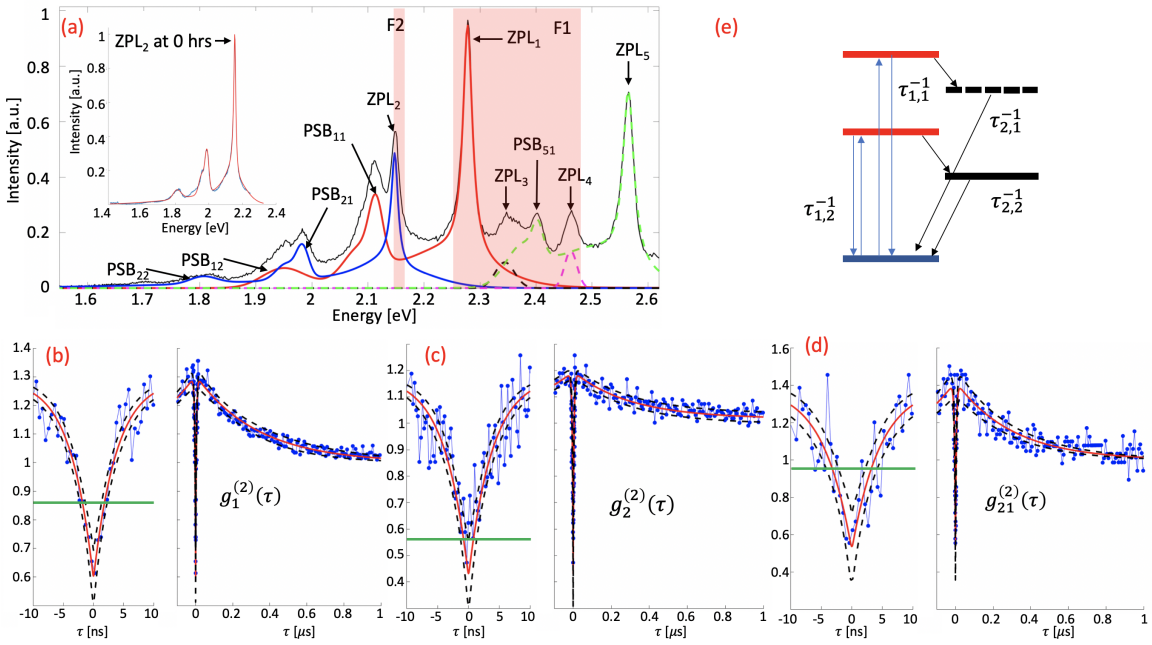

Figure 5.2: Two-color Hanbury Brown-Twiss interferometry after 1.8 hrs of laser-irradiation. (a) Spectral lineshapes for ZPL_j. Fits to the ZPL_1 (red), ZPL_2 (blue) lineshapes and uncorrelated emitters (ZPL_j, $j = 3,4,5$) are used to estimate the probability (z_{ij}) that a transition contributes to the μPL (black) collected in each filtered (F1, F2) interferometer arm ($i = 1,2$). The inset shows the best fit for ZPL_2 at 0 hrs. The auto-correlations for (b) ZPL_1, (c) ZPL_2, and (d) the cross-correlations between ZPL_1 and ZPL_2. The distance of $g_i^{(2)}(0)$ from the limit for single-photon-emission (indicated by the green horizontal line) exceeds five standard deviations, σ. Here the black-dashed lines are the 5σ bounds for $g_i^{(2)}(\tau)$. (e) A proposed energy diagram for the suspected defect with excited states (red) and shelving state(s). The observed shelving in the auto-correlations may be explained by one (solid black) or two (solid and dashed black) energy levels.

quenched as seen in Figure 5.1b and Figure S1 in the Supplemental Material. The ZPLs remained dark after a month, suggesting that they are either bleached or pumped into a very long-lived dark state.

Given the appearance of similar trends in the evolution of the ZPL_1 and ZPL_2 μPL spectra, it may be possible that the two transitions are correlated and are potentially excited-state transitions of the same defect or complex. However, photoluminescence spectroscopy by itself is insufficient to prove such a claim. Clear evidence of photochromism is essential to the understanding of the electronic structure and atomistic origin of hBN single photon emitters.

5.4 Two-Color HBT Interferometry

To test the hypothesis that ZPL_1 and ZPL_2 are excited-state transitions of the same defect, we employed two-color HBT interferometry after ZPL_2 spectrally jumped 10 meV. Filters F1 and F2 (illustrated in Figure 5.2a) selected the luminescence of ZPL_1 and ZPL_2 in each arm of the interferometer. Because of the presence of additional defects in the spectrum shown in Figure 5.2a, the background counts in each channel could not be attributed solely to a Poissonian background. Instead, the background is modeled as defect emission that is uncorrelated with ZPL_1 and ZPL_2 [206]. To determine the contribution of each emitter to the counts in each channel, fits of the lineshapes corresponding to ZPL_1 and ZPL_2 and their respective phonon sidebands were made as shown in Figure 5.2a. Here the lineshapes for ZPL_1 and ZPL_2 were fit using a phenomenological model composed of the sum of a Lorentzian, exponentially modified Gaussian and Gaussian distributions centered at their observed ZPL, low and high phonon-sideband energies, respectively. While this model is agnostic with respect to the origins of the vibrational modes contributing to the PSB emission, it takes into account the observed low and high energy phonon modes as described in the Supplemental Material. The lineshape of the ZPL_2 emission was assumed to be fixed irrespective of spectral jumps and so only the amplitude and peak energy parameters for the ZPL_2 fit were left free for the 1.8 hr irradiation time presented in Figure 5.2a. Additionally, the fit for ZPL_2 at 0 hrs presumes negligible background overlapped with the lineshape of ZPL_2, so only the group 1 emitter phenomenological model was used with no additional background terms. All peaks attributed to uncorrelated background emission were fit using the same lineshape function or with Gaussian distributions.

The probability z_{ij} that the j^{th} lineshape will contribute to the intensity in the i^{th} filtered arm of the HBT interferometer is the overlap integral of the filter transfer function with the total emission of the i^{th} lineshape divided by the total emission in the filter-band [206]. The auto-correlations for ZPL_1 and ZPL_2 as well as the cross-correlation between ZPL_1 and ZPL_2 were calculated with this assumption in mind and using the spectrum taken at

1.8 hrs of laser-irradiation to calculate the probabilities, z_{ij}. The bunching observed in the coincidence counts for $|\tau| > 0$ for both transitions indicates a shelving state is present in each ZPL and we interpret these data assuming a three-level model. The auto-correlations for ZPL_1 and ZPL_2 and the cross-correlations between each are given by

$$g_1^{(2)}(\tau) = (z_{11}^2 + z_{13}^2 + z_{14}^2 + z_{15}^2) g_{\rho 1}^{(2)}(\tau) \tag{5.1}$$
$$+ 2(z_{11}z_{13} + z_{11}z_{15} + z_{11}z_{14} + z_{13}z_{15} + z_{13}z_{14} + z_{15}z_{14}),$$
$$g_2^{(2)}(\tau) = (z_{21}^2 + z_{22}^2) g_{\rho 2}^{(2)}(\tau) + z_{21}z_{22}(g_{21}^{(2)}(\tau) + g_{12}^{(2)}(\tau)), \tag{5.2}$$
$$g_{21}^{(2)}(\tau) = z_{11}z_{22} g_{\rho 21}^{(2)}(\tau) + z_{11}z_{21} g_1^{(2)}(\tau) + z_{13} + z_{14} + z_{15}, \tag{5.3}$$
$$g_{12}^{(2)}(\tau) = z_{11}z_{22} g_{\rho 12}^{(2)}(\tau) + z_{11}z_{21} g_1^{(2)}(\tau) + z_{13} + z_{14} + z_{15}, \tag{5.4}$$
$$g_{\rho i}^{(2)}(\tau) = 1 - \rho_i^2[(1 + a_i)e^{-|x - x_{oi}|\tau/\tau_{1i}} - a_i e^{-|x - x_{oi}|\tau/\tau_{2i}}], \tag{5.5}$$

where $g_1^{(2)}(\tau)$ and $g_2^{(2)}(\tau)$ are the auto-correlation functions for ZPL_1 and ZPL_2, $g_{21}^{(2)}(\tau)$ and $g_{12}^{(2)}(\tau)$ are the cross-correlations between the zero-phonon lines, and $g_{\rho i}^{(2)}(\tau)$ is the three-level model for each correlation function with Poisson-background contribution ρ_i, shelving parameter a_i, excited state lifetime τ_{1i}, and shelving state lifetime τ_{2i}. The fitted parameters for the auto- and cross-correlations are provided in Table 5.3, along with the probabilities z_{ij} in Table 5.2. A full derivation of the auto- and cross-correlations can be found in the Supplemental Material. The threshold for single-photon emission for auto- and cross-correlations is given by $g_{limit,i}^{(2)} = \frac{1}{2}(1 + \rho_i^2 a_i)$[107].

$g_{\rho i}^{(2)}(\tau)$	a	τ_{1i} (ns)	τ_{2i} (ns)
$g_{\rho 1}^{(2)}(\tau)$	0.75	3.9	334
$g_{\rho 2}^{(2)}(\tau)$	0.12	3.2	1600
$g_{\rho 21}^{(2)}(\tau)$	1.0	5.4	271

Table 5.1: Parameter values for the auto- and cross-correlation functions

Due to emission from background emitters, the cross-terms for $g_1^{(2)}(\tau)$, $g_2^{(2)}(\tau)$, $g_{21}^{(2)}(\tau)$ and $g_{12}^{(2)}(\tau)$ degrade the single-photon purity of the emitter while the like-terms dampen the

probability	value
z_{11}	0.55
z_{13}	0.06
z_{14}	0.05
z_{15}	0.34
z_{21}	0.3
z_{22}	0.7

Table 5.2: Probabilities z_{ij} that the j^{th} lineshape will contribute to the counts in the ith filtered interferometer arm

expected shelving amplitude. The most significant background terms come from the overlap of ZPL_1's one-phonon PSB and ZPL_2, where $z_{21} = 30\%$ of the ZPL_1 PSB contributes to the background. But as we will see, the corresponding cross-terms are insufficient to degrade the purity of ZPL_2 beyond the limit for single photon emission. Figures 5.2b-d show the auto- and cross-correlations as well as best-fit and corresponding 5 standard deviation (σ) confidence intervals for $g_1^{(2)}(\tau)$, $g_2^{(2)}(\tau)$ and $g_{21}^{(2)}(\tau)$, respectively. It is clear that the auto- and cross-correlations confirm single-photon emission and provide evidence of photochromism between ZPL_1 and ZPL_2 as the fit for $g_i^{(2)}(0)$ is at least five standard deviations from the limit for single-photon emission. The overlap of ZPL_1 and ZPL_2 leads to additional time dependent cross-terms in (i) the auto-correlation for ZPL_2 ($g_{12}^{(2)}(\tau)$, $g_{21}^{(2)}(\tau)$), and (ii) the cross-correlation between ZPL_1 and ZPL_2 ($g_1^{(2)}(\tau)$), but their contribution to the anti-bunching and anti-correlations are found to be $\sim$10%. Furthermore, all fits for $g_1^{(2)}(\tau)$, $g_2^{(2)}(\tau)$ and $g_{21}^{(2)}(\tau)$ include cross-terms, and thus the background-free cross-correlation between ZPL_1 and ZPL_2 and the respective anti-bunching for each zero-phonon line would increase the distance $[g_{limit,i}^{(2)} - g_i^{(2)}(0)]$.

While the defect photobleached prior to collecting $g_{12}^{(2)}(\tau)$, the large cross-correlation of $g_{21}^{(2)}(\tau)$ and single-photon purity of $g_2^{(2)}(\tau)$ remained consistent with $[g_{limit,i}^{(2)} - g_i^{(2)}(0)] > 5\sigma$ under the assumptions that $g_{\rho 12}^{(2)}(\tau) \approx g_{\rho 2}^{(2)}(\tau)$ while leaving all parameters for $g_{\rho 12}^{(2)}(\tau)$ free in the fits for $g_2^{(2)}(\tau)$. Generally, the auto- and cross-correlations maintain the single-photon purity, whether we assume that the spectral shape of ZPL_2 is the same after its spectral jump

or whether we allow it to be modified. In this case, we left all spectral parameters free to estimate the lineshape for ZPL_2. Under these different cases, the coefficient of determination varied by 1% or less, supporting the claim that these assumptions have negligible effect on the single-photon purity of each ZPL or the magnitude of anti-correlations between ZPL_1 and ZPL_2.

Furthermore, we repeated the two-color HBT interferometry on different sets of additional pairs of ZPLs where each filter only passes light from a single ZPL (i.e. no background emission from other spectrally distinct defects overlaps with the filter linewidth). While these additional emitters do not meet the threshold for single-photon emission, there is still a clear cross-correlation between the ZPLs, as shown in the Supplemental Material. However, we only observed a minority of emitters exhibiting cross-correlated ZPLs, which is a plausible consequence of a broad family of different defects being generated during the hBN annealing process. This is supported by the observation that the emitters described in the Supplemental Material do not exhibit any phonon sidebands, in contrast with the emitter discussed in this article. We would expect all emitters to have similar lineshapes if they are from the same defect.

5.5 Analysis and Conclusions

The auto- and cross-correlation functions and spectra for each emitter presented in Figures 5.1 and 5.2 provide experimental evidence for multiple excited states within a single hBN defect or complex of defects as proposed in Figure 5.2e. This model is consistent with previous polarimetric studies that described two excited states [201, 202]. The cross-correlations observed here would be expected, for example, from a two-excited state model when optically addressable charge states are present. The shelving observed may be explained most generally by two shelving states, and previous reports have suggested the existence of two shelving states determined through photophysics studies[121, 197]. However, the power dependence of shelving-state dynamics may indicate that there is only one

shelving state [207]. The results shown in Figure 5.2 do not conclusively address whether there is more than one shelving state present, but they provide clear evidence of anticorrelations between the two ZPLs.

Based on the cross-correlations between distinct ZPLs reported in Figure 5.2d and the Supplemental Material, it appears that ZPL_1 and ZPL_2 are associated with a single defect or a complex of defects so that an excited state can emit light into either ZPL_1 or ZPL_2. Alternatively, cross-correlations like those reported here could plausibly result from dipole-dipole interactions between two closely spaced, near-resonant emitters. We suggest that this alternative hypothesis is less plausible but provide a simple classical model of such a coupled defect system in the Supplemental Material. While we cannot reject the case of strongly interacting emitters, the preponderance of the evidence leads us to conclude that the observed cross-correlation are generated by the electronic structure of either a single point defect or a defect complex.

In summary, we have observed correlated laser-irradiation-dependent changes in the μPL intensity for two zero-phonon lines that reach equilibrium before simultaneously quenching in ambient laboratory conditions. These zero-phonon lines were confirmed to be antibunched and anti-correlated with one another. The cross-correlations between these two emitters indicates photochromism between the ZPL_1 and ZPL_2 transitions, consistent with a similar study of the charged and neutral nitrogen vacancy centers in diamond [207]. These results are therefore evidence that ZPL_1 and ZPL_2 are excited state transitions for the same defect or complex. This evidence of photochromism in hBN defects is an essential step toward improved understanding of the atomic origins of these defects.

5.6 Methods

The sample studied in this work was a multilayer hBN flake (3-5 layers in thickness) from Graphene Supermarket. The flake was subsequently annealed in a First Nano rapid thermal processor at a temperature of 850^oC in 1 Torr N_2 with a temperature increase and

decrease of 5^{o}C/min. For all experiments, a room-temperature confocal microscope with a continuous-wave 405 nm diode-laser excitation with $2\mu W$ incident on the sample and a 0.9 NA objective was used to collect μPL from defects in our sample. Laser-edge filters and dichroic mirrors were used to pass only μPL to our spectrometer or interferometer. For laser-irradiation-dependent spectroscopy, the μPL was passed to a diffraction grating spectrometer with 2 meV resolution. For singles counts and two-color HBT interferometry the μPL was passed to a beamsplitter with filters F1 (Newport 10LWF-500-B and 10SWF-550-B) and F2 (Semrock FF01-575/5-25) prior to the detectors corresponding to arm one and two of the HBT interferometer. The detectors were fiber coupled using multimode fiber and spatial mode filtering was adjusted using varying fiber core diameters (50-100 μm). Coincidence counts were collected using a HydraHarp 400 and the single photon detectors used were Perkin Elmer SPCM-AQRs.

5.7 Acknowledgments

This research was sponsored by the U. S. Department of Energy, Office of Science, Basic Energy Sciences, Materials Sciences and Engineering Division. Initial experimental planning and design was supported by the Laboratory-Directed Research and Development Program of Oak Ridge National Laboratory, managed by UT-Battelle, LLC for the U.S. Department of Energy. M.A.F. gratefully acknowledges support by the Department of Defense (DoD) through the National Defense Science & Engineering Graduate Fellowship (NDSEG) and NSF award DMR-1747426. C.E.M gratefully acknowledges postdoctoral research support from the Intelligence Community Postdoctoral Research Fellowship Program at the Oak Ridge National Laboratory, administered by Oak Ridge Institute for Science and Education through an interagency agreement between the U.S. Department of Energy and the Office of the Director of National Intelligence. Rapid thermal processing and spectroscopy experiments were carried out at the Center for Nanophase Materials Sciences (CNMS), which is sponsored at ORNL by the Scientific User Facilities Division,

Office of Basic Energy Sciences, U.S. Department of Energy. The authors thank Harrison Prosper for discussion on uncertainty estimation for the auto- and cross-correlation fits.

5.8 Disclosures

The authors declare no conflicts of interest.

See Supplement 1 for supporting content.

5.9 Supplement Material

5.9.1 Time-Dependent Photoluminescence Spectroscopy

The changes in the μPL spectra shown in Figure 1 of the main article can plausibly be attributed to changes in the charge state of ZPL_1 and ZPL_2 under optical pumping and to photochemical interactions with oxygen. Both the stable blueshift in ZPL_2 and its simultaneous reduction in μPL intensity potentially suggest that the local strain environment was modified as previously reported in first-principle studies of carrier recombination dynamics in hBN defects[208]. However, we do not observe a shift in ZPL_1. While there have been studies showing ZPL transitions insensitive to strain fields due to differences in transition symmetry[209], further study of the strain tuning of these ZPLs is needed to make a conclusive statement and is outside the scope of this article. Furthermore, we find it equally plausible that the blue-shift in ZPL_2 is due to slow spectral diffusion or a modification in the local environment of the defect. Previous work has studied the modification of hBN emitters under different laser excitation energies, environments, and irradiation time. Shotan *et al.* have shown that the μPL intensity of defects in one-to-five layer hBN flakes are enhanced under 405 nm excitation whereas only a fraction of defects fluoresce under 532 nm excitation[198]. The difference in absorption of 405 nm versus 532 nm light was attributed to the presence of additional excited states that compete with lower energy transitions. The same study demonstrated photobleaching and spectral jumps of defects under 405 nm excitation whereas defects were photostable under 532 nm excitation with

the sample in ambient conditions. It is possible that the observed spectral jumps may be due to a modification in the local environment of the defect. These observations are in agreement with the data in Shotan *et al.*'s work and additionally with previous works. For example, in Kanaev *et al.* they have shown a reduction in fluorescence and photobleaching of visible and ultraviolet transitions for near surface defects pumped at energies exceeding the activation energy for the photochemical decomposition of hBN of 2.57 eV under 99% molecular oxygen or air[203] while the μPL of such defects are known to be photostable under vacuum [210, 211, 147]. However, recently such results have also been shown to be clearly dependent on the excitation detuning from the ZPL[125].

The normalized singles counts for ZPL_1 (blue) and ZPL_2 (orange) for the defect discussed in the main article are shown in Figure 5.3. Correlated fluorescent dynamics were observed over timescales of 30 minutes between the zero-phonon lines. Interestingly, the singles counts from both zero-phonon lines completely quench simultaneously to within the 2 ms due to the lower photon count rate for ZPL_2 (2000 cps), which suggests these transitions are associated with the same defect or complex. Uncorrelated bursts in the fluorescence are attributed to blinking background defects or cosmic rays.

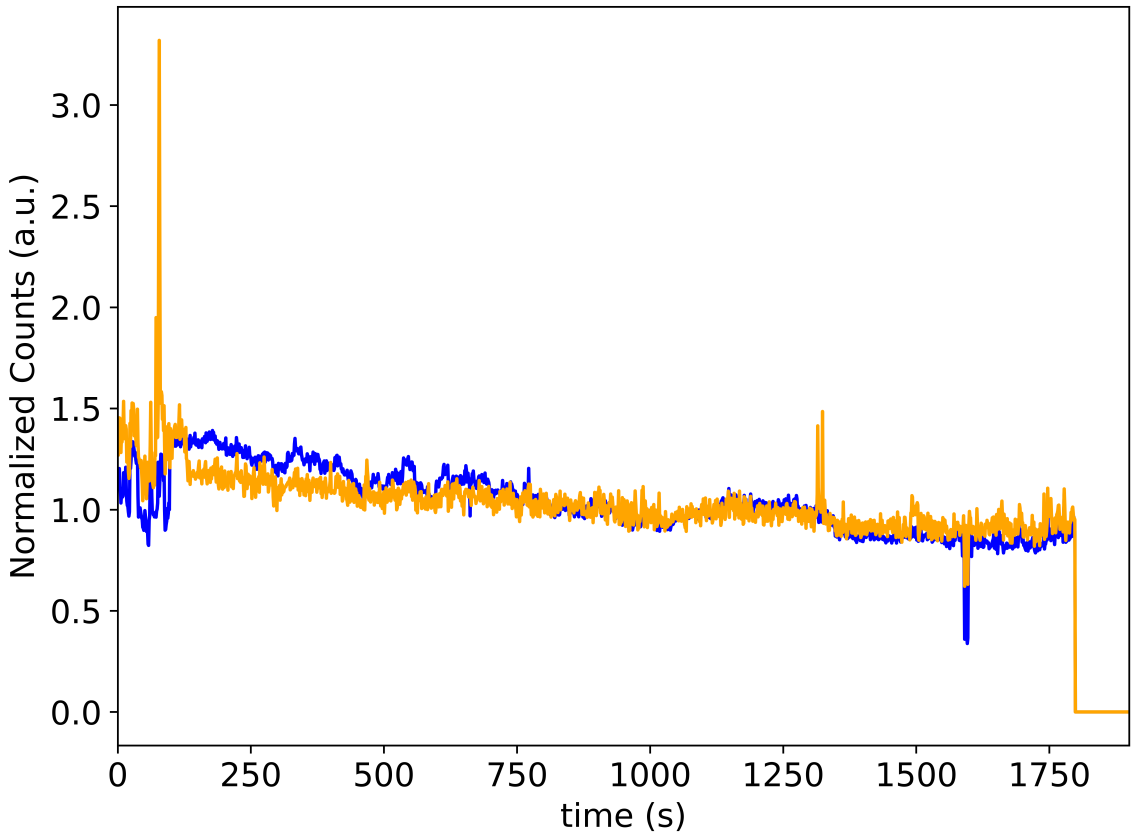

Figure 5.3: Singles counts for the photochromic emitter in the manuscript with ZPL_1 (blue) and ZPL_2 (orange) for the last 30 minutes of emission prior to photo-bleaching of ZPL_1 and ZPL_2

5.9.2 Fitting Methods For Defect Lineshape

A nonlinear least squares fit was performed to estimate the lineshape of the spectrum for each defect, as shown in Figure 5.4. The lineshapes corresponding to ZPL_1 and ZPL_2 were fit using a sum of a Lorentzian for the zero-phonon line, exponentially modified Gaussians for the acoustic phonon modes, two Gaussians for the one-phonon doublet and one Gaussian for the two-phonon sideband given by

$$S/\Gamma = A_1 \frac{1}{\pi} \frac{\frac{1}{2}\sigma_1}{(x-x_1)^2 + (\frac{1}{2}\sigma_1)^2} + \sum_{i=2,3} A_i \frac{\lambda_i}{2} e^{\frac{\lambda_i}{2}(2x_2 + \lambda_i * \sigma_i^2 - 2x)} \mathrm{erf}\left(\frac{x_i + \lambda\sigma_i^2 - x}{\sqrt{(2)}\sigma_2}\right) \tag{5.6}$$
$$+ A_4 \frac{1}{\sigma_4\sqrt{2\pi}} e^{\frac{1}{2}(\frac{x-x_4}{\sigma_4})^2} + A_5 \frac{1}{\sigma_5\sqrt{2\pi}} e^{\frac{1}{2}(\frac{x-x_5}{\sigma_5})^2} + A_6 \frac{1}{\sigma_6\sqrt{2\pi}} e^{\frac{1}{2}(\frac{x-x_6}{\sigma_6})^2},$$

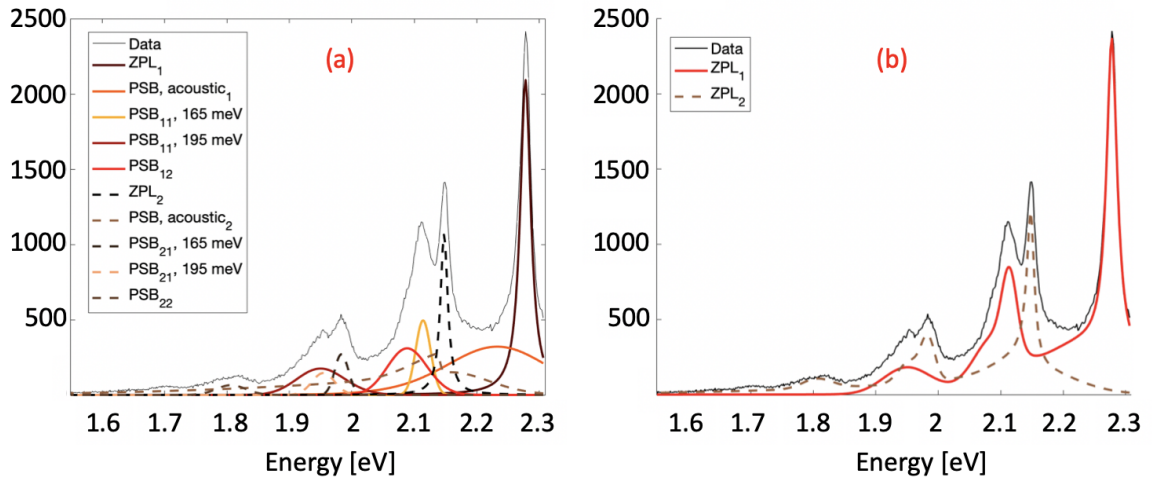

Figure 5.4: Nonlinear Least Squares Spectral Fits for two ZPLs and Corresponding PSBs. (a) Spectral subcomponents of lineshapes for ZPL_1 (solid-red color coded) and ZPL_2 (dashed-copper color coded). A legend is provided to help distinguish between the ZPL components and the acoustic, one-, and two-phonon sideband components for each of the ZPL linewidths. (b) The corresponding lineshapes for ZPL_1 (solid-red) and ZPL_2 (dashed copper). The grey and black traces in a) and b), respectively, are the PL spectrum after 1.8 hrs of laser irradiation.

where S is the lineshape of the defect spectrum, A_i is the amplitude of the transition, σ_i is the linewidth parameter, x_i is the transition peak energy, Γ is a lineshape amplitude scaling parameter and λ is the skewness parameter used in the acoustic phonon term. Fixed parameter bounds were used in the nonlinear least squares fit for each parameter. The interval for the transition peak energies corresponding to the expected redshift in the one-phonon (166±2 meV) and two-phonon (326±2 meV) peak energies relative to the zero-phonon line (2.15±2 meV) was given by the spectrometer resolution. This interval was also widened to ±4 meV to account for strain-induced red- and blue-shifting in the one-phonon and two-phonon energies observed in the literature. The interval for the peak energy of the acoustic phonons was set to ±40 meV consistent with previous observations [147]. The goodness of fits were also checked for the cases in which i) the ZPL_2 lineshape remained the same throughout the study by fixing all parameters except for the peak energy of the ZPL, x_1, and an additional parameter Γ that was left free to estimate the overall amplitude of the

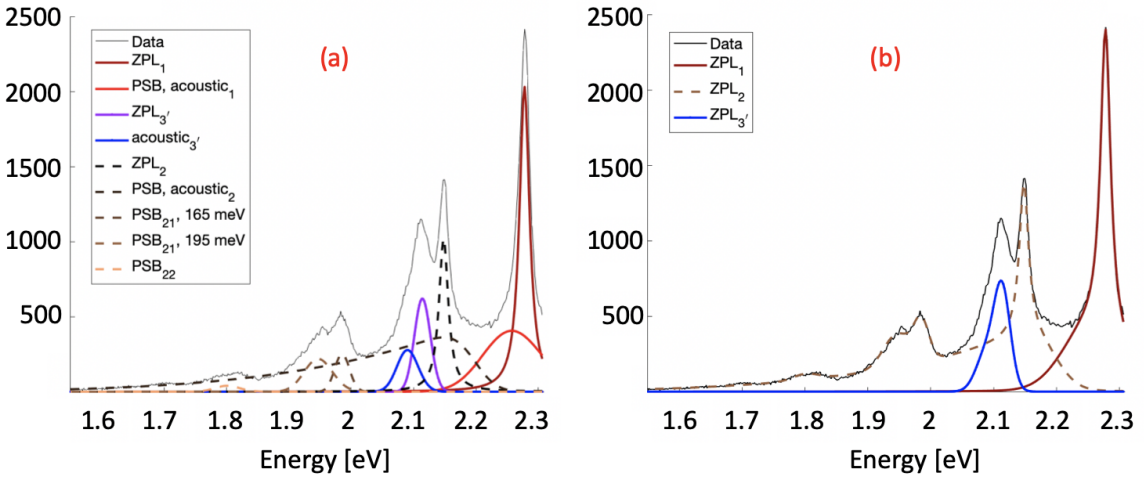

Figure 5.5: Nonlinear Least Squares Spectral Fits for 3 ZPLs and Corresponding PSBs. (a)Spectral subcomponents of lineshapes for ZPL_1 (solid-red color coded) and ZPL_2 (dashed-copper color coded). The blue and purple peaks are assumed to be from a third emitter ZPL_3' distinct from ZPL_1 and ZPL_2. A legend is provided to help distinguish between the ZPL components and the acoustic, one-, and two-phonon sideband components for each of the ZPL linewidths. (b) The corresponding lineshapes for ZPL_1 (solid dark red) and ZPL_2 (dashed copper) and an uncorrelated emitter (solid blue). The grey and black traces in a) and b) are the PL spectrum at 1.8 hrs of laser irradiation.

lineshape and ii) the lineshape was modified during the blue-shift observed after two-hours of irradiation by leaving all parameters free in S and fixing Γ to 1. The goodness-of-fit was estimated using the coefficient of variation R^2 where $R^2 \geq 0.99$ in all cases considered for the spectra at 0 hrs and 1.8 hrs (see Figures 5.4, 5.5 and the inset to 2a in the main article).

To test the plausibility that ZPL_1 is a group 2 emitter and the blue and purple peaks in Figure 5.5a are emission from a third zero-phonon line and acoustic PSB of an uncorrelated emitter, we dropped the phonon sideband terms in the fit for the ZPL_1 lineshape. In this case, while the goodness-of-fit was comparable to the fits which assume both ZPL_1 and ZPL_2 are group 1, the corresponding negligible background ($\sim 1\%$ of the total intensity) emission of the ZPL_1 lineshape that overlaps with the filter F2 is inconsistent with the background ($\sim 10\%$ of the total intensity) detected in the auto-correlation measurements for the ZPL_2. Therefore, we reject the hypothesis that ZPL_1 is of group 2. For the case where we assume that both ZPLs are of group 1 we find that the background emission observed in

the auto-correlations for ZPL_2 and the cross-correlation between ZPL_1 and ZPL_2 is taken into account by the spectral overlap of the ZPL_1 one-phonon sideband with the transfer function of filter F2 (see Figure 5.4b). Fits for all defect emission that was assumed to be an uncorrelated emitter either used the above fit function or a single Gaussian term.

5.9.3 Derivation of the Auto- and Cross-correlations

To account for the effect of multiple emitters in the detection confocal volume on the correlations we let the total intensity on the i^{th} channel of the HBT interferometer be $I_{i,tot} = \Sigma_j I_{ij}$ where the contribution of the j^{th} emitter's intensity is $I_{ij} = z_{ij} I_{i,tot}$, which emits with some probability z_{ij} to contribute to the total intensity such that $\Sigma_j z_{ij} = 1$[206]. For ZPL_1 this leads to

$$\begin{aligned}
\langle I_{ZPL_1}(t)\rangle^2 g_1^{(2)}(\tau) &= \langle I_{ZPL_1}(t) I_{ZPL_1}(t+\tau)\rangle, \qquad (5.7)\\
&= \langle I_{ZPL_1}(z_{11}(t) + z_{13}(t) + z_{14}(t) + z_{15}(t)) \\
&\quad \times I_{ZPL_1}(z_{11}(t+\tau) + z_{13}(t+\tau) + z_{14}(t+\tau) + z_{15}(t+\tau))\rangle, \\
g_1^{(2)}(\tau) &= z_{11}^2 g_1^{(2)}(\tau) + z_{13}^2 g_3^{(2)}(\tau) + z_{14}^2 g_4^{(2)}(\tau)^2 + z_{15}^2 g_5^{(2)}(\tau) \\
&\quad + 2(z_{11}z_{13} + z_{11}z_{15} + z_{11}z_{14} + z_{13}z_{15} + z_{13}z_{14} + z_{15}z_{14}), \\
&= (z_{11}^2 + z_{13}^2 + z_{14}^2 + z_{15}^2) g_{p1}^{(2)}(\tau) \\
&\quad + 2(z_{11}z_{13} + z_{11}z_{15} + z_{11}z_{14} + z_{13}z_{15} + z_{13}z_{14} + z_{15}z_{14}), \qquad (5.8)
\end{aligned}$$

where $g_i^{(2)}(\tau)$ is the second order coherence observable for the i^{th} emitter transition, and $g_{p1}^{(2)}(\tau)$ is the second order coherence using a three-level state model. In order to reduce the number of fit parameters, we set $g_1^{(2)}(\tau) = g_3^{(2)}(\tau) = g_4^{(2)}(\tau) = g_5^{(2)}(\tau)$. Based on the assumption that the background emission intensities I_{13}, I_{14} and I_{15} are independent and uncorrelated, all cross-terms will be constant with respect to τ as seen in equation 3[206].

For the auto-correlation of ZPL_2 we have a similar derivation given by

$$\langle I_{ZPL_2}\rangle^2 g_2^{(2)}(\tau) = \langle I^2_{ZPL_2}(z_{21}(t)+z_{22}(t))(z_{21}(t+\tau)+z_{22}(t+\tau))\rangle, \tag{5.9}$$

$$\begin{aligned} g_2^{(2)}(\tau) &= z_{21}(t)z_{21}(t+\tau)+z_{22}(t)z_{22}(t+\tau)+z_{21}(t)z_{22}(t+\tau)+z_{22}(t)z_{21}(t+\tau), \\ &= (z_{21}^2+z_{22}^2)g_{p2}^{(2)}(\tau)+z_{21}z_{22}(g_{12}^{(2)}(\tau)+g_{21}^{(2)}(\tau)), \end{aligned} \tag{5.10}$$

where the cross terms now involve second order coherences $g_{12}^{(2)}(\tau)$ and $g_{21}^{(2)}(\tau)$ from the correlated transitions ZPL_1 and ZPL_2 due to the spectral overlap of their lineshapes in filter F2. As a result, the cross-terms are no longer constant. The contribution of the time-dependent cross-terms to the antibunching can be as much as 25% to $g_2^{(2)}(\tau)$ and have the same time-dependence as the antibunching of the signal. However, the signal plus the cross-terms for $g^{(2)}(0)$ is still significantly ($>5\sigma$) below the threshold ($g^{(2)}_{limit,2}$) for single-photon emission as discussed in the main article. If we were able to disentangle the $g_{p2}^{(2)}(\tau)$ signal from the background, the single-photon purity for ZPL_2 would be even higher.

Finally the cross-correlation between ZPL_1 and ZPL_2 is given by

$$\begin{aligned} \langle I_{ZPL1}I_{ZPL2}\rangle^2 g_{21}^{(2)}(\tau) &= \langle I_{ZPL_2}(z_{21}(t)+z_{22}(t)) \\ &\quad \times I_{ZPL_1}(z_{11}(t+\tau)+z_{13}(t+\tau)+z_{14}(t+\tau)+z_{15}(t+\tau))\rangle, \end{aligned} \tag{5.11}$$

$$\begin{aligned} g_{21}^{(2)}(\tau) &= z_{11}(t)z_{22}(t+\tau)+z_{22}(t)z_{13}(t+\tau)+z_{22}(t)z_{14}(t+\tau) \\ &\quad + z_{22}(t)z_{15}(t+\tau)+z_{21}(t)z_{11}(t+\tau)+z_{21}(t)z_{13}(t+\tau) \\ &\quad + z_{21}(t)z_{14}(t+\tau)+z_{21}(t)z_{15}(t+\tau), \\ g_{21}^{(2)}(\tau) &= z_{11}z_{22}g_{p21}^{(2)}(\tau)+z_{11}z_{21}g_1^{(2)}(\tau)+z_{13}+z_{14}+z_{15}, \end{aligned} \tag{5.12}$$

where the cross-term $z_{11}z_{22}g_{p21}^{(2)}(\tau)$ involves the correlated zero-phonon lines ZPL_1 and ZPL_2 with cross-correlation $g_{p21}^{(2)}(\tau)$. Again, due to the partial overlap of the ZPL_1 lineshape with filter F2, the auto-correlation for ZPL_1 ($g_1^{(2)}(\tau)$) is included in the cross-term between

z_{11} and z_{21}. Despite this term contributing up to 15% to $g^{(2)}_{21}(\tau)$ and having the same time-dependence as the signal $g^{(2)}_{\rho 21}(\tau)$, the signal plus the cross-terms is significantly ($\gg 5\sigma$) below the threshold ($g^{(2)}_{limit,21}$) for a anti-correlation due to single-photon emission from distinct transitions.

5.9.4 Additional Cross-Correlation Data

Four additional clearly distinct ZPL lineshapes (labeled ZPL$_j$, $j = 6,7,8,9$ in Figure 5.6(a) and 5.7(a) were observed on a separate site on the same sample discussed in the article. Photoluminescence spectra were taken at room temperature (blue) and at 4K (red). An overall shift of 4±0.5 meV in the ZPL peak energies was observed consistent with previous reports due to expansion of the lattice as a function of temperature[200]. VersaChrome tunable bandpass Semrock filters (TBP01-547-15,TBP01-617-14) were used for all interferometry indicated by the blue bandpass in Figures 5.6a and 5.7a. All of the additional correlation data was collected at 4K. As seen in Figure 5.6b-c and 5.7b-c, the photon statistics indicate that we do not meet the threshold for single photon emission from one emitter. To model the photon statistics for the auto- ($g^{(2)}_j(\tau)$) and cross-correlations ($g^{(2)}_{ij}(\tau)$), we incorporate a background term assuming N of the same emitter types are present given by

$$g^{(2)}_{j\rho}(\tau) = g^{(2)}_{ij\rho}(\tau) = 1 - \frac{\rho^2}{N}[(1+a_n)e^{-|x-x_{on}|/\tau_{1n}} - a_n e^{-|x-x_{on}|/\tau_{2n}}], \tag{5.13}$$

where $n = j$ for the auto-correlation and $n = ij$ for the cross-correlation, and all other parameters are defined in the main article. We again do not observe any significant Poisson statistics contributing to the background and thus it is not a major source of background emission. Rather, with this model we find an ensemble of 3 to 6 emitters contribute to the observed spectrum. Remarkably, cross-correlations are still present, suggesting the presence of an ensemble of the same emitters with two optically accessible transitions. The parameters for each correlation are provided in Table 5.3.

In addition, there is no evidence of phonon sidebands in the lineshapes for ZPL_6, ZPL_8 and ZPL_9. If the emitters responsible for the ZPL emission described in the main article and those presented in this section were all from the same defect type then we would instead expect a consistent lineshape for the defects, counter to our results.

$g^{(2)}_{\rho n}(\tau)$	a	τ_{1i} (ns)	τ_{2i} (ns)
$g^{(2)}_{\rho 6}(\tau)$	0.55	1.5	105
$g^{(2)}_{\rho 8}(\tau)$	0.41	2.1	141
$g^{(2)}_{\rho 9}(\tau)$	0.72	2.6	111
$g^{(2)}_{\rho 86}(\tau)$	0.36	1.8	186
$g^{(2)}_{\rho 89}(\tau)$	0.41	3.7	153

Table 5.3: Parameter values for the auto- and cross-correlation functions of emitters 6, 8 and 9

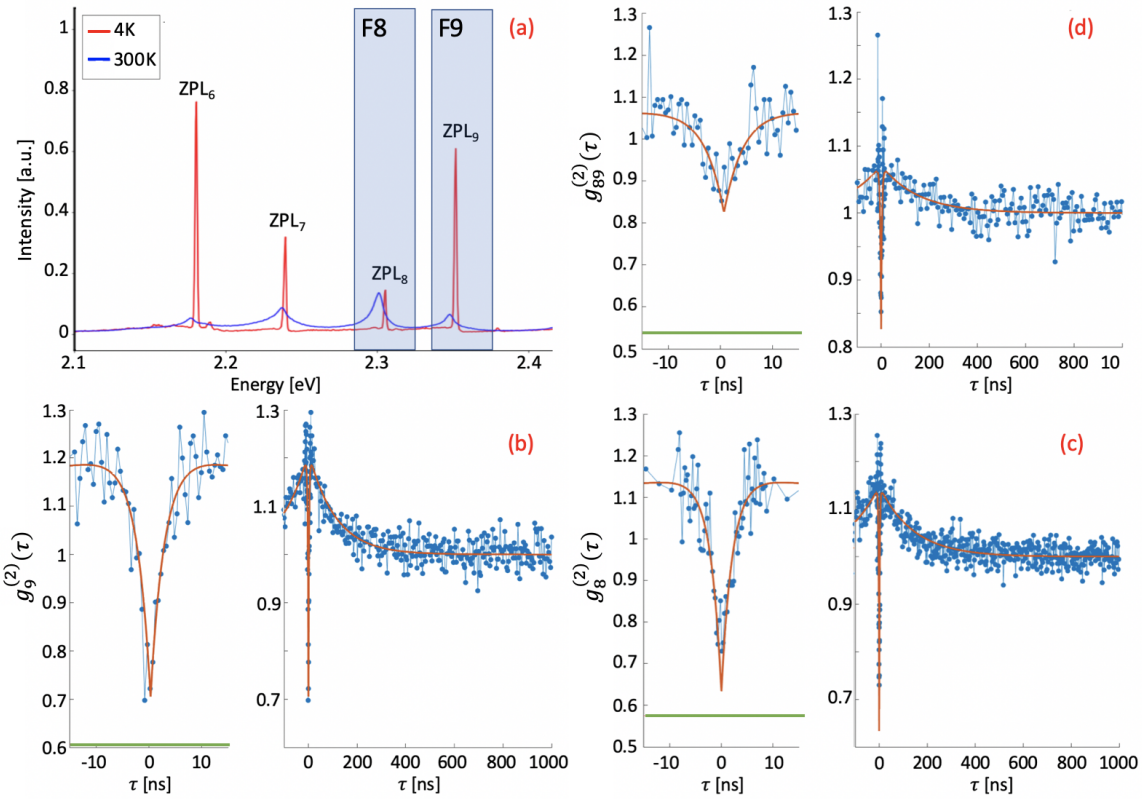

Figure 5.6: Two-color HBT interferometry between ZPL transition 8 and 9. a) Spectrum of four transitions labeled ZPL_j, $j = 6,7,8,9$ taken at 4K (red) and 300K (blue). Filters F8 and F9 (represented by translucent blue rectangles) are placed at the output arms of the HBT interferometer to collect μPL for ZPL_8 and ZPL_9, respectively. b) The auto-correlation $g_9^{(2)}(\tau)$ for ZPL_9 and c) $g_8^{(2)}(\tau)$ for ZPL_8 and d) the cross-correlation $g_{89}^{(2)}(\tau)$ between ZPL_8 and ZPL_9.The threshold for single photon emission is given by the green horizontal lines for the auto- and cross-correlations. All correlation data were taken at 4K.

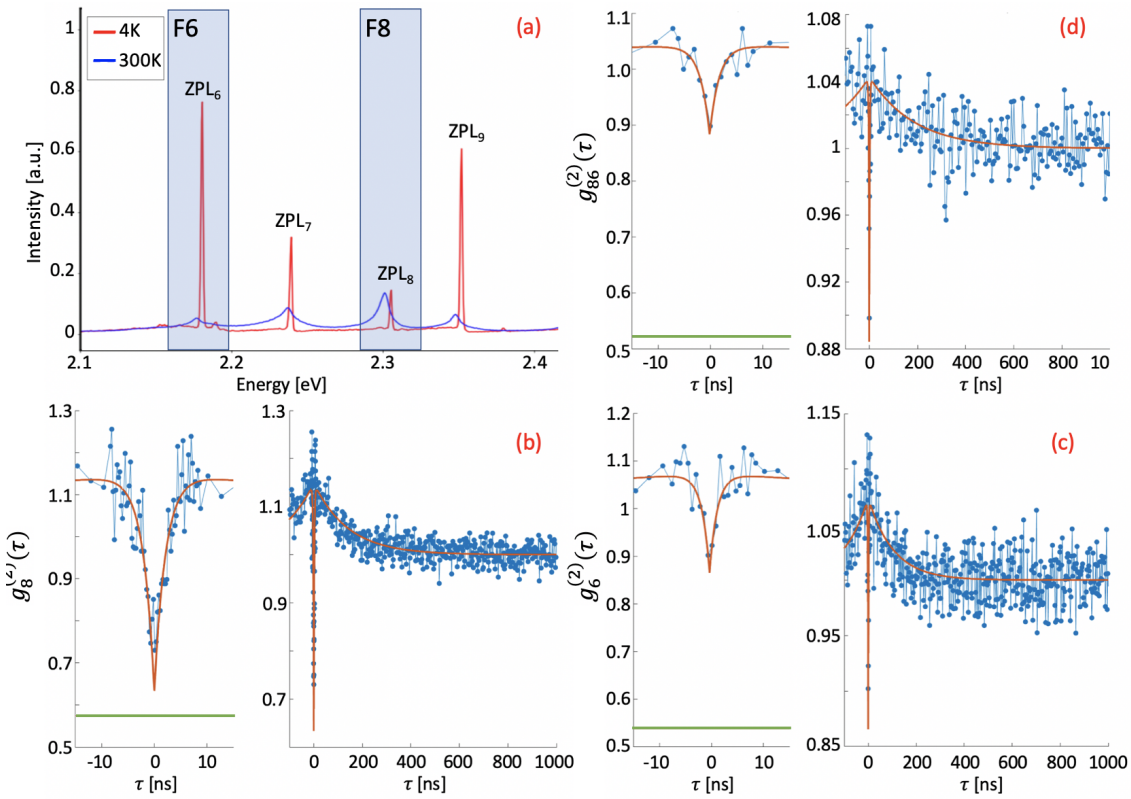

Figure 5.7: Two-color HBT interferometry between ZPL transition 6 and 8. a) Spectrum of four transitions labeled ZPL_j, $j = 6,7,8,9$ taken at 4K (red) and 300K (blue). Filters F6 and F8 (represented by translucent blue rectangles) are placed at the output arms of the HBT to collect μPL for transitions ZPL_6 and ZPL_8, respectively. b) the auto-correlations $g_8^{(2)}(\tau)$ for ZPL_8 and c) $g_6^{(2)}(\tau)$ for ZPL_6 and d) the cross-correlation $g_{86}^{(2)}(\tau)$ between ZPL_8 and ZPL_6. The threshold for single photon emission is given by the green horizontal lines for the auto- and cross-correlations. All correlation data were taken at 4K.

5.9.5 Dipole-Dipole Coupling Toy Model

While it appears that ZPL_1 and ZPL_2 are associated with a single defect or a complex of defects, an alternative possibility is that the cross-correlations are a result of the dipole-dipole interaction energy E_{dd} between two closely spaced, near-resonant emitters. We can approximate the interaction energy $E_{dd} = \mu_1\mu_2/(4\pi\epsilon r^3)$ where $\mu_1 = \mu_2 = ed$ is the dipole moment for each emitter, e is the charge of an electron, $d = 0.1nm$ is the distance between the poles of the dipole, ϵ is the permittivity of hBN, and r is the distance between dipoles. As a limiting case, we assume no charge screening ($E_{dd} \sim 1/r^3$). While defects have been found to be within 50 nm of one another[196], electronic dipole-dipole interaction strengths

at this distance are a negligible $\sim 10^{-8}$ eV. In the limiting case of a separation between emitters of $\sim$1 nm the interaction strength would be $\sim$3 meV, likely leading to the states of the two emitters hybridizing to form an effective defect complex[212]. In this case, we would expect $g_{21}^{(2)}(0) < 0.5$. Engineering these sorts of interactions between emitters often requires deterministic placement of defects[212] and controllable cavity interactions[213]. Furthermore, optimal coupling of emitters is also dependent on Stark tuning[214] of the transitions and can require quasi-resonant pumping[215] of transitions to generate antibunched sub-Poissonian photon statistics in the cross-correlations between the coupled transitions. While this model does not take into account quantum effects of the i) defect dipole-dipole interactions nor ii) the electro-optical properties of hBN, we are still led to conclude that the hypothesis of two strongly interacting emitters is less likely than the model presented in the main article.

Chapter 6

Summary and Outlook

6.1 Summary

The experimental methods of microphotoluminescence (μPL) spectroscopy, Hanbury-Brown Twiss (HBT) interferometry and confocal microscopy have been combined to identify SQEs in hBN. Two-color HBT interferometry and μPL spectroscopy have been used to reveal strong cross-correlations i) between the SQE's zero-phonon line and its phonon sidebands (PSB) and ii) between two ZPLs. The former was covered in chapter 3 and the latter was reviewed in chapter 4. Here I review the main conclusions from the results.

In the experiments described in chapter 3, we observed broad emission redshifted 165 and 326 meV from the ZPL of hBN SQEs. These phonon sidebands were modeled using a Huang-Rhys model of the μPL, taking into account the phonon density of states (DOS) of the lattice. By reweighting the phonon DOS we found good agreement between experiment and theory. However, the necessity to reweight terms in the phonon DOS indicated that there are either selection rules causing the phonon DOS to differ from those expected for hBN or there are local vibrational modes of the defect not accounted for in our analysis. Despite this limitation we were able to show that the 165 and 326 meV modes are one- and two-phonon sidebands by measuring single-photon cross-correlations between these modes and the corresponding ZPLs.

In chapter 4 we reported the results of experiments that showed a fraction of SQEs in hBN exhibit cross-correlations and correlated microphotoluminescence between group II ZPLs. We also determined that the emission is single-photon in nature for the auto-correlation of each ZPL and the cross-correlation between these ZPLs. This result provides evidence of this defect having an excited state structure composed of two excited states with radiative transitions. These results indicated the possible presence of excited states with a charge or spin degrees of freedom. Alternatively, the ZPL emission may originate

from a complex of defects since when defects are in close proximity (~1 nm) they interact strongly and their states will be expected to hybridize.

6.2 Outlook

Through my six years of research, the field of hBN color centers has progressed a great deal. The community as a whole has been able to advance an understanding of what is likely a wide variety of defects that exist within hBN. However, there are still major improvements to be made. There are at least four main areas of fundamental and applied research that the field will continue to pursue. Namely for hBN defects, continuing to identify their atomic origins, identification of their local vibrational and phonon modes, continued characterization of their spin properties, and improving their optical properties to make an exceptional SQE.

6.2.1 Defect Identification

Initially, the field was limited in its ability to classify hBN defects relying primarily on the group I and group II phenomenological characterization according to ZPL energy and electron-phonon coupling. While the V_B^- and the $V_BC_N^-$ defects have recently been identified due to their spin-triplet ground state, many observed defects, such as i) ultra-violet defect, ii) defects which do not exhibit magnetic properties, and iii) defects that exhibit multiple excited states have not been accounted for fully or conclusively. Moreover, the V_B^- and the $V_BC_N^-$ defects have been found to have optical and spin properties necessary for their operation as SQEs or quantum memories but it is not clear that the remaining unidentified defects are suited for use as SQEs or quantum memories. I pose the question to the reader whether further pursuit of identifying defects is warranted? If so, to help identify other defect species experimental studies must conduct large surveys of defects incorporating concurrent measures of μPL spectroscopy, two-color HBT interferometry, magneto-optical spectroscopy and ODMR. This will aid in identifying all the electronic, phonon, spin and magnetic properties of the defect. Additionally, The spatial resolution

to implant and detect defects must be increased to further confirm the detection of SQEs. Defects can be created using nano-ion implantation capabilities detected using either time-resolved scanning near-field optical microscopy (SNOM) or scanning transmission electron microscopy (STEM) as the excitation source. In particular, STEM is an attractive excitation source since this opens the door for correlative studies of μPL, ODMR and the atomic structure of defects. The results of these combined efforts can be used by theorists, in turn, to determine the appropriate family of defects to model and their expected properties.

Furthermore, previous studies have been performed across different fabrication methods to inject nonnative atomic species into hBN to form defects [154]. These correlative studies have shown great promise in being able to identify defects as done with the carbon defect ($V_B C_N^-$). This process should be pursued further for other defect species in the future to correlate the observed μPL, ODMR and two-color HBT interferometry to said atomic species as described in Table 6.1. This table is presented for illustrative purposes only.

Atomic defect	hBN fabrication	Defect Fabrication	Characterization
Oxygen based	MBE	MOVPE	ODMR, μPL, two-color HBT
Oxygen based	MBE	ion implantation	ODMR, μPL, two-color HBT
Boron vacancy	MBE	neutron irradiation	ODMR, μPL, two-color HBT
Boron vacancy	MBE	electron irradiation	ODMR, μPL, two-color HBT

Table 6.1: Examples of suggested correlated studies of fabrication methods and their effect on SQE measuremensts (ODMR, μPL, two-color HBT interferometry). For molecular beam epitaxy (MBE) a saphhire substrate is used. For metal-organic vapour-phase epitaxy (MOVPE) a oxygen precursor is assumed.

6.2.2 Electron-Phonon Coupling

The electron-phonon coupling of hBN defects has been characterized using unidentified defects. The phonon modes observed for these defects match the phonon modes of hBN. However, no observations of local vibrational modes, a key signature of the defect species, have been made to date. For experimentalists to aid in the effort of identifying local modes, high-resolution photoluminescent excitation (PLE) spectroscopy studies should be conducted with i) bulk-hBN and ii) suspended few-layer hBN to minimize the effects

of the substrate interactions with phonons in hBN. These studies should be systemic with large sample sizes of defects. An initial set of defects to explore are the V_B^- and the $V_BC_N^-$ defects. To corroborate the initial identification of V_B^- and the $V_BC_N^-$ defects, experimentalists should confirm by PLE spectroscopy that the observed vibrational modes are consistent with theoretical predictions. Further studies can be envisioned focusing on yet unidentified defects.

An additional point of clarity needed in the electron-phonon coupling for SQEs in hBN is the effect different isotopes of boron and nitrogen have on the SQE phonon-sideband (PSB). To date PSB studies have been performed on hBN, which has a natural abundance of ^{10}B, ^{11}B, ^{14}N, and ^{15}N. However, the phonon density of states of hBN will have peak energies associated with each of these isotopes. For unidentified defects, it will be necessary to identify the contribution of modes to the phonon DOS and the phonon sideband of the defect. This will aid further in determining the contributions to the phonon density of states, which are due to phonons or localized modes.

6.2.3 Spin Characterization

With the recent discovery of optically accessible spin states in the V_B^- and the $V_BC_N^-$ defects in hBN the next appropriate step is to determine the spin lifetimes and spin coherence of these defects to determine their viability as quantum memories and as magnetometers. Determining the spin coherence in particular will be of key importance in determining the quality of its quantum memory since the dephasing time (T_2^*) determines how insensitive the spin is to dephasing mechanisms. Initial studies will be conducted at room temperature. But performing spin lifetime and spin dephasing measurements as a function of temperature and magnetic field will also elucidate the relaxation and dephasing mechanisms affecting these defects. Both of which are critical to understanding how to optimally control hBN quantum memories. A spin spectroscopy facility has been developed for this purpose the details of which can be found in appendix A. Likewise the sensitivity of color center based

DC-magnetometers scales monotonically with T_2^*. Once T_2^* is known initial applications of these defects as magnetometers can be considered to determine their feasibility to measure local magnetic fields at the mesoscale.

6.2.4 Towards indistinguishable SQEs

While defects in few-layer hBN are exceedingly bright and photostable at room temperature they have yet to reach the Fourier limit for their optical coherence times. These defects in few-layer hBN have been reported to have linewidths broadened from spectral diffusion over prolonged integration times exceeding 30s . Currently, these defects are not sufficiently capable of acting as a SQE since they do not generate indistinguishable photons. To overcome this limitation fundamental studies must first be conducted to determine the absorption linewidths of defects in bulk-hBN where defects are implanted well below the surface ($\gg$ 50 nm). This is to avoid interactions with surface charges and the electric dipole moment of the defect, thereby limiting the effects of spectral diffusion. These measurements will thereby act as a lower bound on the absorption linewidths. Presuming defects in bulk-hBN are not lifetime-limited, then continued pursuits should be taken to couple defects to optical cavities thereby exploiting a Purcell enhancement in the optical lifetimes to reach the Fourier limit.

Appendix A

Appendix A: A mK Spin Spectroscopy Facility

1.1 Introduction

A myriad of quantum physics and quantum information science based technologies require operation at extremely low temperatures on the order of ~100 mK. For example, the silicon vacancy in diamond requires operation at mK temperatures to mitigate against phonon-induced spin decoherence processes [94]. Additionally, the temperature dependence of the spin coherence and spin lifetimes for V_B^- and $V_B C_N^-$ defects in hBN have yet to be characterized. To access and control SQEs at mK temperatures a confocal microscope or optical fiber access must be made available to a dilution refrigerator. Furthermore, excitation optics and software control are necessary to perform initialization and readout pulses for SQE spin relaxometry and spin coherence measurements. In this section I will discuss the development of and technical details for a dilution refrigerator, scanning confocal microscope in a dilution refrigerator and corresponding excitation optics and software meant to perform spin spectroscopy at mK temperatures.

1.2 Dilution Refrigerator

Experiments operating at mK temperatures require a dilution refrigerator. A dilution refrigerator works by condensing helium three and helium four in a mixing circuit, which forms a dilute and concentrated phase of the helium three in its superfluid state within the mixing chamber. The flow of the helium 3 from the concentrated phase to the dilute phase absorbs heat from the mixing chamber.

We have a Leiden Cryogenics dilution refrigerator with a cold insertable probe, which allows for rapid sample transfer of 1 day. The refrigerator's key parameters for its performance are its base temperature and its cooling power. Our refrigerator's cryostat has a base temperature of 14 mK whereas the base temperature of the probe is 19 mK. This base

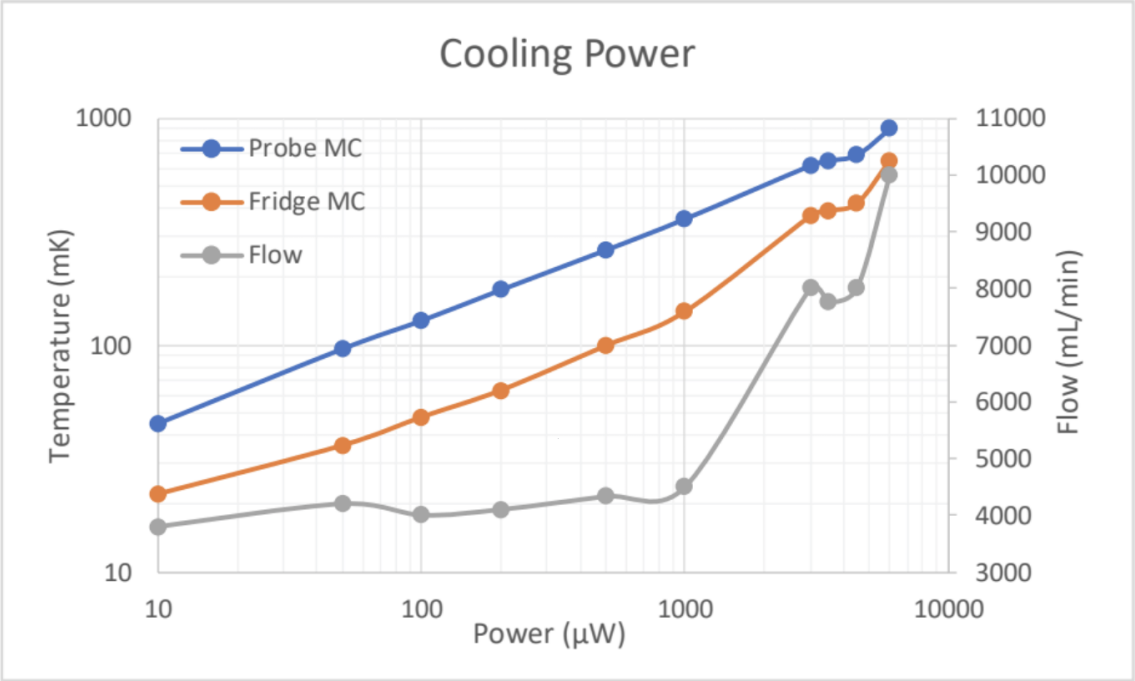

Figure 1.1: Cooling power of the dilution refrigerator. At 128 μW of applied power to the mixing chamber plate of the probe, the probe is stable at 100 mK and the mixing chamber of the fridge is stable at 48 mK. Above 6 mW of applied power, the circulation flow is no longer able to keep up with the heat load, and the system begins mixture recovery. The base temperature of the probe during this measurement was 45 mK, due to a poorly clamped probe.

temperature is highly dependent on the thermal conductivity between each thermal stage of the refrigerator cryostat and the probe (*e.g.* the mixing chambers for the refrigerator and the probe). Under normal operation, the cold insertable probe is clamped to each thermal stage of the fridge using a pneumatic actuator. However, when the fridge is not optimally pumped, ice can form on the clamps thereby decreasing the base temperature of the probe. To assure a low base temperature the fridge and probe are evacuated of any residual gasses by pumping a vacuum of 1e-6 torr and purging each with helium before cooling. Under normal conditions, the cooling power for the probe is 128 μW at 100 mK as shown in Figure 1.1.

1.3 Development of a mK-Scanning Confocal Microscope

In this section, I cover the technical aspects of how I built a scanning confocal microscope into a dilution refrigerator. The integration of a confocal microscope into a dilution refrigerator requires the fridge to have minimal vibrations, free-space optical access, as well as a mK-cryogenic objective. Piezo-motorized stages are necessary for sample and objective positioning. We include all of this functionality in our dilution refrigerator. The cold insertable probe has an 8 mm diameter free-space access at each stage. We include optical windows to filter out black body radiation. At the bottom of the mixing chamber, a NA=0.84 cryogenic objective is positioned onto a z-axis piezo-stage. Below that is a three-axis xyz-stage for sample positioning. The sample stage is thermally sunk to the mixing chamber via thermal braids.

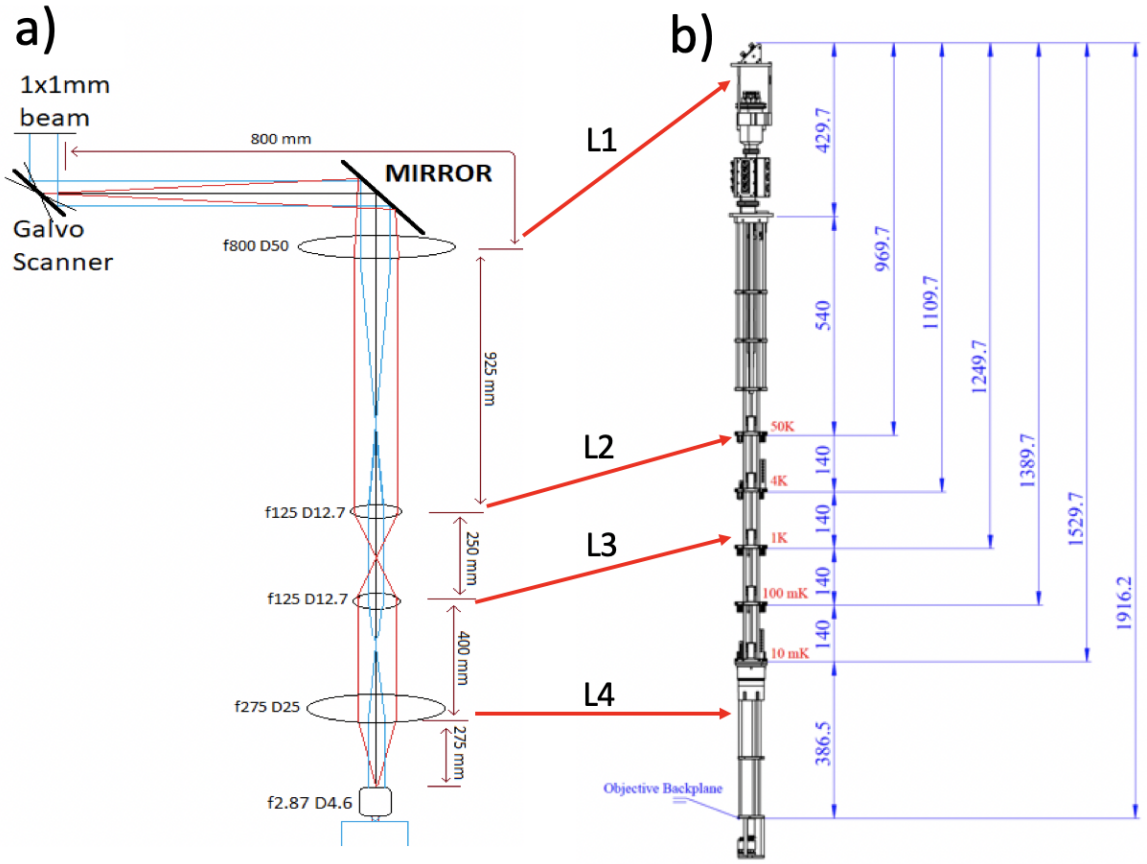

Figure 1.2: 8F Scanning imaging system. a) the ray optics simulation for a 8F scanning imaging system. b) is a diagram of the cold insertable probe with the positions of the four lenses L1-L4 of the 8F imaging system

However, the DC current applied from the stages can induce larger thermal gradients $\sim$ 100 mK and so other scanning capabilities are necessary, which minimize heating during scans. An 8F (concatenated 4F) imaging system coupled to a galvanometer-based scanning mirror capability is suitable for this application. In this case, the only heat deposited within the fridge is that generated from the black body radiation and scattered laser light during scans, which is minimal in power ($\sim \mu$W) and heats the fridge only $\sim$ 10 mK above its base temperature. The selection of an 8F imaging system requires four lenses where each nearest neighbor lenses i and j are separated by a distance $d = f_i + f_j$. Here these two lenses apply Fourier and inverse Fourier transforms thus creating a reversed replica of an input image (i.e. input laser) at the output of the imaging system. The galvanometer mirror then allows for the steering of the laser onto the sample surface as shown in Figure 1.2.

Here four lenses L1-L4 are placed on the cold removable probe: one in the atmosphere outside the fridge, and one on the 50K stage, one on the 1K stage and one inside the mixing chamber stage. Using a ray optics simulator, Zeemax, we simulate a scan range of $\pm 36\mu$m. Our scan range is ultimately limited by the 8 mm diameter clear aperture of our 1 meter long radiation shield on the cold insertable probe. We implement this design using L1-L4 with focal lengths F1 = 80cm, F2=F3=12.5cm, and F4= 27.5 cm lenses.

The remaining optics for collection and part of excitation are placed onto a custom-made optics breadboard, which is situated on top of the dilution refrigerator cryostat as shown in Figure 1.3. Laser light is passed from the excitation arm to a low-pass dichroic mirror (DM), which reflects the laser beam onto the galvanometer mirror and 8F imaging system. The light is focused onto a confocal diameter of $\sim 1\mu$m on the sample under test. By the principle of reciprocity, light emitted by the sample is collected by the objective and traverses the reversed ray path for excitation. The collected light from the sample is then transmitted across the dichroic mirror (DM) and passed to the collection arm. The sample light is then passed to a low pass filter, which blocks the residual laser light. The collected sample light is then passed to either a camera for imaging, a single photon counting

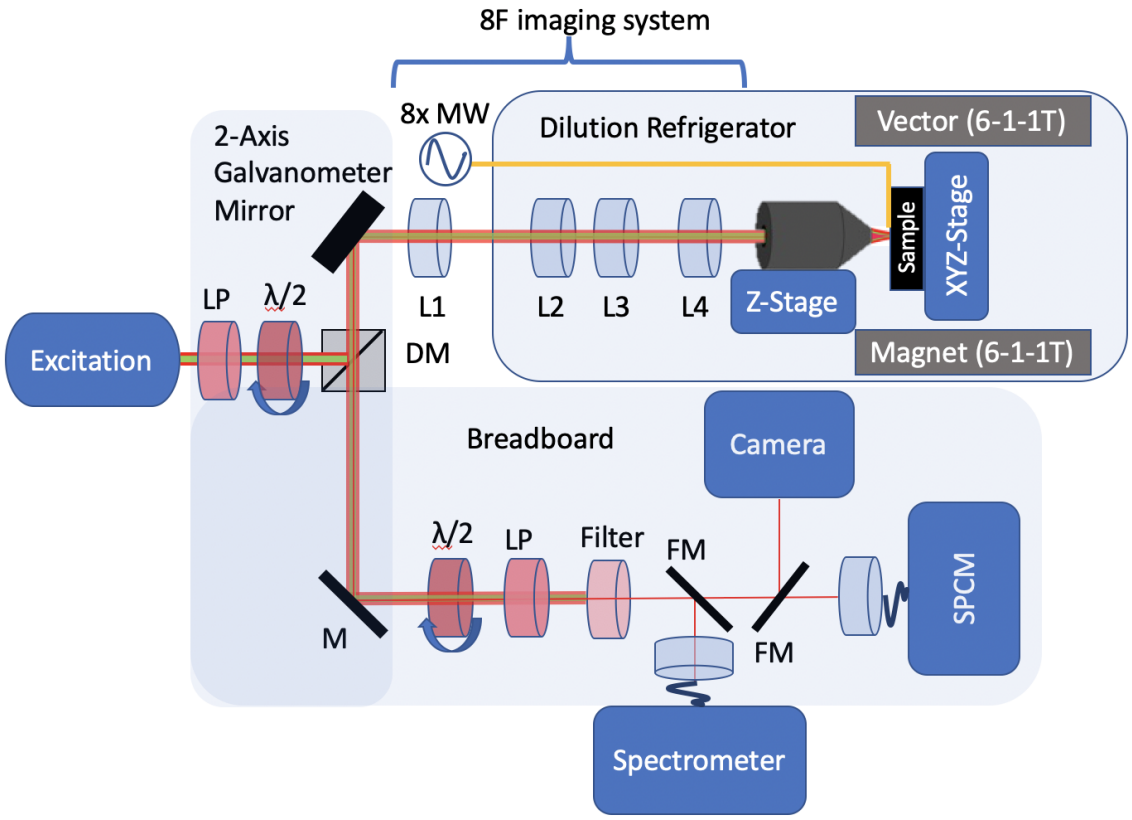

Figure 1.3: Collection optics for a mK-scanning confocal microscope. Laser light from the excitation arm is reflected off a low-pass dichroic mirror (DM) to a 2-axis galvanometer mirror, which reflects the laser light onto the 8F imaging system. The 8F imaging system comprises lenses L1-L4 steering the light onto a position on the cryogenic objective, which focuses light on the sample. Photoluminescence (PL) from the sample is collected by the objective and by reciprocity is passed to the DM where it is transmitted to a mirror (M), which passes the light to a laser clean up filter. The PL is then selectively passed to either a spectrometer, a camera or a single-photon counting module using two flip mirrors (FM).

module for ODMR experiments, or a spectrometer to collect spectra. Polarization optics (linear polarizer, and a half-wave plate) are optionally included in the excitation and collection to allow for absorption and emission polarimetry. For ODMR style experiments eight microwave lines are included in the cold insertable probe to drive SQEs spin states coherently. Likewise, a 6-1-1 T vector magnet is housed inside the dilution refrigerator cryostat to allow for aligning static magnetic fields along the symmetry axis of the defect during OMDR experiments. Generally, this is done to limit the state readout from being an admixutre of spin up and spin down, which makes the defect system less spin conserving and more difficult to readout the spin.

1.4 Excitation Optics

To perform spin relaxometry and spin coherence measurements requires pulse sequences of laser light, microwaves and readout periods. Defects with triplet ground states and a corresponding intersystem crossing relaxation pathways only require off-resonant laser light for spin state initialization and readout [70]. Whereas defects with spin-orbit selection rules require excitation pulses resonant with the spin state to be initialized or readout [94, 97]. An additional recharging pulse is often used before resonant excitation pulses as well to assure the defect is repumped into the correct charge state. For this purpose, I used two acousto-optic modulators (AOM) to convert cw 532 nm laser and the tunable output of an optical parametric oscillator into pulse laser light as seen in Figure 1.4. The AOM is pulsed by driving the AOM crystal with an 80 MHz carrier from a RF modulator. This drives phonons through the crystal generating 1st order diffraction modes with angular frequencies $\omega_l \pm \omega_p$, where ω_l is the laser frequency and ω_p is the phonon driving frequency. A Swabian pulsestreamer then controls the RF driver to activate the laser pulses. The 532 nm and tunable sources laser light are passed onto separate AOMs and their first order diffraction modes are combined with a 50/50 beam splitter. The combined 532 nm and tunable laser light is passed to the excitation arm on the breadboard using a single-mode fiber. The polarization state of the laser is initialized using polarization optics on the breadboard. Additionally, a half-wave plate ($\lambda/2$) and a polarization beam splitter (PBS) are in the path of each AOM to control the power of each source input into the dilution refrigerator cryostat.

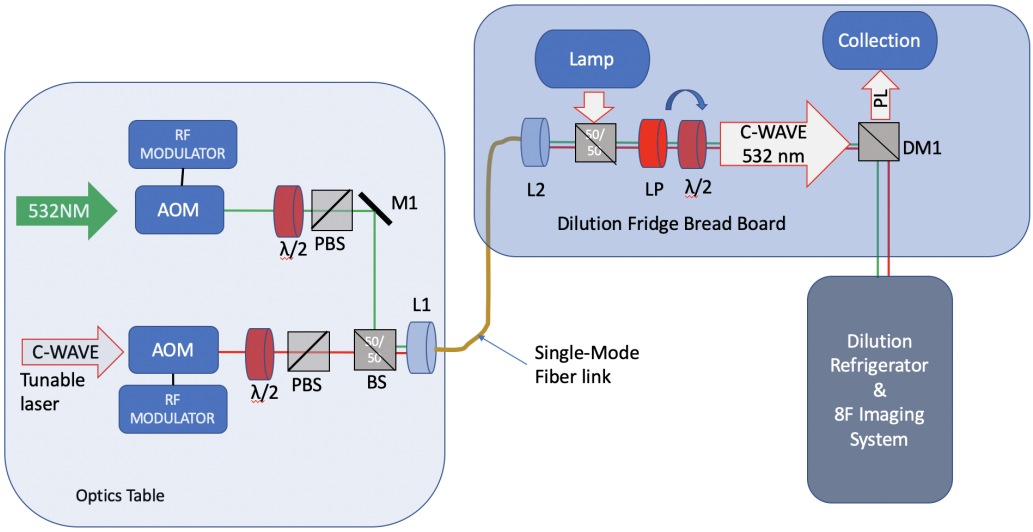

Figure 1.4: Excitation optics for mK-scanning confocal microscope. Here a 532 nm and tunable laser light from a Millenia Edge and CWave OPO laser are input into an acousto-optic modulator (AOM). The first-order mode of each source is passed to separate half-wave plates ($\lambda/2$) and polarization beam splitters (PBS) to control the power for each source. The light of each source is combined on a beam splitter (BS) and fiber-coupled to the excitation optics on the refrigerator breadboard using lenses L1 and L2 and a single-mode fiber. A lamp source, used for imaging, is combined with the laser sources on a BS. The optical polarization is initialized using a linear polarizer (LP) and a half-wave plate ($\lambda/2$). The light is then reflected off a dichroic mirror (DM) into the dilution refrigerator.

1.5 Software

The control of ODMR pulse sequences was implemented using the CommandCenter software package available at https://github.com/mwalsh161/CommandCenter/tree/ornl_stopgap. This application has various layers in the software stack meant to i) manage software modules, ii) implement experiments, data collection ann iii) establish control and operation of photon source and corresponding drivers. For this facility, I wrote drivers and photon-sources (referred to as sources from here on out) for our Cwave tunable laser, 532 nm laser, microwave signal generator, and pulsestreamer. The total collection of drivers and sources written for this facility are provided below in bullet format.

- Drivers

  - CWave Laser
  - Microwave Signal Generator
  - 532 nm Laser
  - Pulsestreamer

- Sources
  - CWave Laser
  - Microwave Signal Generator
  - 532 nm Laser

The pulsestreamer driver controls the pulsestreamer and allows for the downloading, running, stopping and starting of pulsesequences to the pulsestreamer. The laser and microwave drivers provide at a minimum functionality to i) initialize the driver, ii) turn the hardware (laser, microwave signal generator, etc) on and off, and iii) tuning methods to control the laser frequency for the case of tunable lasers such as the CWave. The laser or microwave signal generator drivers were then combined with the pulsestreamer driver to enable a controllable pulsed source. Each source can be selected and used during an experiment to run a pulse sequences.

REFERENCES

[1]Nicholas R. Jungwirth and Gregory D. Fuchs. Optical Absorption and Emission Mechanisms of Single Defects in Hexagonal Boron Nitride. *Physical Review Letters*, 119(5):1–6, 2017.

[2]Toan Trong Tran, Christopher ElBadawi, Daniel Totonjian, Charlene J Lobo, Gabriele Grosso, Hyowon Moon, Dirk R Englund, Michael John Ford, Igor Aharonovich, and Milos Toth. Robust multicolor single photon emission from point defects in hexagonal boron nitride. *arXiv:*, page 1603.09608, 2016.

[3]C. L. Degen, F. Reinhard, and P. Cappellaro. Quantum sensing. *Reviews of Modern Physics*, 89(3):1–39, 2017.

[4]C. Zu, W. B. Wang, L. He, W. G. Zhang, C. Y. Dai, F. Wang, and L. M. Duan. Experimental Realization of Universal Geometric Quantum Gates with Solid-State Spins. *Nature*, 514:2–6, 2014.

[5]N. Bar-Gill, L. M. Pham, A. Jarmola, D. Budker, and R. L. Walsworth. Solid-state electronic spin coherence time approaching one second. *Nature Communications*, 4:1743–1746, 2013.

[6]Peter C. Maurer, Georg Kucsko, Christian Latta, Liang Jiang, Norman Y. Yao, Steven D. Bennett, Fernando Pastawski, David Hunger, Nicholas Chisholm, Matthew Markham, Daniel J. Twitchen, J. Ignacio Cirac, and Mikhail D. Lukin. Room-temperature quantum bit memory exceeding one second. *Optics InfoBase Conference Papers*, (June):1283–1287, 2013.

[7]C. T. Nguyen, D. D. Sukachev, M. K. Bhaskar, B. MacHielse, D. S. Levonian, E. N. Knall, P. Stroganov, C. Chia, M. J. Burek, R. Riedinger, H. Park, M. Lončar, and M. D. Lukin. An integrated nanophotonic quantum register based on silicon-vacancy spins in diamond. *Physical Review B*, 100(16):1–19, 2019.

[8]Christiana Panayi, Mohsen Razavi, Xiongfeng Ma, and Norbert Lütkenhaus. Memory-assisted measurement-device-independent quantum key distribution. *New Journal of Physics*, 16, 2014.

[9]Tie Jun Wang, Si Yu Song, and Gui Lu Long. Quantum repeater based on spatial entanglement of photons and quantum-dot spins in optical microcavities. *Physical Review A - Atomic, Molecular, and Optical Physics*, 85(6):1–11, 2012.

[10]Chun Yan Wei, Tian Yin Wang, and Fei Gao. Practical quantum private query with better performance in resisting joint-measurement attack. *Physical Review A*, 93(4):1–7, 2016.

[11]Nicoló Lo Piparo, Mohsen Razavi, and William J. Munro. Memory-assisted quantum key distribution with a single nitrogen-vacancy center. *Physical Review A*, 96(5):1–9, 2017.

[12]Filip RozpÈl'dek, Raja Yehia, Kenneth Goodenough, Maximilian Ruf, Peter C. Humphreys, Ronald Hanson, Stephanie Wehner, and David Elkouss. Near-term quantum-repeater experiments with nitrogen-vacancy centers: Overcoming the limitations of direct transmission. *Physical Review A*, 99(5):1–29, 2019.

[13]Samuel L. Braunstein and Stefano Pirandola. Side-channel-free quantum key distribution. *Physical Review Letters*, 108(13):1–4, 2012.

[14]M. K. Bhaskar, R. Riedinger, B. Machielse, D. S. Levonian, C. T. Nguyen, E. N. Knall, H. Park, D. Englund, M. Lončar, D. D. Sukachev, and M. D. Lukin. Experimental demonstration of memory-enhanced quantum communication. *Nature*, 580(7801):60–64, 2020.

[15]Wolfgang Tittel, Mikael Afzelius, Thierry Chanelière, Rufus L. Cone, Stefan Kröll, Sergey A. Moiseev, and Matthew Sellars. Photon-echo quantum memory in solid state systems. *Laser and Photonics Reviews*, 4(2):244–267, 2010.

[16]Manjin Zhong, Morgan P. Hedges, Rose L. Ahlefeldt, John G. Bartholomew, Sarah E. Beavan, Sven M. Wittig, Jevon J. Longdell, and Matthew J. Sellars. Optically addressable nuclear spins in a solid with a six-hour coherence time. *Nature*, 517(7533):177–180, 2015.

[17]H. J. Briegel, W. Dür, J. I. Cirac, and P. Zoller. Quantum repeaters: The role of imperfect local operations in quantum communication. *Physical Review Letters*, 81(26):5932–5935, 1998.

[18]Christoph Simon, Hugues De Riedmatten, Mikael Afzelius, Nicolas Sangouard, Hugo Zbinden, and Nicolas Gisin. Quantum repeaters with photon pair sources and multimode memories. *Physical Review Letters*, 98(19):1–4, 2007.

[19]Bo Zhao, Zeng Bing Chen, Yu Ao Chen, Jörg Schmiedmayer, and Jian Wei Pan. Robust creation of entanglement between remote memory qubits. *Physical Review Letters*, 98(24):1–4, 2007.

[20]Nicolas Sangouard, Christoph Simon, Hugues De Riedmatten, and Nicolas Gisin. Quantum repeaters based on atomic ensembles and linear optics. *Reviews of Modern Physics*, 83(1):33–80, 2011.

[21]Andreas Reiserer, Norbert Kalb, Gerhard Rempe, and Stephan Ritter. A quantum gate between a flying optical photon and a single trapped atom. *Nature*, 508(7495):237–240, 2014.

[22]Wang Yao, Ren Bao Liu, and L. J. Sham. Theory of control of the spin-photon interface for quantum networks. *Physical Review Letters*, 95(3):1–4, 2005.

[23]Sreraman Muralidharan, Jungsang Kim, Norbert Lütkenhaus, Mikhail D. Lukin, and Liang Jiang. Ultrafast and fault-tolerant quantum communication across long distances. *Physical Review Letters*, 112(25):1–6, 2014.

[24]Andreas Reiserer and Gerhard Rempe. Cavity-based quantum networks with single atoms and optical photons. *Reviews of Modern Physics*, 87(4):1379–1418, 2015.

[25]Aurélien Cuche, Yannick Sonnefraud, Orestis Faklaris, Damien Garrot, Jean Paul Boudou, Thierry Sauvage, Jean François Roch, François Treussart, and Serge Huant. Near-field optical microscopy with a nanodiamond-based single-photon tip. *Optics express*, 17(22):19969–19980, 2009.

[26]Gopalakrishnan Balasubramanian, I. Y. Chan, Roman Kolesov, Mohannad Al-Hmoud, Julia Tisler, Chang Shin, Changdong Kim, Aleksander Wojcik, Philip R. Hemmer, Anke Krueger, Tobias Hanke, Alfred Leitenstorfer, Rudolf Bratschitsch, Fedor Jelezko, and Jörg Wrachtrup. Nanoscale imaging magnetometry with diamond spins under ambient conditions. *Nature*, 455(7213):648–651, 2008.

[27]Simon Schmitt, Tuvia Gefen, Felix M Stürner, Thomas Unden, Gerhard Wolff, Christoph Müller, Jochen Scheuer, Boris Naydenov, Matthew Markham, Sebastien Pezzagna, Jan Meijer, Ilai Schwarz, Martin Plenio, Alex Retzker, Liam P Mcguinness, and Fedor Jelezko. quantum sensor. 837(May):832–837, 2017.

[28]L. Thiel, Z. Wang, M. A. Tschudin, D. Rohner, I. Gutiérrez-Lezama, N. Ubrig, M. Gibertini, E. Giannini, A. F. Morpurgo, and P. Maletinsky. Probing magnetism in 2D materials at the nanoscale with single-spin microscopy. *Science*, 364(6444):973–976, 2019.

[29]P. Maletinsky, S. Hong, M. S. Grinolds, B. Hausmann, M. D. Lukin, R. L. Walsworth, M. Loncar, and A. Yacoby. A robust scanning diamond sensor for nanoscale imaging with single nitrogen-vacancy centres. *Nature Nanotechnology*, 7(5):320–324, 2012.

[30]Francesco Casola, Toeno Van Der Sar, and Amir Yacoby. Probing condensed matter physics. pages 8–12, 2018.

[31]G. Waldherr, J. Beck, P. Neumann, R. S. Said, M. Nitsche, M. L. Markham, D. J. Twitchen, J. Twamley, F. Jelezko, and J. Wrachtrup. High-dynamic-range magnetometry with a single nuclear spin in diamond. *Nature Nanotechnology*, 7(2):105–108, 2012.

[32]N. M. Nusran, M. Ummal Momeen, and M. V.Gurudev Dutt. High-dynamic-range magnetometry with a single electronic spin in diamond. *Nature Nanotechnology*, 7(2):109–113, 2012.

[33]C. Bonato, M. S. Blok, H. T. Dinani, D. W. Berry, M. L. Markham, D. J. Twitchen, and R. Hanson. Optimized quantum sensing with a single electron spin using real-time adaptive measurements. *Nature Nanotechnology*, 11(3):247–252, 2016.

[34]Paola Cappellaro. Spin-bath narrowing with adaptive parameter estimation. *Physical Review A - Atomic, Molecular, and Optical Physics*, 85(3):1–5, 2012.

[35]Hossein T. Dinani, Dominic W. Berry, Raul Gonzalez, Jeronimo R. Maze, and Cristian Bonato. Bayesian estimation for quantum sensing in the absence of single-shot detection. *Physical Review B*, 99(12):1–7, 2019.

[36]R. Santagati, A. A. Gentile, S. Knauer, S. Schmitt, S. Paesani, C. Granade, N. Wiebe, C. Osterkamp, L. P. McGuinness, J. Wang, M. G. Thompson, J. G. Rarity, F. Jelezko, and A. Laing. Magnetic-Field Learning Using a Single Electronic Spin in Diamond with One-Photon Readout at Room Temperature. *Physical Review X*, 9(2):21019, 2019.

[37]Cristian Bonato and Dominic W. Berry. Adaptive tracking of a time-varying field with a quantum sensor. *Physical Review A*, 95(5):1–10, 2017.

[38]Sandu Popescu, Noah Linden, and Richard Jozsa. Quantum Information and Computation. *Journal of Physics A: Mathematical and General*, 34(35):6723–6723, 2001.

[39]T. D. Ladd, F. Jelezko, R. Laflamme, Y. Nakamura, C. Monroe, and J. L. O'Brien. Quantum computers. *Nature*, 464(7285):45–53, 2010.

[40]Pieter Kok, W. J. Munro, Kae Nemoto, T. C. Ralph, Jonathan P. Dowling, and G. J. Milburn. Linear optical quantum computing with photonic qubits. *Reviews of Modern Physics*, 79(1):135–174, 2007.

[41]R. Blatt and C. F. Roos. Quantum simulations with trapped ions. *Nature Physics*, 8(4):277–284, 2012.

[42]David J. Wineland. Nobel Lecture: Superposition, entanglement, and raising Schrödinger's cat. *Reviews of Modern Physics*, 85(3):1103–1114, 2013.

[43]J. M. Raimond. Quantum information processing with atoms and cavities. *Superlattices and Microstructures*, 32(4-6):187–193, 2002.

[44]M. Saffman, T. G. Walker, and K. Mølmer. Quantum information with Rydberg atoms. *Reviews of Modern Physics*, 82(3):2313–2363, 2010.

[45]M. H. Devoret, A. Wallraff, and J. M. Martinis. Superconducting Qubits: A Short Review. 2004.

[46]G. Wendin. Quantum information processing with superconducting circuits: A review. *Reports on Progress in Physics*, 80(10), 2017.

[47]Bjoern Lekitsch, Sebastian Weidt, Austin G. Fowler, Klaus Mølmer, Simon J. Devitt, Christof Wunderlich, and Winfried K. Hensinger. Blueprint for a microwave trapped ion quantum computer. *Science Advances*, 3(2):1–12, 2017.

[48]Rosa Brouri, Alexios Beveratos, Jean-Philippe Poizat, and Philippe Grangier. Photon antibunching in the fluorescence of individual color centers in diamond. *Optics Letters*, 25(17):1294, 2000.

[49]F. Jelezko and J. Wrachtrup. Single defect centres in diamond: A review. *Physica Status Solidi (A) Applications and Materials Science*, 203(13):3207–3225, 2006.

[50]David D. Awschalom, Ronald Hanson, Jörg Wrachtrup, and Brian B. Zhou. Quantum technologies with optically interfaced solid-state spins. *Nature Photonics*, 12(9):516–527, 2018.

[51]I. Aharonovich, S. Castelletto, D. A. Simpson, C. H. Su, A. D. Greentree, and S. Prawer. Diamond-based single-photon emitters. *Reports on Progress in Physics*, 74(7), 2011.

[52]Igor Aharonovich, Dirk Englund, and Milos Toth. Solid-state single-photon emitters. *Nature Photonics*, 10(10):631–641, 2016.

[53]Igor Aharonovich and Elke Neu. Diamond nanophotonics. *Advanced Optical Materials*, 2014.

[54]Birgit J M Hausmann, Brendan Shields, Qimin Quan, Patrick Maletinsky, Murray McCutcheon, Jennifer T. Choy, Tom M. Babinec, Alexander Kubanek, Amir Yacoby, Mikhail D. Lukin, and Marko Lončar. Integrated diamond networks for quantum nanophotonics. *Nano Letters*, 12(3):1578–1582, 2012.

[55]R. E. Evans, M. K. Bhaskar, D. D. Sukachev, C. T. Nguyen, A. Sipahigil, M. J. Burek, B. Machielse, G. H. Zhang, A. S. Zibrov, E. Bielejec, H. Park, M. Lončar, and M. D. Lukin. Photon-mediated interactions between quantum emitters in a diamond nanocavity. *Science*, 362(6415):662–665, 2018.

[56]A. Sipahigil, R. E. Evans, D. D. Sukachev, M. J. Burek, J. Borregaard, M. K. Bhaskar, C. T. Nguyen, J. L. Pacheco, H. A. Atikian, C. Meuwly, R. M. Camacho, F. Jelezko, E. Bielejec, H. Park, M. Lončar, and M. D. Lukin. An integrated diamond nanophotonics platform for quantum-optical networks. *Science*, 354(6314):847–850, 2016.

[57]Carlo Bradac, Weibo Gao, Jacopo Forneris, Matthew E. Trusheim, and Igor Aharonovich. Quantum nanophotonics with group IV defects in diamond. *Nature Communications*, 10(1):1–13, 2019.

[58]L. J. Rogers, K. D. Jahnke, T. Teraji, L. Marseglia, C. Müller, B. Naydenov, H. Schauffert, C. Kranz, J. Isoya, L. P. McGuinness, and F. Jelezko. Multiple intrinsically identical single-photon emitters in the solid state. *Nature Communications*, 5:1–2, 2014.

[59]Michael J. Burek, Nathalie P. De Leon, Brendan J. Shields, Birgit J.M. Hausmann, Yiwen Chu, Qimin Quan, Alexander S. Zibrov, Hongkun Park, Mikhail D. Lukin, and Marko Lončar. Free-standing mechanical and photonic nanostructures in single-crystal diamond. *Nano Letters*, 12(12):6084–6089, 2012.

[60]A. Sipahigil, M. L. Goldman, E. Togan, Y. Chu, M. Markham, D. J. Twitchen, A. S. Zibrov, A. Kubanek, and M. D. Lukin. Quantum interference of single photons from remote nitrogen-vacancy centers in diamond. *Physical Review Letters*, 108(14):1–5, 2012.

[61]A. Sipahigil, K. D. Jahnke, L. J. Rogers, T. Teraji, J. Isoya, A. S. Zibrov, F. Jelezko, and M. D. Lukin. Indistinguishable photons from separated silicon-vacancy centers in diamond. *Physical Review Letters*, 113(11):1–5, 2014.

[62]Charles Santori, David Fattal, Jelena Vučković, Glenn S. Solomon, and Yoshihisa Yamamoto. Indistinguishable photons from a single-photon device. *Nature*, 419(6907):594–597, 2002.

[63]Hannes Bernien, Lilian Childress, Lucio Robledo, Matthew Markham, Daniel Twitchen, and Ronald Hanson. Two-photon quantum interference from separate nitrogen vacancy centers in diamond. *Physical Review Letters*, 108(4):1–5, 2012.

[64]G. D. Fuchs, G. Burkard, P. V. Klimov, and D. D. Awschalom. A quantum memory intrinsic to single nitrogen-vacancy centres in diamond. *Nature Physics*, 7(10):789–793, 2011.

[65]K. F. Reim, P. Michelberger, K. C. Lee, J. Nunn, N. K. Langford, and I. A. Walmsley. Single-photon-level quantum memory at room temperature. *Physical Review Letters*, 107(5):1–4, 2011.

[66]Colin D. Bruzewicz, John Chiaverini, Robert McConnell, and Jeremy M. Sage. Trapped-ion quantum computing: Progress and challenges. *Applied Physics Reviews*, 6(2), 2019.

[67]Michael J. Biercuk, Hermann Uys, Aaron P. VanDevender, Nobuyasu Shiga, Wayne M. Itano, and John J. Bollinger. Optimized dynamical decoupling in a model quantum memory. *Nature*, 458(7241):996–1000, 2009.

[68]Holger P. Specht, Christian Nölleke, Andreas Reiserer, Manuel Uphoff, Eden Figueroa, Stephan Ritter, and Gerhard Rempe. A single-atom quantum memory. *Nature*, 473(7346):190–193, 2011.

[69]R. Zhao, Y. O. Dudin, S. D. Jenkins, C. J. Campbell, D. N. Matsukevich, T. A.B. Kennedy, and A. Kuzmich. Long-lived quantum memory. *Nature Physics*, 5(2):100–104, 2009.

[70]John F. Barry, Jennifer M. Schloss, Erik Bauch, Matthew J. Turner, Connor A. Hart, Linh M. Pham, and Ronald L. Walsworth. Sensitivity optimization for NV-diamond magnetometry. *Reviews of Modern Physics*, 92(1), 2020.

[71]Feng Liu, Alistair J. Brash, John O'Hara, Luis M.P.P. Martins, Catherine L. Phillips, Rikki J. Coles, Benjamin Royall, Edmund Clarke, Christopher Bentham, Nikola Prtljaga, Igor E. Itskevich, Luke R. Wilson, Maurice S. Skolnick, and A. Mark Fox. High Purcell factor generation of indistinguishable on-chip single photons. *Nature Nanotechnology*, (1):1–6, 2018.

[72]R. Stockill, C. Le Gall, C. Matthiesen, L. Huthmacher, E. Clarke, M. Hugues, and M. Atatüre. Quantum dot spin coherence governed by a strained nuclear environment. *Nature Communications*, 7(May):1–7, 2016.

[73]A. Jarmola, V. M. Acosta, K. Jensen, S. Chemerisov, and D. Budker. Temperature- and magnetic-field-dependent longitudinal spin relaxation in nitrogen-vacancy ensembles in diamond. *Physical Review Letters*, 108(19):1–5, 2012.

[74]Anaïs Dréau, Anna Tcheborateva, Aboubakr El Mahdaoui, Cristian Bonato, and Ronald Hanson. Quantum Frequency Conversion of Single Photons from a Nitrogen-Vacancy Center in Diamond to Telecommunication Wavelengths. *Physical Review Applied*, 9(6):1–8, 2018.

[75]A Lohrmann, B C Johnson, J C McCallum, and S Castelletto. A review on single photon sources in silicon carbide. *Reports on Progress in Physics*, 80(3):34502–34519, jan 2017.

[76]Kevin C. Miao, Alexandre Bourassa, Christopher P. Anderson, Samuel J. Whiteley, Alexander L. Crook, Sam L. Bayliss, Gary Wolfowicz, Gergõ Thiering, Péter Udvarhelyi, Viktor Ivády, Hiroshi Abe, Takeshi Ohshima, Ádám Gali, and David D. Awschalom. Electrically driven optical interferometry with spins in silicon carbide. *Science Advances*, 5(11), 2019.

[77]Gary Wolfowicz, Christopher P. Anderson, Berk Diler, Oleg G. Poluektov, F. Joseph Heremans, and David D. Awschalom. Vanadium spin qubits as telecom quantum emitters in silicon carbide. *Science Advances*, 6(18):2–10, 2020.

[78]William F. Koehl, Bob B. Buckley, F. Joseph Heremans, Greg Calusine, and David D. Awschalom. Room temperature coherent control of defect spin qubits in silicon carbide. *Nature*, 479(7371):84–87, 2011.

[79]Christopher P Anderson, Alexandre Bourassa, Kevin C Miao, Gary Wolfowicz, Peter J Mintun, Alexander L Crook, Hiroshi Abe, Jawad Ul Hassan, Nguyen T Son, Takeshi Ohshima, and David D Awschalom. Electrical and optical control of single spins integrated in scalable semiconductor devices. *Science*, 366(6470):1225–1230, 2019.

[80]Jun Feng Wang, Fei Fei Yan, Qiang Li, Zheng Hao Liu, He Liu, Guo Ping Guo, Li Ping Guo, Xiong Zhou, Jin Ming Cui, Jian Wang, Zong Quan Zhou, Xiao Ye Xu, Jin Shi Xu, Chuan Feng Li, and Guang Can Guo. Coherent Control of Nitrogen-Vacancy Center Spins in Silicon Carbide at Room Temperature. *Physical review letters*, 124(22):223601, 2020.

[81]Roland Nagy, Matthias Widmann, Matthias Niethammer, Durga B.R. Dasari, Ilja Gerhardt, Öney O. Soykal, Marina Radulaski, Takeshi Ohshima, Jelena Vučković, Nguyen Tien Son, Ivan G. Ivanov, Sophia E. Economou, Cristian Bonato, Sang Yun Lee, and Jörg Wrachtrup. Quantum Properties of Dichroic Silicon Vacancies in Silicon Carbide. *Physical Review Applied*, 9(3):25–27, 2018.

[82]Tian Zhong, Jonathan M Kindem, John G Bartholomew, Jake Rochman, Ioana Craiciu, Evan Miyazono, Marco Bettinelli, Enrico Cavalli, Varun Verma, Sae Woo Nam, Francesco Marsili, Matthew D Shaw, Andrew D Beyer, and Andrei Faraon. Controlled Retrieval. *Science*, 1395(September):1392–1395, 2017.

[83]Disheng Chen, Nikolay Zheludev, and WeiâĂŘbo Gao. Building Blocks for Quantum Network Based on GroupâĂŘIV SplitâĂŘVacancy Centers in Diamond. *Advanced Quantum Technologies*, 3(2):1900069, 2020.

[84]Amanuel M. Berhane, Kwang Yong Jeong, Zoltán Bodrog, Saskia Fiedler, Tim Schröder, Noelia Vico Triviño, Tomás Palacios, Adam Gali, Milos Toth, Dirk Englund, and Igor Aharonovich. Bright Room-Temperature Single-Photon Emission from Defects in Gallium Nitride. *Advanced Materials*, 29(12), 2017.

[85]M. Koperski, K. Nogajewski, A. Arora, V. Cherkez, P. Mallet, J. Y. Veuillen, J. Marcus, P. Kossacki, and M. Potemski. Single photon emitters in exfoliated WSe2structures. *Nature Nanotechnology*, 10(6):503–506, 2015.

[86]Yu Ming He, Genevieve Clark, John R. Schaibley, Yu He, Ming Cheng Chen, Yu Jia Wei, Xing Ding, Qiang Zhang, Wang Yao, Xiaodong Xu, Chao Yang Lu, and Jian Wei Pan. Single quantum emitters in monolayer semiconductors. *Nature Nanotechnology*, 10(6):497–502, 2015.

[87]Chitraleema Chakraborty, Laura Kinnischtzke, Kenneth M. Goodfellow, Ryan Beams, and A. Nick Vamivakas. Voltage-controlled quantum light from an atomically thin semiconductor. *Nature Nanotechnology*, 10(6):507–511, 2015.

[88]Ajit Srivastava, Meinrad Sidler, Adrien V. Allain, Dominik S. Lembke, Andras Kis, and A. Imamoglu. Optically active quantum dots in monolayer WSe2. *Nature Nanotechnology*, 10(6):491–496, 2015.

[89]Sumin Choi, Brett C. Johnson, Stefania Castelletto, Cuong Ton-That, Matthew R. Phillips, and Igor Aharonovich. Single photon emission from ZnO nanoparticles. *Applied Physics Letters*, 104(26), 2014.

[90]N. R. Jungwirth, Y. Y. Pai, H. S. Chang, E. R. Macquarrie, K. X. Nguyen, and G. D. Fuchs. A single-molecule approach to ZnO defect studies: Single photons and single defects. *Journal of Applied Physics*, 116(4), 2014.

[91]Alexander Högele, Christophe Galland, Martin Winger, and Atac ImamoÇğlu. Photon antibunching in the photoluminescence spectra of a single carbon nanotube. *Physical Review Letters*, 100(21):5–8, 2008.

[92]Gabriel I. López-Morales, Aziza Almanakly, Sitakanta Satapathy, Nicholas V. Proscia, Harishankar Jayakumar, Valery N. Khabashesku, Pulickel M. Ajayan, Carlos A. Meriles, and Vinod M. Menon. Room-temperature single photon emitters in cubic boron nitride nanocrystals. *Optical Materials Express*, 10(4):843, 2020.

[93]Toan Trong Tran, Kerem Bray, Michael J. Ford, Milos Toth, and Igor Aharonovich. Quantum Emission From Hexagonal Boron Nitride Monolayers. *Nature nanotechnology*, 11(January):37–41, oct 2015.

[94]D. D. Sukachev, A. Sipahigil, C. T. Nguyen, M. K. Bhaskar, R. E. Evans, F. Jelezko, and M. D. Lukin. Silicon-Vacancy Spin Qubit in Diamond: A Quantum Memory Exceeding 10 ms with Single-Shot State Readout. *Physical Review Letters*, 119(22):1–6, 2017.

[95]M. K. Bhaskar, D. D. Sukachev, A. Sipahigil, R. E. Evans, M. J. Burek, C. T. Nguyen, L. J. Rogers, P. Siyushev, M. H. Metsch, H. Park, F. Jelezko, M. Lončar, and M. D. Lukin. Quantum Nonlinear Optics with a Germanium-Vacancy Color Center in a Nanoscale Diamond Waveguide. *Physical Review Letters*, 118(22):1–6, 2017.

[96]Matthew E. Trusheim, Noel H. Wan, Kevin C. Chen, Christopher J. Ciccarino, Johannes Flick, Ravishankar Sundararaman, Girish Malladi, Eric Bersin, Michael Walsh, Benjamin Lienhard, Hassaram Bakhru, Prineha Narang, and Dirk Englund. Lead-related quantum emitters in diamond. *Physical Review B*, 99(7):1–7, 2019.

[97]Matthew E. Trusheim, Benjamin Pingault, Noel H. Wan, Mustafa GündoÇğan, Lorenzo De Santis, Romain Debroux, Dorian Gangloff, Carola Purser, Kevin C. Chen, Michael Walsh, Joshua J. Rose, Jonas N. Becker, Benjamin Lienhard, Eric Bersin, Ioannis Paradeisanos, Gang Wang, Dominika Lyzwa, Alejandro R.P. Montblanch, Girish Malladi, Hassaram Bakhru, Andrea C. Ferrari, Ian A. Walmsley, Mete Atatüre, and Dirk Englund. Transform-Limited Photons from a Coherent Tin-Vacancy Spin in Diamond. *Physical Review Letters*, 124(2), 2020.

[98]Gabriele Grosso, Hyowon Moon, Benjamin Lienhard, Sajid Ali, Dmitri K. Efetov, Marco M. Furchi, Pablo Jarillo-Herrero, Michael J. Ford, Igor Aharonovich, and Dirk Englund. Tunable and high-purity room temperature single-photon emission from atomic defects in hexagonal boron nitride. *Nature Communications*, 8(1):1–8, 2017.

[99]Xiangzhi Li, Gabriella D. Shepard, Andrew Cupo, Nicolas Camporeale, Kamran Shayan, Yue Luo, Vincent Meunier, and Stefan Strauf. Nonmagnetic Quantum Emitters in Boron Nitride with Ultranarrow and Sideband-Free Emission Spectra. *ACS Nano*, 11(7):6652–6660, 2017.

[100]Andreas Gottscholl, Mehran Kianinia, Victor Soltamov, Sergei Orlinskii, Georgy Mamin, Carlo Bradac, Christian Kasper, Klaus Krambrock, Andreas Sperlich, Milos Toth, Igor Aharonovich, and Vladimir Dyakonov. Initialization and read-out of intrinsic spin defects in a van der Waals crystal at room temperature. *Nature Materials*, 19(5):540–545, 2020.

[101]Nathan Chejanovsky, Amlan Mukherjee, Youngwook Kim, Andrej Denisenko, Amit Finkler, Takashi Taniguchi, Kenji Watanabe, Durga Bhaktavatsala Rao Dasari, Jurgen H. Smet, and Jörg Wrachtrup. Single spin resonance in a van der Waals embedded paramagnetic defect. 2019.

[102]A Sajid, Kristian S Thygesen, Jeffrey R Reimers, and Michael J Ford. Identification of defects responsible for optically detected magnetic resonance in hexagonal boron nitride. pages 1–17, 2019.

[103]Mehran Kianinia, Simon White, Johannes E. Fröch, Carlo Bradac, and Igor Aharonovich. Generation of Spin Defects in Hexagonal Boron Nitride. *ACS Photonics*, pages 6–11, 2020.

[104]Annemarie L. Exarhos, David A. Hopper, Raj N. Patel, Marcus W. Doherty, and Lee C. Bassett. Magnetic-field-dependent quantum emission in hexagonal boron nitride at room temperature. *Nature Communications*, 10(1):1–8, 2019.

[105]Nicholas R Jungwirth, Brian Calderon, Yanxin Ji, Michael G Spencer, Michael E Flatté, and Gregory D Fuchs. Temperature Dependence of Wavelength Selectable Zero-Phonon

Emission from Single Defects in Hexagonal Boron Nitride. *Nano Letters*, 16:6052–6057, oct 2016.

[106]Toan Trong Tran, Mehran Kianinia, Minh Nguyen, Sejeong Kim, Zai Quan Xu, Alexander Kubanek, Milos Toth, and Igor Aharonovich. Resonant Excitation of Quantum Emitters in Hexagonal Boron Nitride. *ACS Photonics*, 5(2):295–300, 2018.

[107]Annemarie L Exarhos, David A Hopper, Richard R Grote, Audrius Alkauskas, and Lee C Bassett. Optical Signatures of Quantum Emitters in Suspended Hexagonal Boron Nitride. *ACS Nano*, 11(March):3328–3336, 2017.

[108]Matthew A. Feldman, Alex Puretzky, Lucas Lindsay, Ethan Tucker, Dayrl P. Briggs, Philip G. Evans, Richard F. Haglund, and Benjamin J. Lawrie. Phonon-induced multicolor correlations in hBN single-photon emitters. *Physical Review B*, 99(2):1–5, 2019.

[109]Sherif Abdulkader Tawfik, Sajid Ali, Marco Fronzi, Mehran Kianinia, Toan Trong Tran, Catherine Stampfl, Igor Aharonovich, Milos Toth, and Michael J. Ford. First-principles investigation of quantum emission from hBN defects. *Nanoscale*, 9(36):13575–13582, 2017.

[110]A. Sajid, Jeffrey R. Reimers, and Michael J. Ford. Defect states in hexagonal boron nitride: Assignments of observed properties and prediction of properties relevant to quantum computation. *Physical Review B*, 97(6):1–9, 2018.

[111]L. Weston, D. Wickramaratne, M. Mackoit, A. Alkauskas, and C. G. Van De Walle. Native point defects and impurities in hexagonal boron nitride. *Physical Review B*, 97(21):1–13, 2018.

[112]Feng Wu, Tyler J. Smart, Junqing Xu, and Yuan Ping. Carrier recombination mechanism at defects in wide band gap two-dimensional materials from first principles. *Physical Review B*, 100(8):1–6, 2019.

[113]Mark E. Turiansky, Audrius Alkauskas, Lee C. Bassett, and Chris G. Van De Walle. Dangling Bonds in Hexagonal Boron Nitride as Single-Photon Emitters. *Physical Review Letters*, 123(12):127401, 2019.

[114]Feng Wu, Andrew Galatas, Ravishankar Sundararaman, Dario Rocca, and Yuan Ping. First-principles engineering of charged defects for two-dimensional quantum technologies. *Physical Review Materials*, 1(7):1–6, 2017.

[115]Tyler J. Smart, Feng Wu, Marco Govoni, and Yuan Ping. Fundamental principles for calculating charged defect ionization energies in ultrathin two-dimensional materials. *Physical Review Materials*, 2(12):1–8, 2018.

[116]Dan Wang and Ravishankar Sundararaman. Substrate effects on charged defects in two-dimensional materials. *Physical Review Materials*, 3(8):1–8, 2019.

[117]Jack Strand, Luca Larcher, and Alexander L. Shluger. Properties of intrinsic point defects and dimers in hexagonal boron nitride. *Journal of Physics Condensed Matter*, 32(5), 2020.

[118]Mehdi Abdi, Jyh-pin Chou, Adam Gali, and Martin B Plenio. Color Centers in Hexagonal Boron Nitride Monolayers: A Group Theory and Ab Initio Analysis. *ACS Photonics*, 2018.

[119]Gergely Barcza, Viktor Ivády, Tibor Szilvási, Márton Vörös, Libor Veis, Ádám Gali, and Örs Legeza. DMRG on top of plane-wave Kohn-Sham orbitals: case study of defected boron nitride. pages 1–12, 2020.

[120]Viktor Ivády, Gergely Barcza, GergÅŚ Thiering, Song Li, Hanen Hamdi, Jyh Pin Chou, Örs Legeza, and Adam Gali. Ab initio theory of the negatively charged boron vacancy qubit in hexagonal boron nitride. *npj Computational Materials*, 6(1):1–6, 2020.

[121]Mads K. Boll, Ilya P. Radko, Alexander Huck, and Ulrik L. Andersen. Photophysics of quantum emitters in hexagonal boron-nitride nano-flakes. *Optics Express*, 28(5):7475, 2020.

[122]Prince Khatri, Andrew J. Ramsay, Ralph Nicholas Edward Malein, Harold M.H. Chong, and Isaac J. Luxmoore. Optical Gating of Photoluminescence from Color Centers in Hexagonal Boron Nitride. *Nano Letters*, 20(6):4256–4263, 2020.

[123]Noah Mendelson, Marcus Doherty, Milos Toth, Igor Aharonovich, and Toan Trong Tran. Strain-Induced Modification of the Optical Characteristics of Quantum Emitters in Hexagonal Boron Nitride. *Advanced Materials*, 32(21):1–9, 2020.

[124]Alexander Bommer and Christoph Becher. New insights into nonclassical light emission from defects in multi-layer hexagonal boron nitride. *Nanophotonics*, 8(11):2041–2048, 2019.

[125]Gabriele Grosso, Hyowon Moon, Christopher J. Ciccarino, Johannes Flick, Noah Mendelson, Lukas Mennel, Milos Toth, Igor Aharonovich, Prineha Narang, and Dirk R. Englund. Low-Temperature Electron-Phonon Interaction of Quantum Emitters in Hexagonal Boron Nitride. *ACS Photonics*, 7(6):1410–1417, 2020.

[126]P. Khatri, I. J. Luxmoore, and A. J. Ramsay. Phonon sidebands of color centers in hexagonal boron nitride. *Physical Review B*, 100(12):125305, 2019.

[127]Mark Fox. *Optical Properties of Solids*. 2010.

[128]Pavel Frantsuzov, Masaru Kuno, Boldizsár Jankó, and Rudolph A. Marcus. Universal emission intermittency in quantum dots, nanorods and nanowires. *Nature Physics*, 4(7):519–522, 2008.

[129]C Bradac, T Gaebel, N Naidoo, M J Sellars, J Twamley, L J Brown, A S Barnard, T Plakhotnik, A V Zvyagin, and J R Rabeau. Observation and control of blinking nitrogen- vacancy centres in discrete nanodiamonds. *Nature Publishing Group*, 5(5):345–349, apr 2010.

[130]Sorawis Sangtawesin, Bo L. Dwyer, Srikanth Srinivasan, James J. Allred, Lila V.H. Rodgers, Kristiaan De Greve, Alastair Stacey, Nikolai Dontschuk, Kane M. O'Donnell, Di Hu, D. Andrew Evans, Cherno Jaye, Daniel A. Fischer, Matthew L. Markham, Daniel J. Twitchen, Hongkun Park, Mikhail D. Lukin, and Nathalie P. De Leon. Origins of Diamond Surface Noise Probed by Correlating Single-Spin Measurements with Surface Spectroscopy. *Physical Review X*, 9(3):1–17, 2019.

[131]Zhiyang Yuan, Mattias Fitzpatrick, Lila V. H. Rodgers, Sorawis Sangtawesin, Srikanth Srinivasan, and Nathalie P. de Leon. Charge State Dynamics and Optically Detected Electron Spin Resonance Contrast of Shallow Nitrogen-Vacancy Centers in Diamond. *Physical Review Research*, 033263:1–11, 2020.

[132]L. Rondin, G. Dantelle, A. Slablab, F. Grosshans, F. Treussart, P. Bergonzo, S. Perruchas, T. Gacoin, M. Chaigneau, H. C. Chang, V. Jacques, and J. F. Roch. Surface-induced charge state conversion of nitrogen-vacancy defects in nanodiamonds. *Physical Review B - Condensed Matter and Materials Physics*, 82(11):1–5, 2010.

[133]Lucio Robledo, Hannes Bernien, Ilse Van Weperen, and Ronald Hanson. Control and coherence of the optical transition of single nitrogen vacancy centers in diamond. *Physical Review Letters*, 105(17):1–4, 2010.

[134]V. M. Acosta, C. Santori, A. Faraon, Z. Huang, K. M C Fu, A. Stacey, D. A. Simpson, K. Ganesan, S. Tomljenovic-Hanic, A. D. Greentree, S. Prawer, and R. G. Beausoleil. Dynamic stabilization of the optical resonances of single nitrogen-vacancy centers in diamond. *Physical Review Letters*, 108(20):6–11, 2012.

[135]Gergo Thiering and Adam Gali. Ab Initio Magneto-Optical Spectrum of Group-IV Vacancy Color Centers in Diamond Ab INITIO MAGNETO-OPTICAL SPECTRUM of ... GERGO THIERING and ADAM GALI. *Physical Review X*, 8(2):1–17, 2018.

[136]Rodney Louden. *The Quantum Theory of Light*. 2003.

[137]H. Paul. Photon antibunching. *Reviews of Modern Physics*, 54(4):1061–1102, 1982.

[138]Martin Berthel, Oriane Mollet, G raldine Dantelle, Thierry Gacoin, Serge Huant, and Aur lien Drezet. Photophysics of single nitrogen-vacancy centers in diamond nanocrystals. *Physical Review B*, 91(3):35308–35313, jan 2015.

[139]By R Hanbury Brown and R Q Twiss. A test of a new type of stellar interferometer on sirius. *Nature*, 17:1046–1048, 1956.

[140]Roy J. Glauber. The quantum theory of optical coherence. *Physical Review*, 130(6):2529âĂŞ2539, 1963.

[141]Zhe-Yu Jeff Ou. *Quantum Optics for Experimentalists*. 2017.

[142]Brahim Lounis and Michel Orrit. Single-photon sources. *Reports on Progress in Physics*, 68(5):1129–1179, 2005.

[143]Jingang Wang, Xuefeng Xu, Xijiao Mu, Fengcai Ma, and Mengtao Sun. Magnetics and spintronics on two-dimensional composite materials of graphene/hexagonal boron nitride. *Materials Today Physics*, 3:93 – 117, 2017.

[144]G. Cassabois, P. Valvin, and B. Gil. Hexagonal boron nitride is an indirect bandgap semiconductor. *Nature Photonics*, 10(4):262–266, 2016.

[145]T.T. Tran, K Bray, M.J. Ford, M. Toth, and I. Aharonovich. . *Nature nanotechnology*, 11(37), 2016.

[146]J. Serrano, A. Bosak, R. Arenal, M. Krisch, K. Watanabe, T. Taniguchi, H. Kanda, A. Rubio, and L. Wirtz. Vibrational properties of hexagonal boron nitride: Inelastic x-ray scattering and ab initio calculations. *Phys. Rev. Lett.*, 98:095503, Mar 2007.

[147]Matthew A Feldman, Alex Puretzky, Lucas Lindsay, Ethan Tucker, Dayrl P Briggs, Philip G Evans, Richard F Haglund, and Benjamin J Lawrie. Phonon-induced multicolor correlations in hbn single-photon emitters. *Physical Review B*, 99(2):020101, 2019.

[148]T. Q.P. Vuong, G. Cassabois, P. Valvin, A. Ouerghi, Y. Chassagneux, C. Voisin, and B. Gil. Phonon-Photon Mapping in a Color Center in Hexagonal Boron Nitride. *Physical Review Letters*, 117(9):1–5, 2016.

[149]A. Sajid, Michael J. Ford, and Jeffrey R. Reimers. Single-photon emitters in hexagonal boron nitride: a review of progress. *Reports on Progress in Physics*, 83(4), 2020.

[150]Zav Shotan, Harishankar Jayakumar, Christopher R. Considine, Mažena Mackoit, Helmut Fedder, Jörg Wrachtrup, Audrius Alkauskas, Marcus W. Doherty, Vinod M. Menon, and Carlos A. Meriles. Photoinduced Modification of Single-Photon Emitters in Hexagonal Boron Nitride. *ACS Photonics*, 3(12):2490–2496, 2016.

[151]Nicholas R Jungwirth, Brian Calderon, Yanxin Ji, Michael G Spencer, Michael E Flatté, and Gregory D Fuchs. Supplemental Info: Temperature Dependence of Wavelength Selectable Zero-Phon Emission from Single Defects in Hexagonal Boron Nitride. *ACS Nano*, 16:6052–6057, 2016.

[152]Mehran Kianinia, Blake Regan, Sherif Abdulkader Tawfik, Toan Trong Tran, Michael J. Ford, Igor Aharonovich, and Milos Toth. Robust Solid-State Quantum System Operating at 800 K. *ACS Photonics*, 4(4):768–773, 2017.

[153]Viktor IvÃądy, Gergely Barcza, GergÅŚ Thiering, Song Li, Hanen Hamdi, ÃŰrs Legeza, Jyh-Pin Chou, and Adam Gali. Ab initio theory of negatively charged boron vacancy qubit in hbn. 2019.

[154]Noah Mendelson, Dipankar Chugh, Jeffrey R Reimers, Tin S Cheng, Andreas Gottscholl, Hu Long, Christopher J Mellor, Alex Zettl, Vladimir Dyakonov, Peter H Beton, Sergei V Novikov, Chennupati Jagadish, Hark Hoe Tan, Michael J Ford, Milos Toth, Carlo Bradac, and Igor Aharonovich. Identifying carbon as the source of visible single-photon emission from hexagonal boron nitride. *Nature Materials*, 2020.

[155]T. T. Tran, C. Elbadawi, D. Totonjian, C. J. Lobo, G. Grosso, H. Moon, D. R. Englund, M. J. Ford, I. Aharonovich, and M. Toth. . *ACS nano*, 10:7331, 2016.

[156]Toan Trong Tran, Carlo Bradac, Alexander S. Solntsev, Milos Toth, and Igor Aharonovich. Suppression of spectral diffusion by anti-stokes excitation of quantum emitters in hexagonal boron nitride. *Applied Physics Letters*, 115:071102, 2019.

[157]Bernd Sontheimer, Merle Braun, Niko Nikolay, Nikola Sadzak, Igor Aharonovich, and Oliver Benson. Photodynamics of quantum emitters in hexagonal boron nitride revealed by low-temperature spectroscopy. *Physical Review B*, 96(12):1–5, 2017.

[158]L. J. Martínez, T. Pelini, V. Waselowski, J. R. Maze, B. Gil, G. Cassabois, and V. Jacques. Efficient single photon emission from a high-purity hexagonal boron nitride crystal. *Physical Review B*, 94(12):1–5, 2016.

[159]Nathan Chejanovsky, Mohammad Rezai, Federico Paolucci, Youngwook Kim, Torsten Rendler, Wafa Rouabeh, Felipe Fávaro De Oliveira, Patrick Herlinger, Andrej Denisenko, Sen Yang, Ilja Gerhardt, Amit Finkler, Jurgen H. Smet, and Jörg Wrachtrup. Structural Attributes and Photodynamics of Visible Spectrum Quantum Emitters in Hexagonal Boron Nitride. *Nano Letters*, 16(11):7037–7045, 2016.

[160]M.A. Feldman, E.F. Dumitrescu, D. Bridges, M.F. Chisholm, R.B. Davidson, P.G. Evans, J. A. Hachtel, A. Hu, R.C. Pooser, R.F. Haglund, and B. Lawrie. . *Physical Review B*, 97:081404, 2018.

[161]P.Y. Hou, Y.Y. Huang, X.X. Yuan, X.Y. Chang, C. Zu, L. He, and L.M. Duan. . *Nature Communications*, 7:11736, 2016.

[162]D. England, P. Bustard, J. Nunn, R. Lausten, and B. Sussman. . *Physical review letters*, 111:243601, 2013.

[163]D. G. England, K. A. Fisher, J.-P. W. MacLean, P. J. Bustard, R. Lausten, K. J. Resch, and B. J. Sussman. . *Physical review letters*, 114:053602, 2015.

[164]K. Lee, B. Sussman, M. Sprague, P. Michelberger, K. Reim, J. Nunn, N. Langford, P. Bustard, D. Jaksch, and I. Walmsley. . *Nature Photonics*, 6(41), 2012.

[165]M. Schuetz, E. Kessler, G. Giedke, L. Vandersypen, M. Lukin, and J. Cirac. . *PhysicalReview X*, 5:031031, 2015.

[166]I. SÃűllner, L. Midolo, and P. Lodahl. . *Physical review letters*, 116:234301, 2016.

[167]Matthew A. Feldman, Alex Puretzky, Lucas Lindsay, Ethan Tucker, Dayrl P. Briggs, Philip G. Evans, Richard F. Haglund, and Benjamin J. Lawrie. See Supplemental Material at [URL will be inserted by publisher] for additional details on emission cross-section calculation and the experimental apparatus. *See Supplemental Material at [URL will be inserted by publisher] for additional details on emission cross-section calculation and the experimental apparatus*, 2019.

[168]L. Weston, D. Wickramaratne, M. Mackoit, A. Alkauskas, and C. Van de Walle. . *PhysicalReview B*, 97:214104, 2018.

[169]J. Serrano, A. Bosak, R. Arenal, M. Krisch, K. Watanabe, T. Taniguchi, H. Kanda, A. Rubio, and L. Wirtz. . *Physical Review Letters*, 98(12), 2007.

[170]G. Kern, G. Kresse, and J. Hafner. . *Phys. Rev. B*, 59:8551, 1999.

[171]R. Geick, C. Perry, and G. Rupprecht. . *Physical Review*, 146:543, 1966.

[172]R. J. Nemanich, S. A. Solin, and R. M. Martin. . *Physical Review B*, 23:6348, 1981.

[173]P. Jiang, X. Qian, R. Yang, and L. Lindsay. . *arXiv:1805.00564*, 2018.

[174]G. Davies. . *Journal of Physics C: Solid State Physics*, 7(3797), 1974.

[175]A.A. Maradudin. . *Solid State Physics - Advances in Research and Applications*, 19(1), 1967.

[176]A. M. Stoneham. *Theory of defects in solids: electronic structure of defects in insulators and semiconductors*. Oxford University Press, 2001.

[177]A. M. Marino, V. Boyer, and P. D. Lett. . *Physical review letters*, 100:233601, 2008.

[178]J. F. Clauser. . *Physical Review D*, 9(853), 1974.

[179]S.-K. Liao, W.-Q. Cai, W.-Y. Liu, L. Zhang, Y. Li, J.-G. Ren, J. Yin, Q. Shen, Y. Cao, Z.-P. Li, F.-Z Li, and X.-W Chen. . *Nature*, 549(43), 2017.

[180]J. Yin, Y. Cao, Y.-H. Li, J.-G. Ren, S.-K. Liao, L. Zhang, W.-Q. Cai, W.-Y. Liu, B. Li, H. Da, M. Li, Y.-M. Huang, and L. Deng. . *Physical review letters*, 119:200501, 2017.

[181]P. Li, M. Lewin, A. V. Kretinin, J. D. Caldwell, K. S. Novoselov, T. Taniguchi, K. Watanabe, F. Gaussmann, and T. Taubner. . *Nature Communications*, 6(7507), 2015.

[182]R. Ruskov ÃŰ. Soykal and C. Tahan. . *Physical review letters*, 107:235502, 2011.

[183]Matthew Feldman, Claire Marvinney, Alexander Puretzky, and Ben Lawrie. Evidence of photochromism in a hexagonal boron nitride single-photon emitter. *Optica*, 8(1), 2020.

[184]Igor Aharonovich, Dirk Englund, and Milos Toth. Solid-state single-photon emitters. *Nature Photonics*, 10(10):631, 2016.

[185]David D Awschalom, Lee C Bassett, Andrew S Dzurak, Evelyn L Hu, and Jason R Petta. Quantum spintronics: engineering and manipulating atom-like spins in semiconductors. *Science*, 339(6124):1174–1179, 2013.

[186]David D Awschalom, Ronald Hanson, Jörg Wrachtrup, and Brian B Zhou. Quantum technologies with optically interfaced solid-state spins. *Nature Photonics*, 12(9):516–527, 2018.

[187]Toan Trong Tran, Kerem Bray, Michael J Ford, Milos Toth, and Igor Aharonovich. Quantum emission from hexagonal boron nitride monolayers. *Nature Nanotechnology*, 11(1):37, 2016.

[188]Andreas Gottscholl, Mehran Kianinia, Victor Soltamov, Sergei Orlinskii, Georgy Mamin, Carlo Bradac, Christian Kasper, Klaus Krambrock, Andreas Sperlich, Milos Toth, et al. Initialization and read-out of intrinsic spin defects in a van der waals crystal at room temperature. *Nature Materials*, 19(5):540–545, 2020.

[189]Mete Atatüre, Dirk Englund, Nick Vamivakas, Sang-Yun Lee, and Joerg Wrachtrup. Material platforms for spin-based photonic quantum technologies. *Nature Reviews Materials*, 3(5):38–51, 2018.

[190]Prince Khatri, Andrew J Ramsay, Ralph Nicholas Edward Malein, Harold MH Chong, and Isaac J Luxmoore. Optical gating of photoluminescence from color centers in hexagonal boron nitride. *Nano Letters*, 20(6):4256, 2020.

[191]Kumarasiri Konthasinghe, Chitraleema Chakraborty, Nikhil Mathur, Liangyu Qiu, Arunabh Mukherjee, Gregory D Fuchs, and A Nick Vamivakas. Rabi oscillations and resonance fluorescence from a single hexagonal boron nitride quantum emitter. *Optica*, 6(5):542–548, 2019.

[192]Nicholas V Proscia, Zav Shotan, Harishankar Jayakumar, Prithvi Reddy, Charles Cohen, Michael Dollar, Audrius Alkauskas, Marcus Doherty, Carlos A Meriles, and Vinod M Menon. Near-deterministic activation of room-temperature quantum emitters in hexagonal boron nitride. *Optica*, 5(9):1128–1134, 2018.

[193]Gabriele Grosso, Hyowon Moon, Benjamin Lienhard, Sajid Ali, Dmitri K Efetov, Marco M Furchi, Pablo Jarillo-Herrero, Michael J Ford, Igor Aharonovich, and Dirk Englund. Tunable and high-purity room temperature single-photon emission from atomic defects in hexagonal boron nitride. *Nature Communications*, 8(1):1–8, 2017.

[194]Sherif Abdulkader Tawfik, Sajid Ali, Marco Fronzi, Mehran Kianinia, Toan Trong Tran, Catherine Stampfl, Igor Aharonovich, Milos Toth, and Michael J Ford. First-principles investigation of quantum emission from hbn defects. *Nanoscale*, 9(36):13575–13582, 2017.

[195]A. Sajid, Jeffrey R. Reimers, and Michael J. Ford. Defect states in hexagonal boron nitride: Assignments of observed properties and prediction of properties relevant to quantum computation. *Phys. Rev. B*, 97:064101, Feb 2018.

[196]Fariah Hayee, Leo Yu, Jingyuan Linda Zhang, Christopher J Ciccarino, Minh Nguyen, Ann F Marshall, Igor Aharonovich, Jelena Vučković, Prineha Narang, Tony F Heinz, et al. Revealing multiple classes of stable quantum emitters in hexagonal boron nitride with correlated optical and electron microscopy. *Nature Materials*, 19(5):534–539, 2020.

[197]Toan Trong Tran, Christopher Elbadawi, Daniel Totonjian, Charlene J Lobo, Gabriele Grosso, Hyowon Moon, Dirk R Englund, Michael J Ford, Igor Aharonovich, and Milos Toth. Robust multicolor single photon emission from point defects in hexagonal boron nitride. *ACS Nano*, 10(8):7331–7338, 2016.

[198]Zav Shotan, Harishankar Jayakumar, Christopher R Considine, Mazena Mackoit, Helmut Fedder, JoÌĹrg Wrachtrup, Audrius Alkauskas, Marcus W Doherty, Vinod M Menon, and Carlos A Meriles. Photoinduced modification of single-photon emitters in hexagonal boron nitride. *ACS Photonics*, 3(12):2490–2496, 2016.

[199]Hanh Ngoc My Duong, Minh Anh Phan Nguyen, Mehran Kianinia, Takeshi Ohshima, Hiroshi Abe, Kenji Watanabe, Takashi Taniguchi, James H Edgar, Igor Aharonovich, and Milos Toth. Effects of high-energy electron irradiation on quantum emitters in hexagonal boron nitride. *ACS Applied Materials & Interfaces*, 10(29):24886–24891, 2018.

[200]Nicholas R. Jungwirth, Brian Calderon, Yanxin Ji, Michael G. Spencer, Michael E. Flatte, and Gregory D. Fuchs. Temperature dependence of wavelength selectable zero-phonon emission from single defects in hexagonal boron nitride. *Nano Letters*, 16(10):6052–6057, 2016.

[201]Nicholas R. Jungwirth and Gregory D. Fuchs. Optical absorption and emission mechanisms of single defects in hexagonal boron nitride. *Phys. Rev. Lett.*, 119:057401, Jul 2017.

[202]Noah Mendelson, Marcus Doherty, Milos Toth, Igor Aharonovich, and Toan Trong Tran. Strain-induced modification of the optical characteristics of quantum emitters in hexagonal boron nitride. *Advanced Materials*, 32(21):1908316, 2020.

[203]Andrei V. Kanaev, Jean Pierre Petitet, Luc Museur, Vladimir Marine, Vladimir L. Solozhenko, and Vassilis Zafiropulos. Femtosecond and ultraviolet laser irradiation of graphitelike hexagonal boron nitride. *Journal of Applied Physics*, 96(8):4483–4489, 2004.

[204]TQP Vuong, Guillaume Cassabois, Pierre Valvin, Abdelkarim Ouerghi, Yannick Chassagneux, Christophe Voisin, and Bernard Gil. Phonon-photon mapping in a color center in hexagonal boron nitride. *Physical Review Letters*, 117(9):097402, 2016.

[205]P Khatri, IJ Luxmoore, and AJ Ramsay. Phonon sidebands of color centers in hexagonal boron nitride. *Physical Review B*, 100(12):125305, 2019.

[206]Alexander Bommer and Christoph Becher. New insights into nonclassical light emission from defects in multi-layer hexagonal boron nitride. *Nanophotonics*, 8(11):2041–2048, 2019.

[207]Martin Berthel, Oriane Mollet, Géraldine Dantelle, Thierry Gacoin, Serge Huant, and Aurélien Drezet. Photophysics of single nitrogen-vacancy centers in diamond nanocrystals. *Physical Review B*, 91(3):035308, 2015.

[208]Feng Wu, Tyler J. Smart, Junqing Xu, and Yuan Ping. Carrier recombination mechanism at defects in wide band gap two-dimensional materials from first principles. *Phys. Rev. B*, 100:081407, Aug 2019.

[209]Srujan Meesala, Young-Ik Sohn, Benjamin Pingault, Linbo Shao, Haig A. Atikian, Jeffrey Holzgrafe, Mustafa Gündoğan, Camille Stavrakas, Alp Sipahigil, Cleaven Chia, Ruffin Evans, Michael J. Burek, Mian Zhang, Lue Wu, Jose L. Pacheco, John Abraham, Edward Bielejec, Mikhail D. Lukin, Mete Atatüre, and Marko Lončar. Strain engineering of the silicon-vacancy center in diamond. *Phys. Rev. B*, 97:205444, May 2018.

[210]Luc Museura, Demetrios Anglos, Jean-Pierre Petitet, Jean-Pierre Michel, and Andrei V. Kanaevc. Photoluminescence of hexagonal boron nitride: Effect of surface oxidation under uv-laser irradiation. *Journal of Luminesence*, 127:595–600, 2007.

[211]B. Berzina, V. Korsaks, L. Trinkler, A. Sarakovskis, J. Grube, and S. Bellucci. Defect-induced blue luminescence of hexagonal boron nitride. *Diamond and Related Materials*, 68:131–137, 2016.

[212]Brian D. Gerardot, Stefan Strauf, Michiel J. A. de Dood, Andrey M. Bychkov, Antonio Badolato, Kevin Hennessy, Evelyn L. Hu, Dirk Bouwmeester, and Pierre M. Petroff. Photon statistics from coupled quantum dots. *Phys. Rev. Lett.*, 95:137403, Sep 2005.

[213]Ruffin E Evans, Mihir K Bhaskar, Denis D Sukachev, Christian T Nguyen, Alp Sipahigil, Michael J Burek, Bartholomeus Machielse, Grace H Zhang, Alexander S Zibrov, Edward Bielejec, et al. Photon-mediated interactions between quantum emitters in a diamond nanocavity. *Science*, 362(6415):662–665, 2018.

[214]G. J. Beirne, C. Hermannstädter, L. Wang, A. Rastelli, O. G. Schmidt, and P. Michler. Quantum light emission of two lateral tunnel-coupled (In,Ga)As/GaAs quantum dots controlled by a tunable static electric field. *Phys. Rev. Lett.*, 96:137401, Apr 2006.

[215]Z. Ficek, R. Tanaś, and S. Kielich. Photon antibunching and squeezing in resonance fluorescence of two interacting atoms. *Phys. Rev. A*, 29:2004–2011, Apr 1984.